Light Modulation with Vanadium Dioxide-Based Optical Devices

Thesis by

Yonghwi Kim

In Partial Fulfillment of the Requirements for

the Degree of

Doctor of Philosophy

CALIFORNIA INSTITUTE OF TECHNOLOGY

Pasadena, California

2022

(Defended June 18, 2021)

Yonghwi Kim
ORCID: 0000-0002-6652-7994

ACKNOWLEDGMENTS

First of all, I would like to express my sincere gratitude to my advisor, Professor Harry A. Atwater, for his endless support and guidance throughout this academic journey. I was inspired by his enthusiasm for novel science and engineering, which guided me to finish my PhD study. It has been a great honor to be in his group as I was able to expose myself to a great research environment including various research projects, facilities, and collaborators.

I would like to thank my thesis committee members, Professor Andrei Faraon, Professor Axel Scherer, and Professor Alireza Marandi, for their helpful academic advice and guidance throughout my PhD study. I also want to thank Professor George Rossman for his help and assistance with optical characterization.

Next, I would like to thank all of the collaborators: Professor Pin Chieh Wu, Dr. Ruzan Sokhoyan, Dr. Kelly Mauser, Rebecca Glaudell, and Dr. Ghazaleh Kafaie Shirmanesh for the phase modulation project; Professor Ognjen Ilic and Komron Shayegan for the thermal emission control project; Dr. Pankaj K. Jha, Hamidreza Akbari and Souvik Biswas for the quantum emission project; Ramon Gao and Dr. Michael D. Kelzenberg for the lightsail project. I appreciate Dr. Seyoon Kim, Dr. Meir Grajower, Joeson Wong, Dr. Wei-Hsiang Lin, Dr. Kiyoul Yang, Dr. Taeyoon Lee, Dr. Myung-Gyun Suh, Dr. Laura Kim, and Areum Kim for their help in fulfilling my projects.

I have been lucky enough to get technical and emotional support from Kam Flower and the current and previous KNI staffs, especially Sangkook Lee, Dr. Guy A. DeRose, and Dr. Matthew S. Hunt. I also want to acknowledge the support from the Kwanjeong Educational Foundation scholarship. It has been my pleasure to meet many colleagues from Caltech Korean Graduate Student Association.

I would also like to thank my parents and brother for their endless support and encouragement. I also truly appreciate my wife, Sung-Hee Paik, for her consistent love and dedication, as well as my little one-year-old son, Jaejoong Kim, for staying healthy and happy throughout this hard time. Lastly, I would like to thank my daughter, Jiwon Kim, who was born last week and become my new family member.

ABSTRACT

This thesis focuses on active material-based tunable optical devices. In particular, I have been working on tunable optical devices based on vanadium dioxide (VO_2), which can produce tunable optical responses, such as amplitude, phase, thermal emission, and quantum emission. The modulations of light are achieved by coupling the phase-transition material with the precisely designed resonant structures or by placing it close to quantum emitters. This thesis presents three research streams, which aim at experimentally demonstrating the dynamically tunable optical responses using VO_2. First, we propose and experimentally demonstrate an electrically tunable VO_2-based reflectarray metasurface that exhibits largely tunable optical responses in the near-infrared region. We incorporate VO_2 directly into the plasmonic resonator, which undergoes a phase transition triggered by Joule heating. The induced plasmonic resonance modulation is accompanied by a large and continuous modulation in optical responses, such as amplitude, resonance wavelength, and phase. Second, we propose and demonstrate an active tuning of thermal emission from VO_2-based metasurfaces. We introduce a thin VO_2 film as an absorbing layer on top of a metal reflector. This layer is coupled with a dielectric resonator, with a dielectric spacer placed between them. Upon undergoing a phase transition triggered by heating, the induced absorption tuning of the VO_2 layer is accompanied by modulation in the absorption spectra of the coupled structure. We experimentally show narrowband absorption spectra, which can be tuned by controlling the VO_2 temperature. Finally, we experimentally demonstrate the axial position of quantum emitters in a multilayered hexagonal boron nitride (*h*BN) flake with nanoscale accuracy, which is enabled through the modification of a photonic density of states by introducing VO_2. Furthermore, we observe a sharp distance-dependent

photoluminescence response by modulating the optical environment of an emitter placed close to the *h*BN/VO_2 interface.

PUBLISHED CONTENT AND CONTRIBUTIONS

Kim, Y.; Wu, P. C.; Sokhoyan, R.; Mauser, K.; Glaudell, R.; Shirmanesh, G. K.; Atwater, H. A. Phase Modulation with Electrically Tunable Vanadium Dioxide Phase-Change Metasurfaces. *Nano Lett.* 2019, 19 (6), 3961-3968.
https://pubs.acs.org/doi/10.1021/acs.nanolett.9b01246
Contribution: conception of the idea, full-wave simulation, sample fabrication and characterization

Kim, Y.; Wu, P. C.; Sokhoyan, R.; Mauser, K.; Glaudell, R.; Shirmanesh, G. K.; Atwater, H. A. Electrically Tunable Metasurfaces Incorporating A Phase Change Material. *US Patent*, 2016, Pub. No.: US2020/0227632 A1.
https://patents.google.com/patent/US20200227632A1/en
Contribution: conception of the idea, full-wave simulation, sample fabrication and characterization

Tumkur, T. U.; Sokhoyan, R.; Su, M. P.; Ceballos-Sanchez, A.; Shirmanesh, G. K.; **Kim, Y.**; Atwater, H. A.; Feigenbaum, E.*; Elhadj, S.* Toward High Laser Power Beam Manipulation with Nanophotonic Materials: Evaluating Thin Film Damage Performance. *Opt. Express*, 2012, 29 (5), 7261-7275.
https://www.osapublishing.org/oe/fulltext.cfm?uri=oe-29-5-7261&id=447943
Contribution: full-wave simulation, sample preparation and characterization

Jha, P.†; Akbari, H.†; **Kim, Y.**†; Biswas, S.; Atwater, H. A. Nanoscale Axial Position and Orientation Measurement of Hexagonal Boron Nitride Quantum Emitters using a Tunable Nanophotonic Environment (*submitted*).
†These authors contributed equally to this work.
https://arxiv.org/abs/2007.07811
Contribution: conception of the idea, full-wave simulation, sample preparation and characterization

Kim, Y.; Ilic, O.; Shayegan, K.; Atwater, H. A. Tunable Narrowband Thermal Emission Based on Phase Change Metasurfaces Coupled with Dielectric Resonators (*in preparation*).
Contribution: conception of the idea, full-wave simulation, sample fabrication and characterization

Shayegan, K.; Zhao, B.; **Kim, Y.**; Fan, S.; Atwater, H. A. Towards Experimentally Violating Kirchhoff's Law of Thermal Radiation Using a Guided-Mode Resonator Coupled to Magneto-Optic InAs (*in preparation*).
Contribution: sample fabrication

Gao, R.; Kelzenberg, M. D.; **Kim, Y.**; Merkt, A.; Ilic, O.; Atwater, H. A. Measuring restoring Optical Forces and Torques from Metagratings (*in preparation*).
Contribution: sample fabrication

TABLE OF CONTENTS

LIST OF ILLUSTRATIONS

Number *Page*

Chapter 1

INTRODUCTION

1.1 Optical Metasurfaces

Optical metasurfaces comprise arrays of subwavelength optical elements that resonantly interact with the incident light and alter its properties, such as amplitude, phase, wavelength, and polarization, in a well-defined manner [1, 2]. Optical metasurfaces have drawn tremendous attention due to their potential to replace conventional optical components by introducing flat and compact subwavelength resonant elements with reduced footprints. In analogy to conventional optics, optical metasurfaces are capable of modifying the wavefront of light in any desired manner. While bulky optical components rely on propagation effects defined by refractive indices of the media, metasurfaces manipulate resonant elements that capture and scatter light with abrupt changes in optical properties. Many applications using metasurfaces, enabled by standard semiconductor manufacturing processes, have been demonstrated, including beam-steering [3, 4], focusing lenses/mirrors [5, 6], polarization conversion [7-9], and holograms [10-12].

1.2 Active Metasurfaces

Although passive metasurfaces have varied applications, the device functions remain invariable, and thus, they cannot be tuned at will. Recently, active metasurfaces, which provide advanced control of wave propagation with multiple functionalities in a

reconfigurable manner, have been extensively researched. Various applications can be realized using dynamically tunable metasurfaces, such as chip-scale beam-steering devices for light detection and ranging (LiDAR) systems, reconfigurable metalenses, and 3D holographic displays. Active metasurface designs with tunable optical responses comprise thermo-optic effects in semiconductors [13-15]; field effect in indium tin oxide [16-20], gallium arsenide [21], silicon [22], and graphene [23-27]; and phase transition in germanium antimony telluride (GST) [28-33] and vanadium dioxide (VO_2) [34-43]; as well as liquid crystals [44-47], ionic transport [48], and mechanical deformations [49-51]. In addition to amplitude modulation, by controlling the phase of light [18, 20, 27], phased-array active metasurfaces can be realized for complex wavefront engineering by, for example, controlling the phase profile of the light with a spatially varying phase of metasurface elements [19].

1.3 Vanadium Dioxide as an Active Material

To achieve stronger modulation in optical responses, it is preferable to introduce an active medium possessing a large contrast in optical properties. In this regard, metasurfaces incorporating phase-change materials (PCMs)—such as GST and VO_2, which exhibit substantially varying refractive indices over a broad spectral range—are strong candidates among the various active device designs. Vanadium dioxide, a well-known temperature-driven phase transition material, is an attractive material that exhibits a large index contrast upon phase transition as well as a near-room-temperature transition threshold ($T_c \approx 340$ K) [52], which is beneficial for realizing energy-efficient devices. The fundamental physics involved in the transition process has been extensively studied [53-55]. Liu et al. studied the ultrafast dynamic behavior of photo-induced phase transition in VO_2 thin films [56] and identified the contribution of size and oxygen stoichiometry to the phase transition of VO_2

[57, 58]. The phase transition of VO_2 can be triggered by external stimuli, such as heat, light, electric field, and even direct electrons [59]. This makes VO_2 a promising PCM for use in tunable metamaterials. However, despite extensive efforts, it is still debated whether VO_2 phase transition is a Peierls insulator-to-metal transition (IMT) or a Mott IMT [52]. Regardless of the intricate physical mechanisms governing the phase change in VO_2, the material can be used for numerous applications through diverse external excitations. This material and its IMT can then be used as electrical switches, thermal modulators, thermochromic windows, and optical modulators.

1.4 Thesis Scope

In this thesis, we investigate the physical properties and applications of VO_2 metasurfaces, which can actively modulate the fundamental properties of light. In Chapter 2, we discuss the VO_2 thin-film growth and characterizations that are essential in this thesis. In addition, we present the structural, electrical, and optical properties of VO_2 films. In Chapter 3, we propose and demonstrate an electrically tunable VO_2-based reflectarray metasurface that exhibits wide phase shifts in the near-infrared region. We incorporate VO_2 directly into the structure as an active medium to enhance the light–mater interaction in the resonance cavity. Upon undergoing a phase transition triggered by Joule heating, the induced plasmonic resonance tuning is accompanied by a large modulation in optical responses, such as amplitude, resonance wavelength, and phase. In Chapter 4, we present active thermal emission control based on a VO_2 metasurface, which comprises a thin-film absorber coupled with a resonant waveguide structure, with a dielectric spacer placed between them. The coupled structure exhibits tunable and narrowband thermal emission, which is achieved by coupling a VO_2-based absorber and a narrowband dielectric resonant structure. In Chapter 5,

we experimentally demonstrate the axial position measurement of quantum emitters in a multilayered hexagonal boron nitride (*h*BN) flake with nanoscale accuracy. This is accomplished by tuning the local density of states by using an optical PCM (i.e., VO_2). We modulate the optical environment of an emitter near the VO_2/sapphire substrate, which generates a sharp distance-dependent PL response. In Chapter 6, we discuss the potential application of VO_2 metasurfaces as beam-steering devices, which require dynamical manipulation of light. In addition, we present thermal management of VO_2 metasurfaces for an individual unit cell control and envision the beam-steering capability through numerical analysis.

1.5 References

[1] Yu, N.; Genevet, P.; Kats, M. A.; Aieta, F.; Tetienne, J.-P.; Capasso, F.; Gaburro, Z. Light Propagation with Phase Discontinuities: Generalized Laws of Reflection and Refraction. *Science* 2011, 334 (6054), 333–337.

[2] Kildishev, A. V.; Boltasseva, A.; Shalaev, V. M. Planar Photonics with Metasurfaces. *Science* 2013, 339 (6125), 1232009.

[3] Sun, S.; Yang, K.-Y.; Wang, C.-M.; Juan, T.-K.; Chen, W. T.; Liao, C. Y.; He, Q.; Xiao, S.; Kung, W.-T.; Guo, G.-Y. Zhou L.; Tsai, D. P. High-Efficiency Broadband Anomalous Reflection by Gradient Meta-Surfaces. *Nano Lett.* 2012, 12 (12), 6223–6229.

[4] Pors, A.; Albrektsen, O.; Radko, I. P.; Bozhevolnyi, S. I. Gap Plasmon-Based Metasurfaces for Total Control of Reflected Light. *Sci. Rep.* 2013, 3, 2155.

[5] Lin, D.; Fan, P.; Hasman, E.; Brongersma, M. L. Dielectric Gradient Metasurface Optical Elements. *Science* 2014, 345 (6194), 298–302.

[6] Khorasaninejad, M.; Chen, W. T.; Devlin, R. C.; Oh, J.; Zhu, A. Y.; Capasso, F. Metalenses at Visible Wavelengths: Diffraction-Limited Focusing and Subwavelength Resolution Imaging. *Science* 2016, 352 (6290), 1190–1194.

[7] Arbabi, A.; Horie, Y.; Bagheri, M.; Faraon, A. Dielectric Metasurfaces for Complete Control of Phase and Polarization with Subwavelength Spatial Resolution and High Transmission. *Nat. Nanotechnol.* 2015, 10 (11), 937–943.

[8] Wu, P. C.; Tsai, W.-Y.; Chen, W. T.; Huang, Y.-W.; Chen, T.-Y.; Chen, J.-W.; Liao, C. Y.; Chu, C. H.; Sun, G.; Tsai, D. P. Versatile Polarization Generation with an Aluminum Plasmonic Metasurface. *Nano Lett.* 2017, 17 (1), 445–452.

[9] Black, L.-J.; Wang, Y.; de Groot, C. H.; Arbouet, A.; Muskens, O. L. Optimal Polarization Conversion in Coupled Dimer Plasmonic Nanoantennas for Metasurfaces. *ACS Nano* 2014, 8 (6), 6390–6399.

[10] Chen, W. T.; Yang, K.-Y.; Wang, C.-M.; Huang, Y.-W.; Sun, G.; Chiang, I.-D.; Liao, C. Y.; Hsu, W.-L.; Lin, H. T.; Sun, S. et al. High-Efficiency Broadband Meta-Hologram with Polarization-Controlled Dual Images. *Nano Lett.* 2014, 14 (1), 225–230.

[11] Zheng, G.; Mühlenbernd, H.; Kenney, M.; Li, G.; Zentgraf, T.; Zhang, S. Metasurface Holograms Reaching 80% Efficiency. *Nat. Nanotechnol.* 2015, 10 (4), 308–312.

[12] Huang, Y.-W.; Chen, W. T.; Tsai, W.-Y.; Wu, P. C.; Wang, C.-M.; Sun, G.; Tsai, D. P. Aluminum Plasmonic Multicolor Meta-Hologram. *Nano Lett.* 2015, 15 (5), 3122–3127.

[13] Lewi, T.; Evans, H. A.; Butakov, N. A.; Schuller, J. A. Ultrawide Thermo-Optic Tuning of PbTe Meta-Atoms. *Nano Lett.* 2017, 17 (6), 3940–3945.

[14] Rahmani, M.; Xu, L.; Miroshnichenko, A. E.; Komar, A.; Camacho-Morales, R.; Chen, H.; Zárate, Y.; Kruk, S.; Zhang, G.; Neshev, D. N. et al. Reversible Thermal Tuning of All-Dielectric Metasurfaces. *Adv. Funct. Mater.* 2017, 27 (31), 1700580.

[15] Horie, Y.; Arbabi, A.; Arbabi, E.; Kamali, S. M.; Faraon, A. High-Speed, Phase-Dominant Spatial Light Modulation with Silicon-Based Active Resonant Antennas. *ACS Photonics* 2018, 5 (5), 1711–1717.

[16] Yi, F.; Shim, E.; Zhu, A. Y.; Zhu, H.; Reed, J. C.; Cubukcu, E. Voltage Tuning of Plasmonic Absorbers by Indium Tin Oxide. *Appl. Phys. Lett.* 2013, 102 (22), 221102.

[17] Park, J.; Kang, J.-H.; Liu, X.; Brongersma, M. L. Electrically Tunable Epsilon-Near-Zero (ENZ) Metafilm Absorbers. *Sci. Rep.* 2015, 5, 15754.

[18] Park, J.; Kang, J.-H.; Kim, S. J.; Liu, X.; Brongersma, M. L. Dynamic Reflection Phase and Polarization Control in Metasurfaces. *Nano Lett.* 2017, 17 (1), 407–413.

[19] Huang, Y.-W.; Lee, H. W. H.; Sokhoyan, R.; Pala, R. A.; Thyagarajan, K.; Han, S.; Tsai, D. P.; Atwater, H. A. Gate-Tunable Conducting Oxide Metasurfaces. *Nano Lett.* 2016, 16 (9), 5319–5325.

[20] Kafaie, S. G.; Sokhoyan, R.; Pala, R. A.; Atwater, H. A. Dual-Gated Active Metasurface at 1550 Nm with Wide (>300°) Phase Tunability. *Nano Lett.* 2018, 18 (5), 2957–2963.

[21] Jun, Y. C.; Reno, J.; Ribaudo, T.; Shaner, E.; Greffet, J.-J.; Vassant, S.; Marquier, F.; Sinclair, M.; Brener, I. Epsilon-Near-Zero Strong Coupling in Metamaterial-Semiconductor Hybrid Structures. *Nano Lett.* 2013, 13 (11), 5391–5396.

[22] Olivieri, A.; Chen, C.; Hassan, S.; Lisicka-Skrzek, E.; Tait, R. N.; Berini, P. Plasmonic Nanostructured Metal–Oxide–Semiconductor Reflection Modulators. *Nano Lett.* 2015, 15 (4), 2304–2311.

[23] Yao, Y.; Kats, M. A.; Genevet, P.; Yu, N.; Song, Y.; Kong, J.; Capasso, F. Broad Electrical Tuning of Graphene-Loaded Plasmonic Antennas. *Nano Lett.* 2013, 13 (3), 1257–1264.

[24] Jang, M. S.; Brar, V. W.; Sherrott, M. C.; Lopez, J. J.; Kim, L.; Kim, S.; Choi, M.; Atwater, H. A. Tunable Large Resonant Absorption in a Midinfrared Graphene Salisbury Screen. *Phys. Rev. B* 2014, 90 (16), 165409.

[25] Dabidian, N.; Kholmanov, I.; Khanikaev, A. B.; Tatar, K.; Trendafilov, S.; Mousavi, S. H.; Magnuson, C.; Ruoff, R. S.; Shvets, G. Electrical Switching of Infrared Light Using Graphene Integration with Plasmonic Fano Resonant Metasurfaces. *ACS Photonics* 2015, 2 (2), 216–227.

[26] Wu, P. C.; Papasimakis, N.; Tsai, D. P. Self-Affine Graphene Metasurfaces for Tunable Broadband Absorption. *Phys. Rev. Appl.* 2016, 6 (4), 044019.

[27] Sherrott, M. C.; Hon, P. W. C.; Fountaine, K. T.; Garcia, J. C.; Ponti, S. M.; Brar, V. W.; Sweatlock, L. A.; Atwater, H. A. Experimental Demonstration of >230° Phase Modulation in Gate-Tunable Graphene–Gold Reconfigurable Mid-Infrared Metasurfaces. *Nano Lett.* 2017, 17 (5), 3027–3034.

[28] Chen, Y.; Li, X.; Sonnefraud, Y.; Fernández-Domínguez, A. I.; Luo, X.; Hong, M.; Maier, S. A. Engineering the Phase Front of Light with Phase-Change Material Based Planar Lenses. *Sci. Rep.* 2015, 5, 8660.

[29] Tittl, A.; Michel, A.-K. U.; Schäferling, M.; Yin, X.; Gholipour, B.; Cui, L.; Wuttig, M.; Taubner, T.; Neubrech, F.; Giessen, H. A Switchable Mid-Infrared Plasmonic Perfect Absorber with Multispectral Thermal Imaging Capability. *Adv. Mater.* 2015, 27 (31), 4597–4603.

[30] Yin, X.; Steinle, T.; Huang, L.; Taubner, T.; Wuttig, M.; Zentgraf, T.; Giessen, H. Beam Switching and Bifocal Zoom Lensing Using Active Plasmonic Metasurfaces. *Light Sci. Appl.* 2017, 6 (7), e17016.

[31] Wang, Q.; Rogers, E. T. F.; Gholipour, B.; Wang, C.-M.; Yuan, G.; Teng, J.; Zheludev, N. I. Optically Reconfigurable Metasurfaces and Photonic Devices Based on Phase Change Materials. *Nat. Photonics* 2016, 10 (1), 60–65.

[32] Galarreta, C. R. de; Alexeev, A. M.; Au, Y.-Y.; Lopez-Garcia, M.; Klemm, M.; Cryan, M.; Bertolotti, J.; Wright, C. D. Nonvolatile Reconfigurable Phase-Change Metadevices for Beam Steering in the Near Infrared. *Adv. Funct. Mater.* 2018, 28 (10), 1704993.

[33] Hosseini, P.; Wright, C. D.; Bhaskaran, H. An Optoelectronic Framework Enabled by Low-Dimensional Phase-Change Films. *Nature* 2014, 511 (7508), 206–211.

[34] Driscoll, T.; Palit, S.; Qazilbash, M. M.; Brehm, M.; Keilmann, F.; Chae, B.-G.; Yun, S.-J.; Kim, H.-T.; Cho, S. Y.; Jokerst, N. M. et al. Dynamic Tuning of an

Infrared Hybrid-Metamaterial Resonance Using Vanadium Dioxide. *Appl. Phys. Lett.* 2008, 93 (2), 024101.

[35] Dicken, M. J.; Aydin, K.; Pryce, I. M.; Sweatlock, L. A.; Boyd, E. M.; Walavalkar, S.; Ma, J.; Atwater, H. A. Frequency Tunable Near-Infrared Metamaterials Based on VO_2 Phase Transition. *Opt. Express* 2009, 17 (20), 18330–18339.

[36] Kats, M. A.; Sharma, D.; Lin, J.; Genevet, P.; Blanchard, R.; Yang, Z.; Qazilbash, M. M.; Basov, D. N.; Ramanathan, S.; Capasso, F. Ultra-Thin Perfect Absorber Employing a Tunable Phase Change Material. *Appl. Phys. Lett.* 2012, 101 (22), 221101.

[37] Kocer, H.; Butun, S.; Banar, B.; Wang, K.; Tongay, S.; Wu, J.; Aydin, K. Thermal Tuning of Infrared Resonant Absorbers Based on Hybrid Gold-VO_2 Nanostructures. *Appl. Phys. Lett.* 2015, 106 (16), 161104.

[38] Dong, K.; Hong, S.; Deng, Y.; Ma, H.; Li, J.; Wang, X.; Yeo, J.; Wang, L.; Lou, S.; Tom, K. B. et al. A Lithography-Free and Field-Programmable Photonic Metacanvas. *Adv. Mater.* 2018, 30 (5), 1703878.

[39] Liu, M.; Hwang, H. Y.; Tao, H.; Strikwerda, A. C.; Fan, K.; Keiser, G. R.; Sternbach, A. J.; West, K. G.; Kittiwatanakul, S.; Lu, J. et al. Terahertz-Field-Induced Insulator-to-Metal Transition in Vanadium Dioxide Metamaterial. *Nature* 2012, 487 (7407), 345–348.

[40] Driscoll, T.; Kim, H.-T.; Chae, B.-G.; Kim, B.-J.; Lee, Y.-W.; Jokerst, N. M.; Palit, S.; Smith, D. R.; Ventra, M. D.; Basov, D. N. Memory Metamaterials. *Science* 2009, 325 (5947), 1518–1521.

[41] Liu, L.; Kang, L.; Mayer, T. S.; Werner, D. H. Hybrid Metamaterials for Electrically Triggered Multifunctional Control. *Nat. Commun.* 2016, 7, 13236.

[42] Zhu, Z.; Evans, P. G.; Haglund, R. F.; Valentine, J. G. Dynamically Reconfigurable Metadevice Employing Nanostructured Phase-Change Materials. *Nano Lett.* 2017, 17 (8), 4881–4885.

[43] Hashemi, M. R. M.; Yang, S.-H.; Wang, T.; Sepúlveda, N.; Jarrahi, M. Electronically-Controlled Beam-Steering through Vanadium Dioxide Metasurfaces. *Sci. Rep.* 2016, 6, 35439.

[44] Decker, M.; Kremers, C.; Minovich, A.; Staude, I.; Miroshnichenko, A. E.; Chigrin, D.; Neshev, D. N.; Jagadish, C.; Kivshar, Y. S. Electro-Optical Switching by Liquid-Crystal Controlled Metasurfaces. *Opt. Express* 2013, 21 (7), 8879–8885.

[45] Sautter, J.; Staude, I.; Decker, M.; Rusak, E.; Neshev, D. N.; Brener, I.; Kivshar, Y. S. Active Tuning of All-Dielectric Metasurfaces. *ACS Nano* 2015, 9 (4), 4308–4315.

[46] Komar, A.; Paniagua-Domínguez, R.; Miroshnichenko, A.; Yu, Y. F.; Kivshar, Y. S.; Kuznetsov, A. I.; Neshev, D. Dynamic Beam Switching by Liquid Crystal Tunable Dielectric Metasurfaces. *ACS Photonics* 2018, 5 (5), 1742–1748.

[47] Bohn, J.; Bucher, T.; Chong, K. E.; Komar, A.; Choi, D.-Y.; Neshev, D. N.; Kivshar, Y. S.; Pertsch, T.; Staude, I. Active Tuning of Spontaneous Emission by Mie-Resonant Dielectric Metasurfaces. *Nano Lett.* 2018, 18 (6), 3461–3465.

[48] Thyagarajan, K.; Sokhoyan, R.; Zornberg, L.; Atwater, H. A. Millivolt Modulation of Plasmonic Metasurface Optical Response via Ionic Conductance. *Adv. Mater.* 2017, 29 (31), 1701044.

[49] Ou, J.-Y.; Plum, E.; Zhang, J.; Zheludev, N. I. An Electromechanically Reconfigurable Plasmonic Metamaterial Operating in the Near-Infrared. *Nat. Nanotechnol.* 2013, 8 (4), 252–255.

[50] Valente, J.; Ou, J.-Y.; Plum, E.; Youngs, I. J.; Zheludev, N. I. A Magneto-Electro-Optical Effect in a Plasmonic Nanowire Material. *Nat. Commun.* 2015, 6, 7021.

[51] Ee, H.-S.; Agarwal, R. Tunable Metasurface and Flat Optical Zoom Lens on a Stretchable Substrate. *Nano Lett.* 2016, 16 (4), 2818–2823.

[52] Qazilbash, M. M.; Brehm, M.; Chae, B.-G.; Ho, P.-C.; Andreev, G. O.; Kim, B.-J.; Yun, S. J.; Balatsky, A. V.; Maple, M. B.; Keilmann, F. et al. Mott Transition in VO_2 Revealed by Infrared Spectroscopy and Nano-Imaging. *Science* 2007, 318 (5857), 1750–1753.

[53] Budai, J. D. et al. Metallization of Vanadium Dioxide Driven by Large Phonon Entropy. *Nature* 2014, 515, 535–539.

[54] Zheng, H., Wagner, L. K. Computation of the Correlated Metal–Insulator Transition in Vanadium Dioxide from First Principles. *Phys. Rev. Lett.* 2015, 114, 176401.

[55] Gray, A. X. et al. Correlation-driven Insulator–Metal Transition in Near-Ideal Vanadium Dioxide Films. *Phys. Rev. Lett.* 2016, 116, 116403.

[56] Liu, H. W.; Wong, L. M.; Wang, S. J.; Tang, S. H.; Zhang, X. H. Ultrafast Insulator–Metal Phase Transition in Vanadium Dioxide Studied Using Optical Pump–Terahertz Probe Spectroscopy. *J. Phys.: Condens. Matter* 2012, 24, 415604.

[57] Liu, H. W.; Wong, L. M.; Wang, S. J.; Tang, S. H.; Zhang, X. H. Effect of Oxygen Stoichiometry on the Insulator–Metal Phase Transition in Vanadium Oxide Thin Films Studied using Optical Pump-Terahertz Probe Spectroscopy. *Appl. Phys. Lett.* 2013, 103, 151908.

[58] Hongwei, L.; Junpeng, L.; Minrui, Z.; Hai, T. S.; Haur, S. C.; Xinhai, Z.; Lin, K. Size Effects on Metal–Insulator Phase Transition in Individual Vanadium Dioxide Nanowires. *Opt. Express* 2014, 22, 30748–30755.

[59] Mayer, B. et al. Tunneling Breakdown of a Strongly Correlated Insulating State in VO_2 Induced by Intense Multiterahertz Excitation. *Phys. Rev. B* 2015, 91, 235113.

Chapter 2

VANADIUM DIOXIDE THIN-FILM GROWTH AND CHARACTERIZATION

2.1 Vanadium Dioxide Thin-Film Growth and X-ray Diffraction

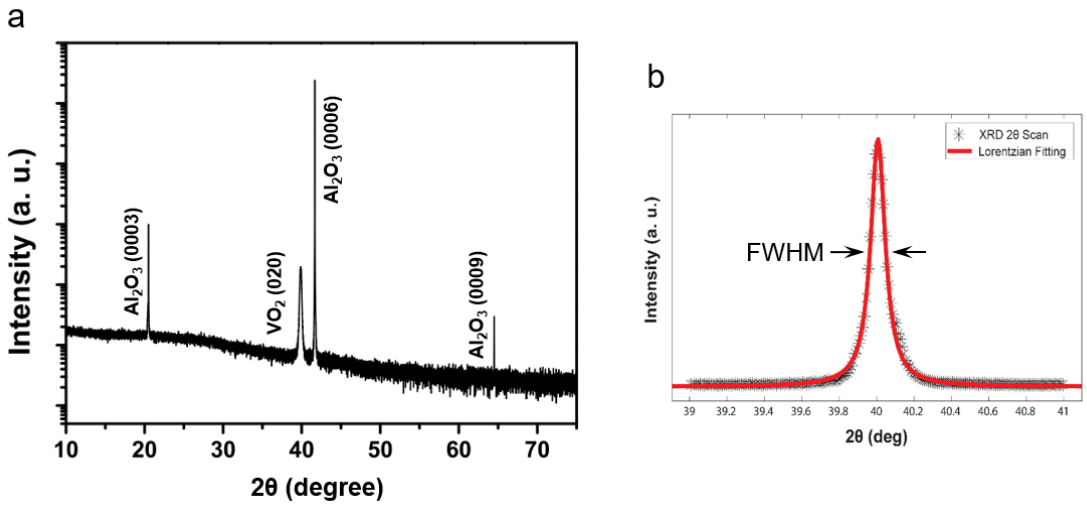

Figure 2.1. X-ray diffraction scan of the VO_2 thin film grown on a c-plane sapphire substrate using a pulsed laser deposition method. (a) The X-ray diffraction confirms the formation of a single-phase polycrystalline VO_2 film. (b) The average grain size is estimated to be at approximately 100 nm based on the Scherrer equation.

To realize high-performance devices, it is essential to develop high-quality VO_2 films. A 50-nm-thick VO_2 film was formed on the single-side polished (SSP) sapphire substrate by a pulsed laser deposition technique. A high-power pulsed laser beam vaporized the vanadium target and deposited a thin film on the sapphire substrate in the presence of 5-mTorr oxygen gas at an elevated temperature (650 °C). As a result, the target material was vaporized from the target (in a plasma plume), which deposited it as a thin film on the substrate. The film quality was analyzed by X-ray diffraction (Figure 2.1a). The result showed a diffraction peak under the Bragg condition, which confirmed the formation of single-phase polycrystalline VO_2 films. From the full width at half maximum (FWHM) of the VO_2 peak (Figure 2.1b), we extracted the average grain size of the film based on the following Scherrer equation:

$$B(2\theta) = \frac{K\lambda}{Lcos(\theta)} \tag{1.1}$$

where λ is the wavelength, θ is the diffraction angle, L is the crystal size, B is the peak width of the 2θ scan, and K is the Scherrer constant. The size of the crystal is inversely proportional to the FWHM of the peak. The average grain size of the film was calculated as approximately 100 nm.

2.2 Thin-Film Morphology

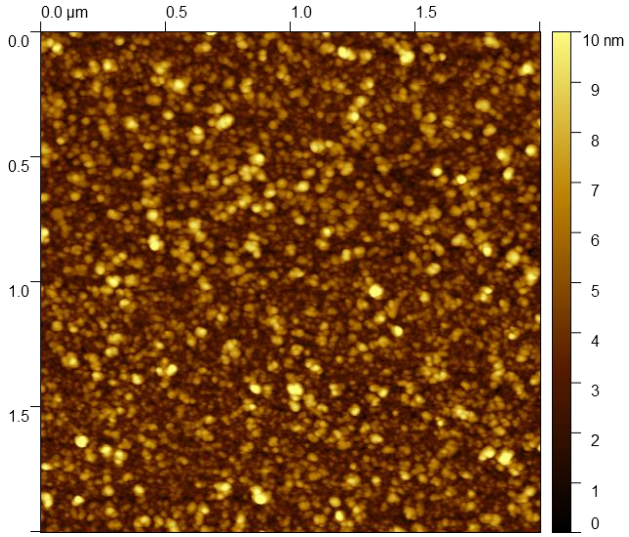

Figure 2.2. Surface characterization of VO_2 film. Atomic force microscopy measurement of VO_2 film deposited on a sapphire substrate. The result shows that the film is uniformly grown, and the root-mean-square roughness is approximately 1.5 nm (2 µm × 2 µm).

A 50-nm-thick VO_2 film was formed on a clean c-plane single-side-polished sapphire substrate by pulsed laser deposition. A high-power pulsed laser beam vaporized the vanadium target and deposited a thin film on the sapphire substrate in the presence of 5-mTorr oxygen gas at an elevated temperature (650 °C). First, the surface of the VO_2 film grown on the sapphire substrate was confirmed to be uniform and continuous, with root-mean-square roughness of approximately 1.5 nm, as measured by atomic force microscopy (AFM) (Figure 2.2). The measurement results showed that the morphology of the VO_2 film comprised smooth and continuous small grains.

2.3 Electrical Characterization

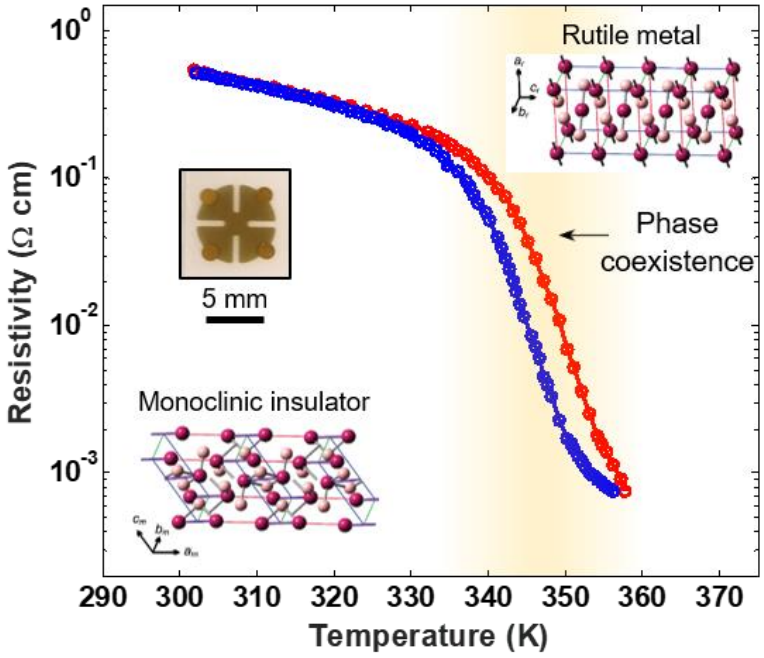

Figure 2.3. Electrical resistance hysteresis curves of the VO_2 thin film grown on a c-plane sapphire substrate. The resistance was measured based on the van der Pauw method (inset) while heating and cooling the substrate by using a thermoelectric element.

We used the van der Pauw method to measure the electrical resistance of the VO_2 film grown on the SSP c-plane sapphire substrate (Figure S1a). The temperature-dependent resistivity change across the transition was measured based on the van der Pauw method. This enabled accurate average resistivity measurement of any arbitrarily shaped sample. The temperature-dependent resistance was recorded by applying heating/cooling temperature cycles in the 300–358 K range, which was controlled using a thermoelectric element. Figure 2.3 shows the temperature-dependent hysteresis curve of resistance for a 50-nm-thick VO_2 film. We observed a drastic change in the resistance as the samples'

temperature passed the IMT temperature (T_c), which was approximately 336 K. The resistance changed by approximately three orders of magnitude across the transition, which is reversible with intrinsic hysteresis. Hysteresis originates from the elastic strain energy generated when a region undergoes nucleation while transforming. The hysteresis of a film is broader than that of bulk single crystals due to the distribution of grains, which induces mixed phases near the transition temperature.

2.4 Optical Characterization

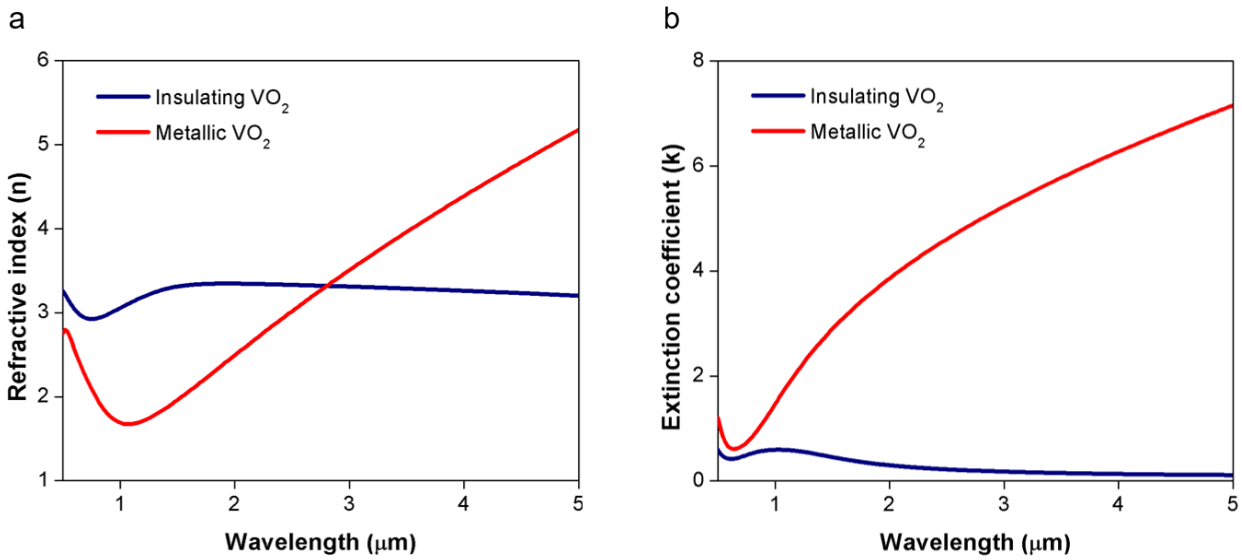

Figure 2.4. Complex refractive index of 50-nm-thick VO_2 film measured using variable-angle spectroscopic ellipsometry (a) below (at room temperature) and (b) above (at 90 °C) the phase transition temperature of the VO_2 film.

The complex refractive index of the VO_2 thin film grown on the sapphire substrate was measured using variable-angle spectroscopic ellipsometry at room temperature and 90 °C (Figure 2.4). The measured data indicated the occurrence of phase transition when the substrate was heated above the critical temperature. In the insulating phase, the extinction coefficient (k) approaches zero in the long-infrared region. In the metallic phase, however, k increases for a longer wavelength, as VO_2 behaves similarly to a metal. Therefore, in the metallic phase at longer wavelengths, k can be approximated using the Drude model.

Chapter 3

ELECTRICALLY TUNABLE OPTICAL RESPONSES OF VO_2 METASURFACES

3.1 Introduction

In this chapter, we demonstrate for the first time electrically tunable phase responses in our PCM-based metasurfaces at optical frequencies. The tunable phase responses were achieved by actively controlling the effective dielectric permittivity of VO_2, which is enabled by Joule heating. Through a strong light–matter interaction, we demonstrated continuous phase shifts by controlling the effective permittivity of VO_2 and the large maximum achievable phase shift over a wide wavelength range, which can be as high as approximately 250° near the zero-bias resonance frequency. Hysteresis curves were observed in voltage-dependent reflectance, resonance wavelength, and phase shift analyses, which opens a new area for electrically rewritable memory devices. We also reported the response time of our VO_2-based metasurface, which can be improved through thermal engineering of the device. We envision that our electrically tunable phase-change metasurface has varying potential applications, such as beam-steering for LiDAR, reconfigurable lenses, and holographic imaging, where dynamical manipulation of light is required.

Most of the previously demonstrated PCM-based metasurfaces have been used through either direct thermal control [1-8] or optical switching [9-11]. As a next frontier, electrical controllability is particularly important for future applications, such as beam-steering devices employing phased array systems with individually addressed elements and

on-chip integration with present electronics, which cannot be accomplished through direct thermal heating or optical actuation. Recently, several studies have successfully demonstrated the electrical control of amplitude modulation in visible [12], near-infrared [13], or mid-infrared [14] regions, as well as phase modulation in the millimeter-wave region, through Joule heating in VO_2. However, despite the tremendous potential, the experimental observation of PCM-based metasurfaces with continuous and large-phase tunability at near-infrared wavelengths remains elusive. A demonstration of the electrically controlled phase responses of near-infrared metasurfaces integrated with VO_2 is expected to provide a new platform to realize the wavefront manipulation functionality of PCM-based electrically tunable optical devices.

Here, we propose and experimentally demonstrate an electrically tunable PCM-based reflectarray metasurface that exhibits wide phase shifts in the near-infrared region. We directly incorporated a PCM (VO_2) into the structure as an active medium to enhance the light–mater interaction in the resonance cavity. Upon undergoing a phase transition triggered by Joule heating, the induced plasmonic resonance tuning was accompanied by a large modulation in optical responses, such as amplitude, resonance wavelength, and phase. We experimentally demonstrated a reflectance modulation of 23.5% at metallic phase resonance and a continuous phase shift of approximately 180° at a wavelength of 1550 nm, as well as a resonance shift of 175 nm upon phase transition. We found that the maximal phase shift near the insulating phase resonance was as high as approximately 250°. In addition, by measuring the active modulation at multiple wavelengths in the near-infrared region, we demonstrated that the proposed metasurface can operate over a wide wavelength range.

3.2 Device Design, Fabrication, and Electrical Modulation Mechanism

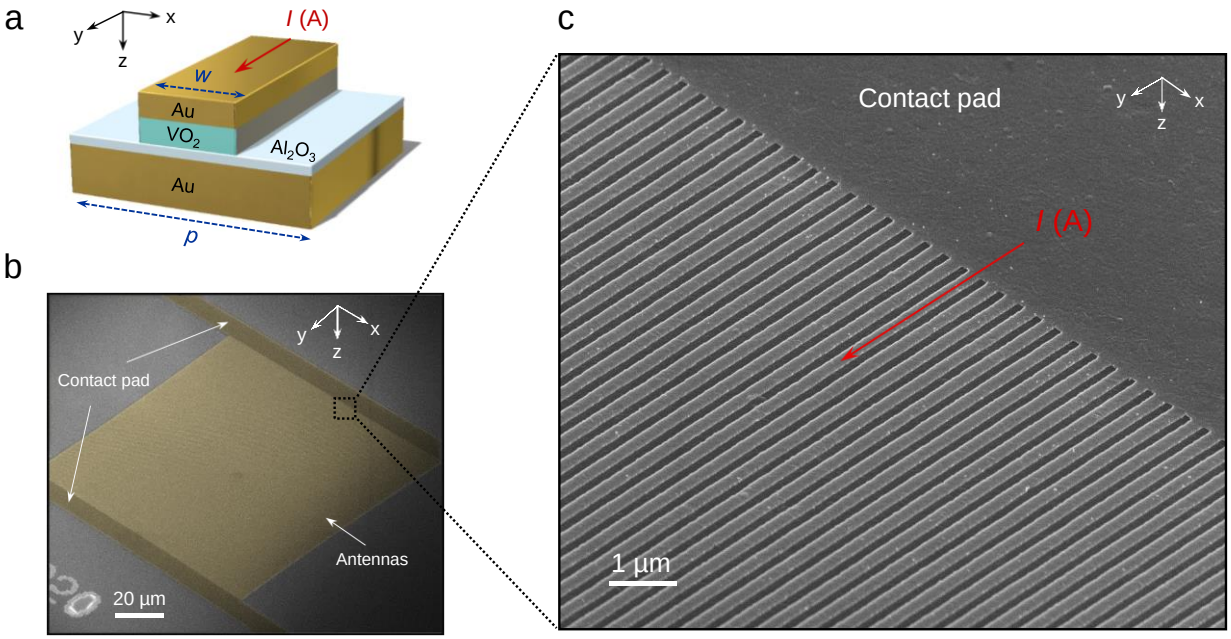

Figure 3.1. Electrically tunable VO_2 metasurface. (a) Schematic of a VO_2-based tunable metasurface unit cell comprising a metal–insulator–metal (MIM) structure. The metasurface device comprises a 40-nm-thick patterned Au stripe atop a 40-nm-thick active VO_2 stripe, a 50-nm-thick Al_2O_3 layer, and an optically thick (150 nm) Au backplane. The width (w) and period (p) of the unit cell of the metasurface are 210 and 400 nm, respectively. (b) Scanning electron microscope (SEM) image (false color) of the metasurface comprising the MIM stripe antenna and the contact pad and (c) the close-up SEM image of the MIM stripe antenna and contact pad. The top Au stripe simultaneously supports optical resonances and acts as a Joule heater through connection to external circuitry.

The unit cell of the designed metasurface was based on a metal–insulator–metal (MIM) structure, as shown in Figure 3.1a. The phase transition in VO_2 was thermally induced through Joule heating of the top Au stripe by using an external current source. In this way, the temperature of the VO_2 could be carefully controlled. We directly incorporated the active material (VO_2) into the MIM structure to enhance the interaction between the active medium

and the strongly confined field. The strong light–matter interaction in the resonance cavity of the metasurface resulted in large phase shifts of the reflected light induced by the significant change in the resonance of the unit cell. Furthermore, continuous phase shifts were obtained by manipulating the intrinsic nature of the VO_2 thin film, which yielded intermediate optical properties near the IMT.

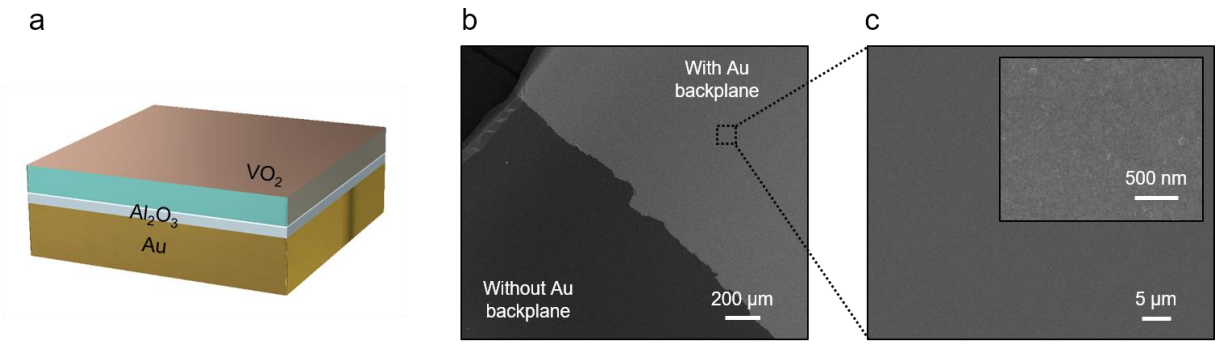

Figure 3.2 VO_2 thin film grown on a planar Au/Al_2O_3 heterostructure. (a) Schematic of the structure that comprises a 40-nm-thick active VO_2 film, a 50-nm-thick Al_2O_3 layer, and an optically thick (150 nm) Au backplane. (b) Scanning electron microscope (SEM) image of the heterostructure and (c) zoomed-in SEM image of the heterostructure with the Au backplane. The inset shows a further magnified SEM image of the continuous VO_2 film on the heterostructure, which is then patterned by the nanofabrication process.

To demonstrate this modulation mechanism, we fabricated subwavelength metallic antenna array structures incorporating the VO_2 active layer. The metasurface was fabricated on a clean fused silica substrate. First, a 150-nm-thick Au backplane was deposited on a 20-nm-thick Ti adhesion layer using electron beam deposition. Then, a 50-nm-thick Al_2O_3 layer was formed on top of the Au backplane by atomic layer deposition, followed by the formation of a 40-nm-thick VO_2 layer by pulsed laser deposition (at 650 °C in a 5-mTorr O_2 environment), which resulted in a heterostructure, as shown in Figure 3.2a. The scanning electron microscope (SEM) images of the planar heterostructure are shown in

Figure 3.2b,c. We verified that during the growth process, the heterostructure was smooth and without any crack, which could lead to the failure of the device's electrical control due to the leakage current [15]. The metasurface was patterned on the positive electron-beam resist by using electron-beam lithography, and the pattern was developed using a resist developer. Then, a 40-nm-thick Au layer and a 10-nm-thick Cr layer were deposited consecutively on the developed resist using electron beam deposition. This was followed by the formation of designed patterns using a lift-off process. Subsequently, the patterned top metal layer (Cr) was used as a hard mask for the dry etching of the VO_2 layer with a fluorine-based inductively coupled plasma-reactive ion etching (ICP-RIE) process, which yielded self-aligned MIM antenna arrays. Finally, the Cr mask was removed using a brief dry etching process, with a chlorine-based ICP-RIE process.

An SEM image of the fabricated device is shown in Figure 3.1b. The large contact pads allowed for uniform electrical connectivity to tune the device response and were wire-bonded to a chip carrier and a circuit board for electrical control. The contact pads and subwavelength antennas composed of Au were false-colored yellow, whereas the gray region corresponded to the etched fused silica substrate. The thicknesses of the layers within the stripe antenna (i.e., Au and VO_2) were both 40 nm. The 50-nm-thick Al_2O_3 layer was deposited on an optically thick Au backplane. The width and period of the MIM antenna were 210 and 400 nm, respectively. The total area of the antenna array was approximately 100 μm × 100 μm, which is larger than the incident-beam spot size. The zoomed-in SEM image of the device (Figure 3.1c) shows the connection between the stripe antennas and contact pads in greater detail.

3.3 Vanadium Dioxide Thin-Film Characterization

3.3.1 Electrical resistance measurement

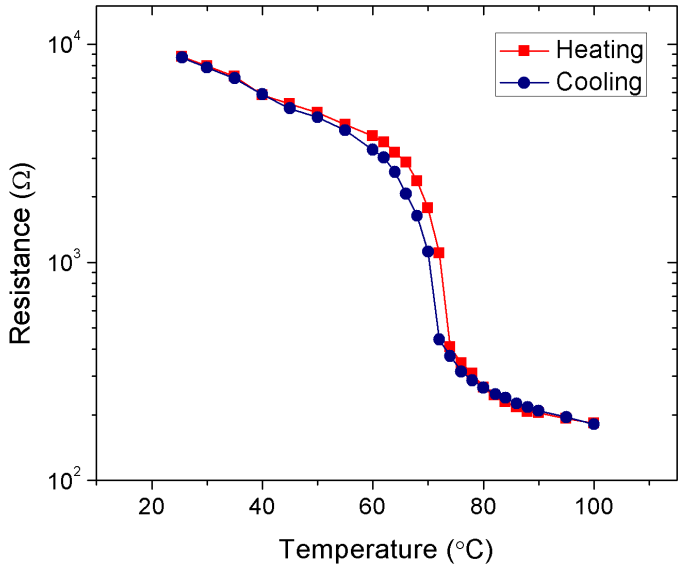

Figure 3.3. Electrical resistance hysteresis curves of the VO_2 thin film grown on the planar Au/Al_2O_3 heterostructure formed on a fused silica substrate. The resistance was measured based on the van der Pauw method during heating/cooling cycles, where the temperature was controlled using a thermoelectric element.

We used the van der Pauw method to measure the electrical resistance of the VO_2 film grown on the planar Au/Al_2O_3 heterostructure formed on the fused silica substrate (Figure 3.3). The temperature-dependent resistance was recorded by applying heating/cooling temperature cycles in the 25–100 °C range, which was controlled using a thermoelectric element. Figure 3.3 shows the temperature-dependent hysteresis curve of resistance for a 40-nm-thick VO_2 film. We observed a drastic change in the resistance as the samples' temperatures passed the IMT temperature, which is approximately 68 °C.

3.3.2 Effective optical constant: effective medium approximation

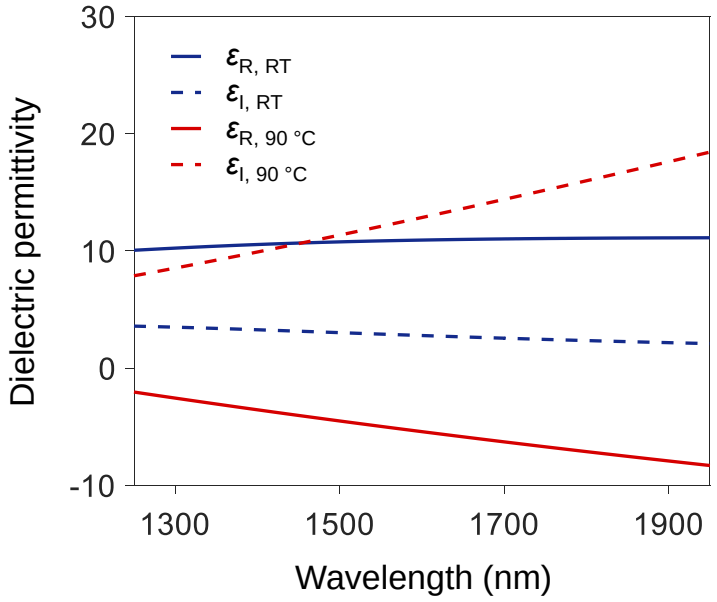

Figure 3.4. Measured dielectric permittivity of a VO_2 thin film on a sapphire substrate at room temperature and 90 °C, which indicates a phase transition. The real part of the dielectric permittivity of VO_2 (solid line) changes its sign from positive to negative upon phase transition.

To estimate the effective optical constants of the VO_2 layer used in the full-wave electromagnetic simulation, we used the Bruggeman effective medium approximation. The effective complex optical constants, $\tilde{\varepsilon}_E(\omega)$, of a two-component system in the Bruggeman model for generalized ellipsoidal inclusions are given by

$$f\frac{\tilde{\varepsilon}_r(\omega)-\tilde{\varepsilon}_E(\omega)}{\tilde{\varepsilon}_r(\omega)+\frac{(1-q)}{q}\,\tilde{\varepsilon}_E(\omega)}+(1-f)\frac{\tilde{\varepsilon}_m(\omega)-\tilde{\varepsilon}_E(\omega)}{\tilde{\varepsilon}_m(\omega)+\frac{(1-q)}{q}\,\tilde{\varepsilon}_E(\omega)}=0, \qquad (2.1)$$

where $\tilde{\varepsilon}_r(\omega)$ and $\tilde{\varepsilon}_m(\omega)$ are the wavelength-dependent complex optical constants of the rutile and monoclinic phases, respectively, as shown in Figure 3.4; f is the volume fraction of the rutile phase; and q is the depolarization factor, which depends on the shape of the inclusions. The depolarization factor is chosen based on the assumption that the rutile-phase inclusions are spherical at low concentrations, and it continuously increases under the assumption that the rutile-phase inclusions form disks at higher concentrations [16].

3.4 Simulation Results for Near- and Far-Field Analyses

3.4.1 Electric field analysis

We used finite-difference time-domain methods to simulate the periodic antenna structure under normal-incidence illumination with a transverse magnetic (TM) plane wave. Figure 3.6b shows the existence of a concentrated magnetic field magnitude $|H_y|$ in the dielectric gap of antenna elements as a result of magnetic dipole resonance. Figure 3.5a shows the enhanced z component of the electric field E_z around the right and left edges of the antenna, which are antiparallel to each other. The figure also shows the existence of an antiparallel x component of the electric field E_x around the top (light blue) and bottom (light yellow) of the dielectric gaps, which indicates an antiparallel electric field resulting from the magnetic dipole resonance. As seen in the right panels of Figures 3.5a and 3.5b, the electric fields become more localized in the Al_2O_3 layer as the VO_2 layer undergoes IMT. This tendency is consistent with the change in the magnetic-field magnitude distributions shown in Figure 3.6b as a result of perturbation in magnetic dipole resonance.

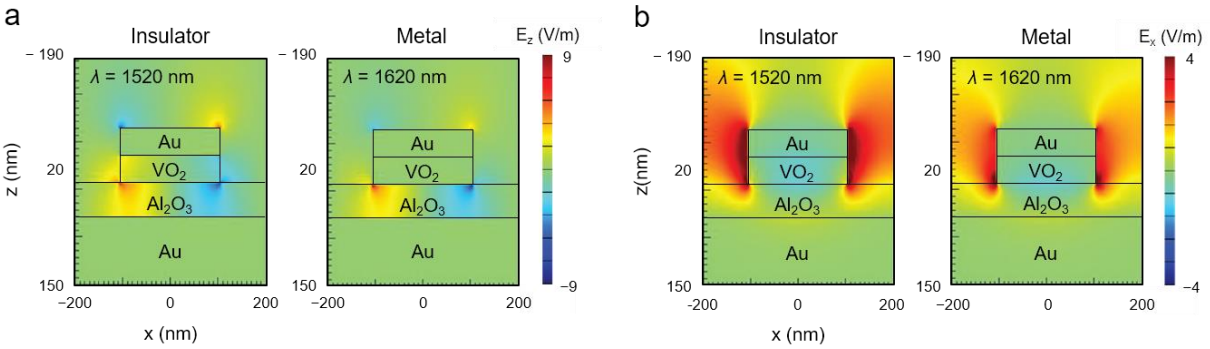

Figure 3.5. Electric field distribution of the metasurface structure. (a) Spatial distribution of the z component of the electric field E_z. (b) Spatial distribution of the x component of the electric field E_x. The left panels of each figure indicate insulating-phase resonance (λ = 1520 nm), whereas the right panels indicate metallic-phase resonance (λ = 1620 nm).

3.4.2 Reflection and phase modulation

The phase transition in VO_2 accompanies structural deformation from a monoclinic insulating phase to a tetragonal rutile metallic phase under the application of external stimuli. A thin VO_2 film comprises small grains with a broad thermal hysteresis near the phase transition threshold temperature, where the insulating and metallic phases coexist. The IMT in VO_2 is initiated by the generation of nanoscale metallic puddles at nucleation sites [16, 17], followed by the growth and connection of these puddles through a percolation process. The spatial inhomogeneity induced by the coexistence of different phases yields an averaged intermediate dielectric permittivity of the VO_2 film. In our tunable metasurface, this continuous modulation of the dielectric permittivity of the VO_2 was obtained by finely controlling the temperature by modulating the voltage applied to the Au stripes. In the simulation (Figure 3.6a), we used Bruggeman effective medium approximation (EMA) to model the intermediate dielectric permittivity of VO_2. The Bruggeman EMA was chosen as it can be applied to composites in which the inclusions cover a large range of volume fractions.

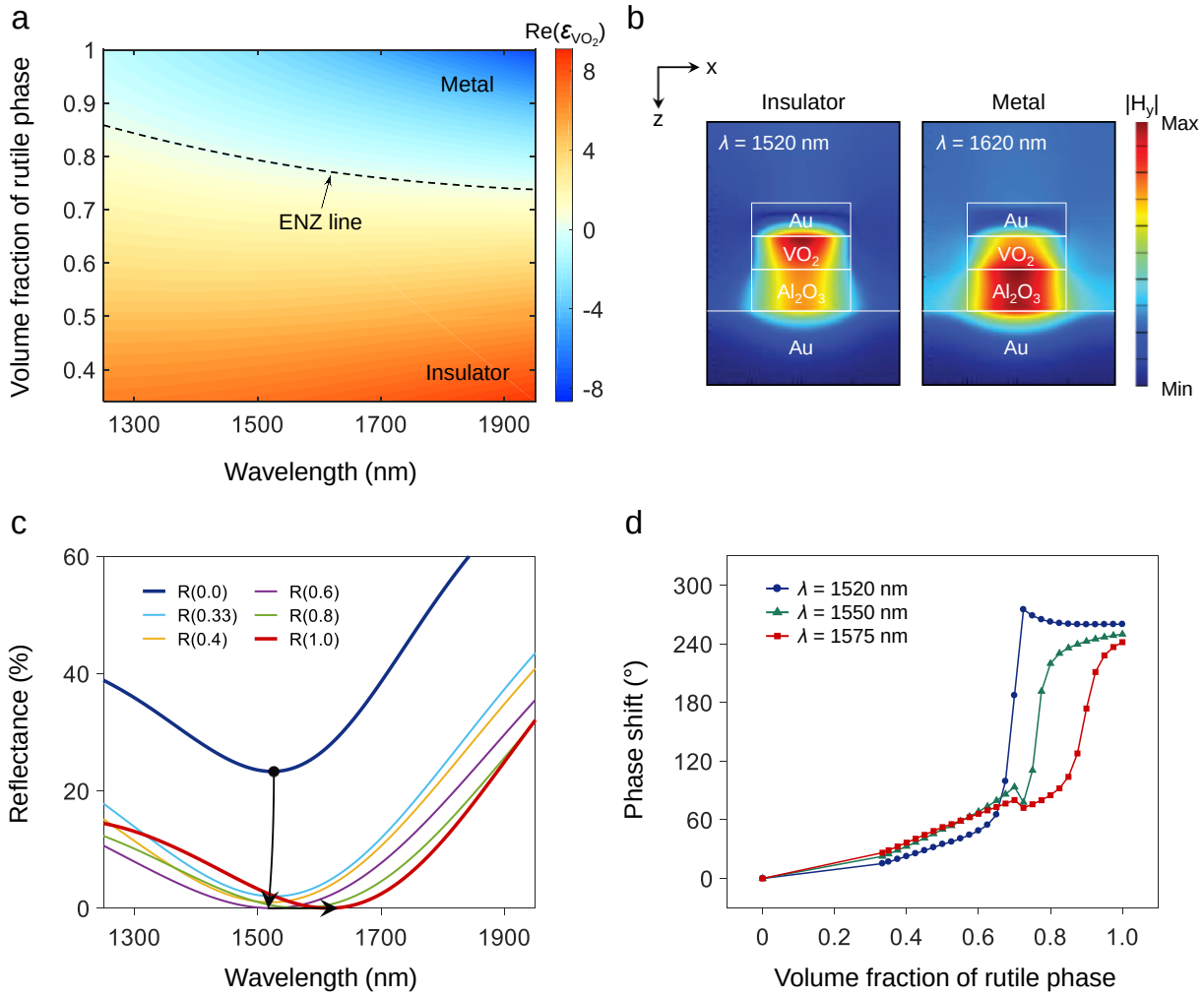

Figure 3.6. Simulation results of the active metasurface structure. (a) The real part of the dielectric permittivity of VO_2 as a function of the rutile-phase volume fraction. The intermediate dielectric permittivity is estimated based on the Bruggeman effective medium approximation. The dashed curve indicates the region in which the real part of the dielectric permittivity of VO_2 is zero. The epsilon-near-zero region implies an abrupt change in the optical properties of VO_2, as the crystal structure changes from the insulating phase to the metallic phase. (b) Magnetic field magnitude in the metasurface unit cell, with VO_2 in the insulating phase (left) and in the metallic phase (right) under normal incidence at each resonance wavelength. The incident illumination is transverse magnetic-polarized (H-field vector parallel to the stripes). (c) Reflectance spectra for different volume fractions of the rutile phase in the VO_2 layer. The legend R(0.0) corresponds to the case in which VO_2 is in a purely insulating phase, whereas R(1.0) corresponds to the case in which VO_2 is in a purely metallic phase. (d) Phase modulation as a function of the rutile-phase volume fraction in the VO_2 layer for three different wavelengths, λ = 1520, 1550, and 1575 nm.

We assumed the inclusion of rutile-phase VO_2 in the monoclinic-phase VO_2 medium and applied Bruggeman EMA for rutile volume fractions of 0.33 or greater, which is the percolation threshold of IMTs predicted from Bruggeman EMA. The optical constants of the insulating and metallic VO_2 used in Bruggeman EMA were obtained by spectroscopic ellipsometry measurements performed for a VO_2 film grown on a sapphire substrate. The real part of the effective dielectric permittivity of VO_2 modeled by Bruggeman EMA is shown in Figure 3.6a, which illustrates that the real part of the dielectric permittivity of VO_2 continuously decreases as the volume fraction of the metallic inclusion increases. The change in the sign of permittivity in the epsilon-near-zero (ENZ) region (dashed line in Figure 3.6a) indicates the change in the averaged optical properties of VO_2 from insulating to metallic. For example, at λ = 1550 nm, when the rutile fraction exceeds R(0.775), the VO_2 layer possesses negative effective permittivity, and therefore, optically functions as a metal.

Based on the predicted effective permittivity of VO_2, we performed full-wave electromagnetic simulations to understand the near- and far-field characteristics of our VO_2-based reflectarray metasurface. In the simulation results shown in Figure 3.6b–d, the optical response of the VO_2 metasurface unit cell was characterized at normal incidence under TM wave excitation. When VO_2 is in the insulating phase, the incident plane wave excites magnetic dipole resonance in the near-infrared region, which is λ = 1520 nm. As observed in the left panel of Figure 1b, the magnetic field is concentrated between the back reflector and top metallic stripe. Alternatively, when the VO_2 layer is in the metallic phase, the magnetic field is mainly confined in the Al_2O_3 layer as the effective thickness of the dielectric layer (Al_2O_3 and VO_2) decreases (the right panel of Figure 3.6b). The described change in the near-field characteristics of the supported mode is accompanied by large changes in the amplitude and phase of the reflected light. Figure 3.6c shows the change in the reflectance spectra of the metasurface as a function of the rutile volume fraction of the VO_2 phase. In the figure, R(0.0) and R(1.0) denote a purely insulating phase and a purely

metallic phase, respectively. The values in between the two pure phases indicate intermediate phases, defined by the volume fraction of the rutile phase. As the fraction of the rutile phase increases, the reflectance around the resonance dip decreases as VO_2 becomes a lossier dielectric, and the dip reaches its minimum around R(0.6). When the rutile-phase fraction becomes the dominant phase (R > 0.6), the resonance dip redshifts toward the wavelength at which the real part of effective permittivity approaches the ENZ region, as shown in Figure 3.6a. The redshift of the resonance amounts to approximately 100 nm when the VO_2 layer crosses the ENZ region and transforms into a pure rutile phase. This redshift is expected as the effective thickness of the dielectric layer shrinks when the VO_2 layer transforms into the metallic phase [18, 19]. Our simulations show that at the wavelength of the resonance dip in the insulating phase (1520 nm), the reflectance from the metasurface decreases by 23.3%. In contrast, at the wavelength of the resonance dip in the metallic phase (λ = 1620 nm), the reflectance decreases by 27.9%.

Along with the amplitude modulation upon phase transition, the full-wave simulation also predicts that a continuous-phase modulation of the reflected light can be achieved through fine control of the ratio of the coexisting phases. As shown in Figure 3.6d, a gradual change in the phase of scattered light can be obtained as the rutile volume fraction of VO_2 increases. In contrast, we observe a larger change in the phase when it approaches and crosses the ENZ region. For example, it corresponds to >R(0.75) at λ = 1550 nm, where the reflectance dip experiences a redshift at the wavelength. Furthermore, our simulations show that the designed structure exhibits a significant phase shift of approximately 260° near the insulating-phase resonance wavelength (λ = 1520 nm) when the phase of VO_2 changes from a purely insulating phase to a purely metallic phase.

3.5 Experimental Measurements

3.5.1 Reflection amplitude and resonance wavelength modulation

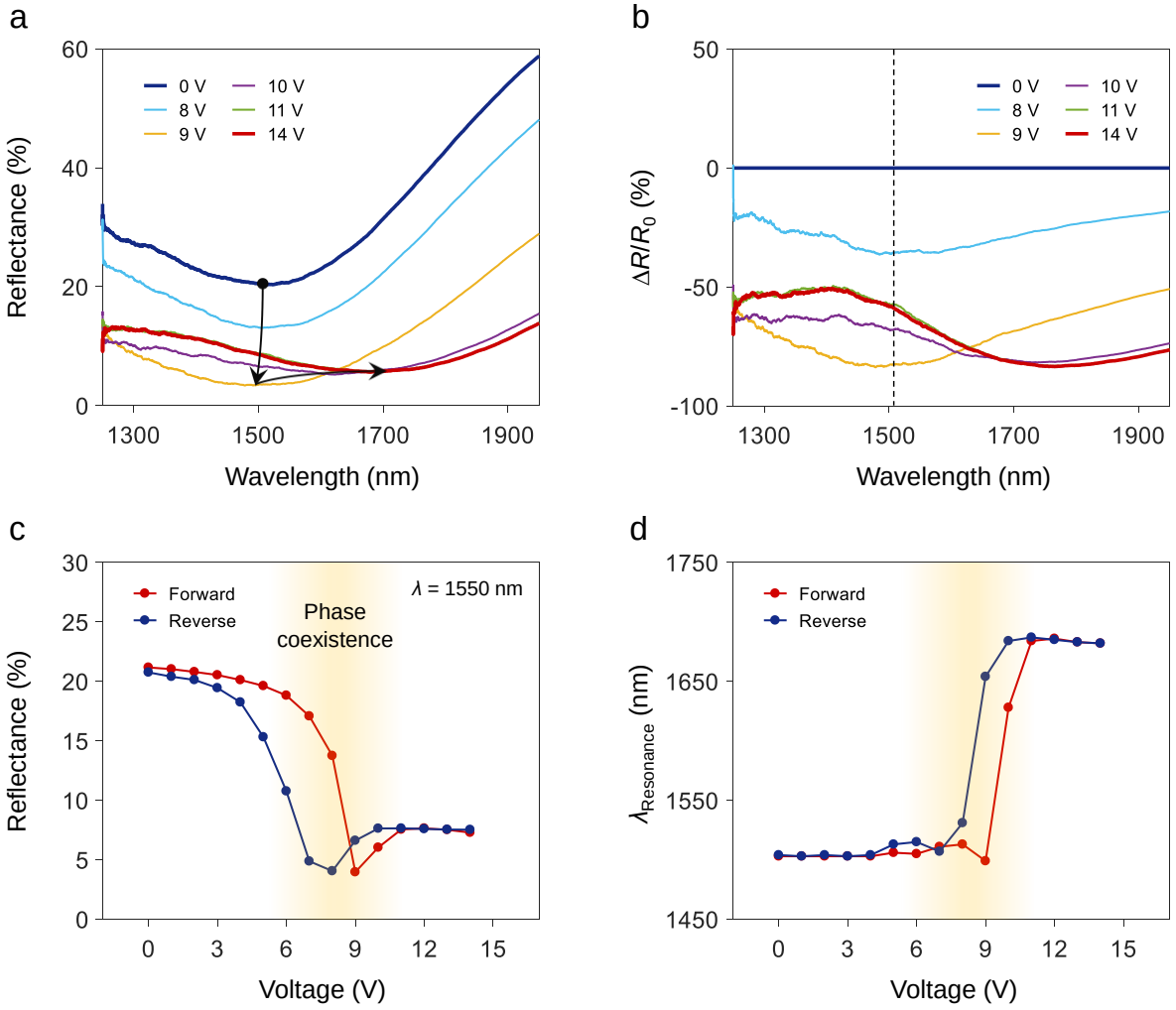

Figure 3.7. Experimental results of amplitude modulation. (a) Reflectance spectra and (b) relative reflectance change for different applied biases. The dashed line in (b) indicates the insulating-phase resonance wavelength observed in (a) at λ = 1505 nm. (c) Hysteresis loop in reflectance modulation as a function of applied bias. The reflectance is extracted at λ = 1550 nm. (d) Hysteretic behavior in voltage-dependent resonance wavelength of the reflectance spectra. The hysteresis loops are reversible upon the application of electrical bias cycles. The phase transition in VO_2 is induced by applying electrical biases on the top metal stripe for Joule heating.

To characterize an actively tunable optical response of the VO_2 metasurface, we used a Fourier transform infrared (FTIR) microscope to collect the reflectance spectra (R) for different electrical biases applied to the top metal stripes (Figure 3.7a). The absorbance (A) of the metasurface can be obtained from the relation $A = 1 - R - T$, where the transmittance (T) is negligible in the wavelength regime because of an optically thick Au backplane. The metasurface performance measured by FTIR agreed well with the full-wave simulation results (Figure 3.6c). When the VO_2 metasurface was in the insulating phase with zero bias, we experimentally observed a resonance dip at a wavelength of 1505 nm. A gradual decrease in the resonance dip was observed as the applied bias was increased up to 9 V. The simulation results indicate almost unity absorption at an intermediate state R(0.6), whereas the measured data show slightly lower absorption (96.5%) at a resonance wavelength of λ = 1505 nm. Our experimental results showed that the position of the resonance dip redshifted to approximately 1680 nm as VO_2 was fully switched to the rutile phase with a peak absorption of 94.1%. Compared to our simulation results, the fabricated device exhibited a larger shift in the resonance dip position by 175 nm and a smaller reflectance modulation (17.2% at λ = 1505 nm and 23.5% at λ = 1680 nm).

Figure 3.7b illustrates the measured relative reflectance change $\Delta R/R_0 = [R(V_a) - R(V_0)]/R(V_0)$, where $R(V_0)$ is the reflectance at zero bias ($V_a = 0$) and ΔR is the difference between the reflectance at the applied bias value and that at zero bias. We observed a large change in the relative reflectance at the resonant dip wavelengths, which correspond to purely insulating and metallic phases of VO_2. In the purely insulating phase, the relative reflectance modulation was −80%, whereas in the purely metallic phase, it was −78%. The reflectance at λ = 1505 nm (insulating-phase resonance dip position) exhibited a nonmonotonic behavior under the applied bias. This is because of the large redshift of the resonance dip when the applied bias exceeded 9 V. In contrast, the reflectance at λ = 1680

nm (metallic-phase resonance dip position) exhibited monotonic change under the applied bias.

Next, we plotted the measured reflectance at λ = 1550 nm for cyclically applied electrical bias (V_a was first gradually increased from 0 to 14 V and then gradually decreased from 14 to 0 V). We observed that the optical modulation was more pronounced when the applied voltage V_a exceeded 5 V, which corresponds to the phase transition threshold. As shown in Figure 3.7c, the reflectance at λ = 1550 nm reached its minimum value at V_a = 9 V and saturated when V_a exceeded 11 V, which implies that the VO_2 layer was completely rearranged to the rutile structure. Furthermore, hysteretic behavior was observed in the forward–reverse switching cycle. The slope of the voltage-dependent reflectance was the steepest in the hysteretic region, where the dielectric and metallic VO_2 phases coexisted. In addition, we used the results shown in Figure 3.7a to extract the spectral position of the resonance dip as a function of V_a (Figure 3.7d). As shown in Figure 3.7d, the resonance dip underwent a slight blueshift immediately before the drastic redshift, and a sharper hysteresis loop than that observed in Figure 3.7c was observed within one switching cycle.

3.5.2 Reflection-phase measurement setup

The interference fringes of the light reflected from the metasurface (Figure 3.9a) were measured using a Michelson-type interferometer, as shown in Figure 3.8. A tunable near-infrared light source was directed onto a 50–50 beam splitter after being passed through a linear polarizer. We used a white light source and a visible camera to position the incident beam on the metasurface structures. One beam was focused onto a reference mirror, whereas the other was focused at the edge of the metasurface structures to use the planar Au/Al_2O_3 heterostructure as a phase reference. By using an infrared CCD camera, we recorded interference fringes formed by the interference from the reference mirror's beam and by the sample beam from the metasurface. We post-processed the captured interference images as a function of applied bias to analyze the phase shift of the reflected light, as described in the main text.

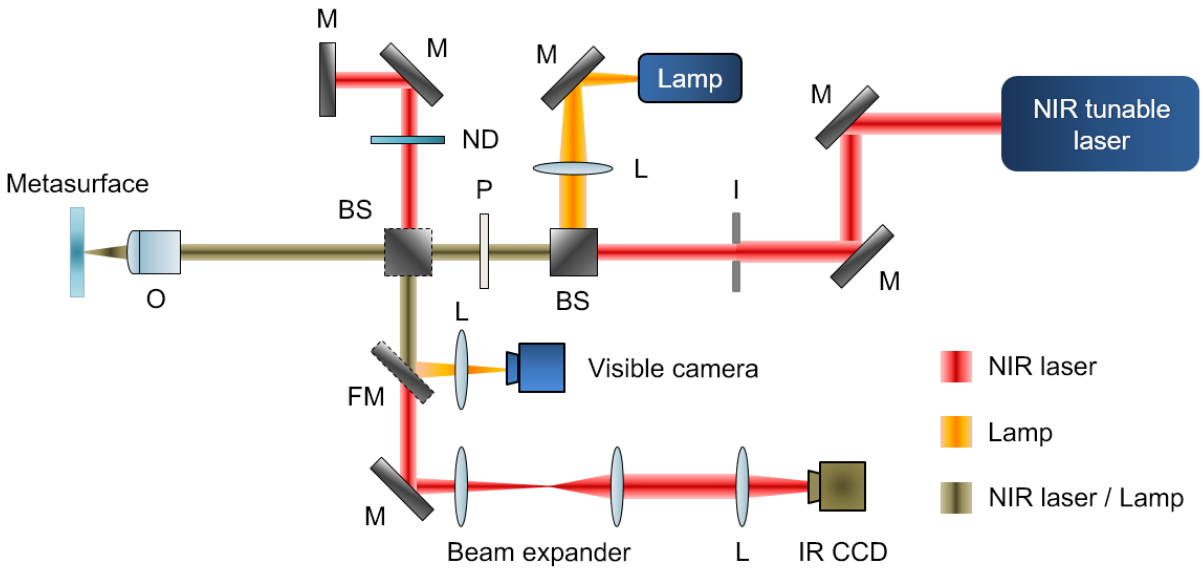

Figure 3.8. Schematic of the optical setup for the phase shift measurement. The labels of each optical component refer to the following: M (mirror); I (iris); BS (beam splitter); L (lens); P (linear polarizer); ND (neutral-density filter); FM (flip mirror).

3.5.3 Phase modulation and temporal response

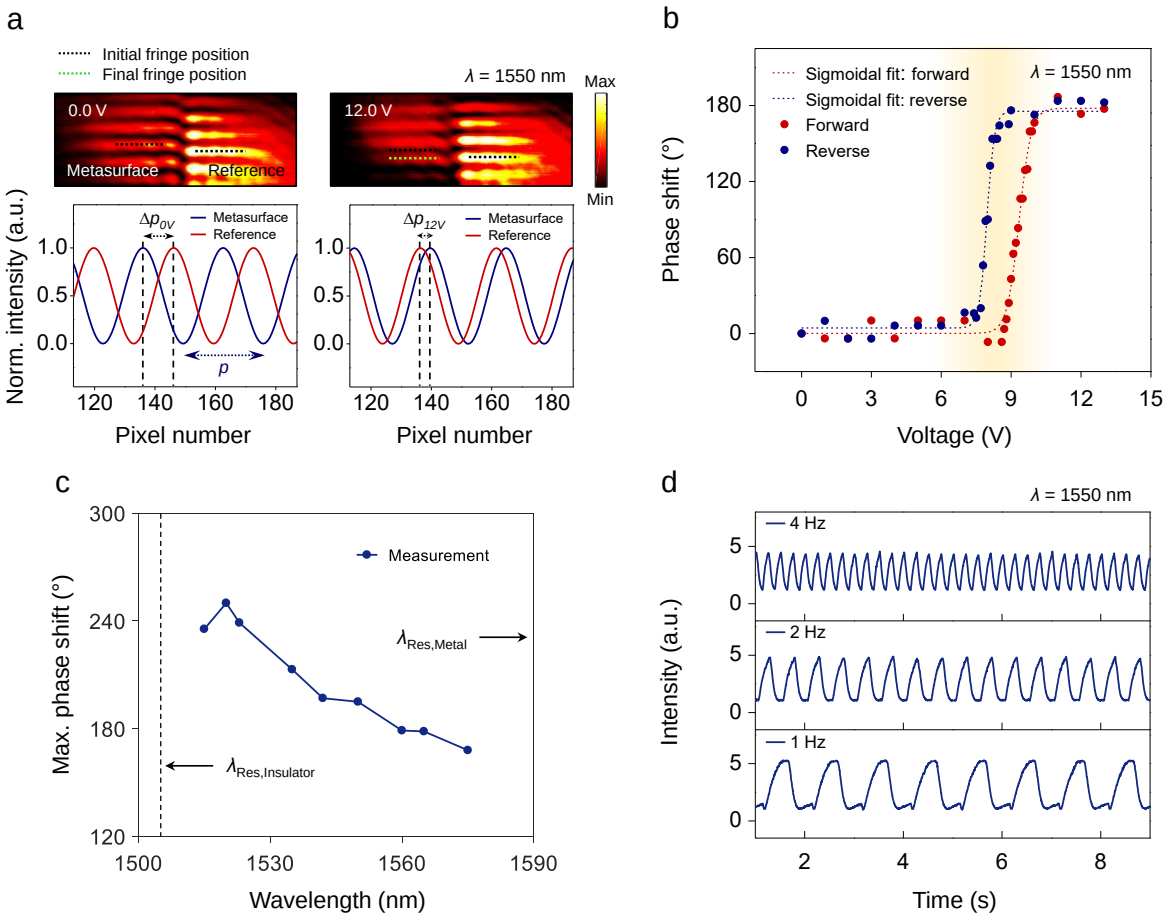

Figure 3.9. Experimental results of phase modulation and amplitude modulation speed. (a) Interference fringes for applied biases of 0 and 12 V at λ = 1550 nm. The dashed black lines indicate initial fringe positions, whereas the dashed green line shows the displacement of the metasurface fringe at V_a = 12 V. (b) Continuously tunable phase shift of the metasurface as a function of applied voltage between 0 and 13 V. This shows a reversible voltage-dependent hysteresis loop in the phase shift. (c) Maximum achievable phase shift as a function of wavelength. A larger maximum phase shift can be obtained when the operating wavelength is close to the insulating-phase resonance dip. (d) The temporal response of the metasurface is measured at λ = 1550 nm.

As indicated by our simulation results (Figure 3.6d), our metasurface not only controlled the reflectance but also provided a platform to continuously tune the phase of the reflected light. To experimentally characterize the phase response of the VO_2 metasurface, we used a Michelson-type interferometer setup (Figure 3.8). In our measurements, the incident laser beam was aligned to the edge of the metasurface structures so that half of the beam illuminated the metasurface, whereas the other half was reflected from the planar Au/Al_2O_3 heterostructure. This approach enables us to use the planar Au/Al_2O_3 heterostructure as a phase reference. The images of the interference fringes from both positions were simultaneously collected using a CCD camera. This experimental setup enabled the measurement of the relative phase between the beam reflected from the metasurface and the reference beam. The top images of Figure 3.9a show clear interference fringes at different biases, which were measured at λ = 1550 nm. The interference fringes from the metasurface structures (left-hand side) shifted downward as the applied bias was increased from 0 to 12 V. We extracted the cross-sectional profiles of the interference fringes and fitted them using sinusoids. This enabled us to calculate phase shift as a function of applied bias (bottom images of Figure 3.9a) [20, 21].

Figure 3.9b shows the phase shift result as a function of the applied bias measured at λ = 1550 nm. The applied bias was gradually increased from 0 to 13 V, which would enable fine tuning of the dielectric permittivity of the VO_2 layer from the insulating phase to the metallic phase and studying an actively tunable phase response of the metasurface. In the case of forward switching (when the applied bias was increased from 0 to 13 V), the phase started to experience a significant variation when the voltage exceeded approximately 9 V. For in-between values of $9\ V \leq V_a \leq 11\ V$, a continuous phase shift was observed with a maximum achievable phase shift of >180°. Similar to the case of voltage-dependent reflectance measurement (Figure 3.7c) and resonance dip position analysis (Figure 3.7d), we also observed a hysteresis loop when performing our phase shift

measurements within a modulation cycle. Note that the hysteresis of the voltage-dependent phase shift agrees well with that of the voltage-dependent resonance dip position analysis. This result implies that the observed large-phase modulation of the reflected light is attributable to the large modulation of the resonance characteristics of the metasurface induced by the effective dielectric permittivity tuning of the VO_2 layer. As shown in Figure 3.6a,c, the region indicating a large redshift in the resonance dip corresponds to the ENZ region, where the sign of the real part of the dielectric permittivity of VO_2 in the resonant cavity changes from positive to negative.

To further emphasize the utility of our metasurface device, the maximum achievable phase shifts as a function of wavelength are presented in Figure 3.9c. A larger phase shift can be achieved as the wavelength is close to the insulating-phase resonance wavelength (λ = 1505 nm). This tendency is consistent with the full-wave simulation results, as shown in Figure 3.6d. These results show a wide wavelength range that exhibits a phase shift of >180°, which implies that the device is not sensitive to the working wavelength, and therefore, it contributes to the device flexibility for practical applications. Furthermore, at an operating wavelength of 1520 nm, the largest phase shift of approximately 250° was achieved upon complete phase transition of the VO_2 layer, which is slightly less than the value obtained through the simulation. This deviation is primarily attributed to sample inhomogeneity and index mismatch. For example, the structural inhomogeneity in the antenna width can induce variation in the resonance characteristics of reflected light, as observed in Figure 3.6c (simulation) and Figure 3.7a (measurement). The dielectric permittivity of VO_2 used in the full-wave simulation was obtained by ellipsometry measurement of the VO_2 film grown on the sapphire substrate. Therefore, the simulation and measurement results can vary as the dielectric permittivity of VO_2 grown

on the planar Au/Al_2O3 heterostructure shows slight variation from that used in the simulation.

3.5.4 Temporal response measurement setup

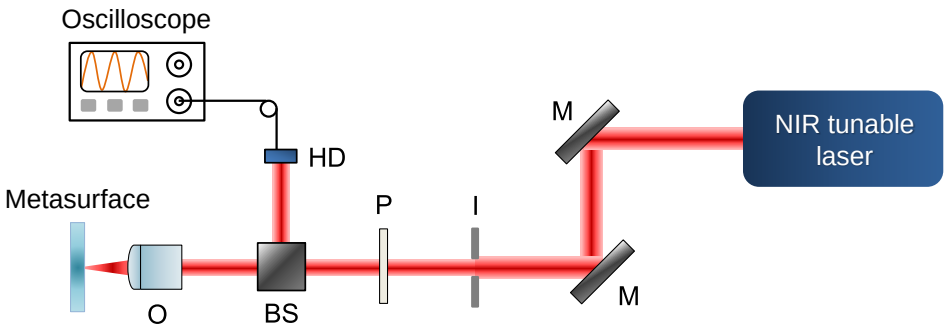

Figure 3.10. Schematic of the optical setup for the temporal response measurement. Here, HD indicates a high-speed InGaAs detector.

We measured the device's temporal response by using a function generator to modulate the reflected signal when rectangular voltage pulses were applied. The signal reflected at 1550 nm was monitored using an oscilloscope (Figure 3.10). Using the setup shown in Figure 3.9d, we performed the response time measurements of the fabricated device. To characterize the frequency response of the metasurface, 11-V rectangular voltage pulses with a 50% duty cycle were applied to the device. This electrical bias value was chosen because it represents the reflectance saturation bias value for the forward switching case, as observed in Figure 3.7c. A high-speed InGaAs detector was used to detect the reflectance from the metasurface at λ = 1550 nm. As the modulation frequency was increased beyond 2 Hz, the amplitude of the modulated signal decreased, which implies that VO_2 was not completely transformed into each phase under the application of

ac signals. The measured ON (V_a = 11 V) and OFF (V_a = 0 V) switching times were approximately 500 and 250 ms, respectively.

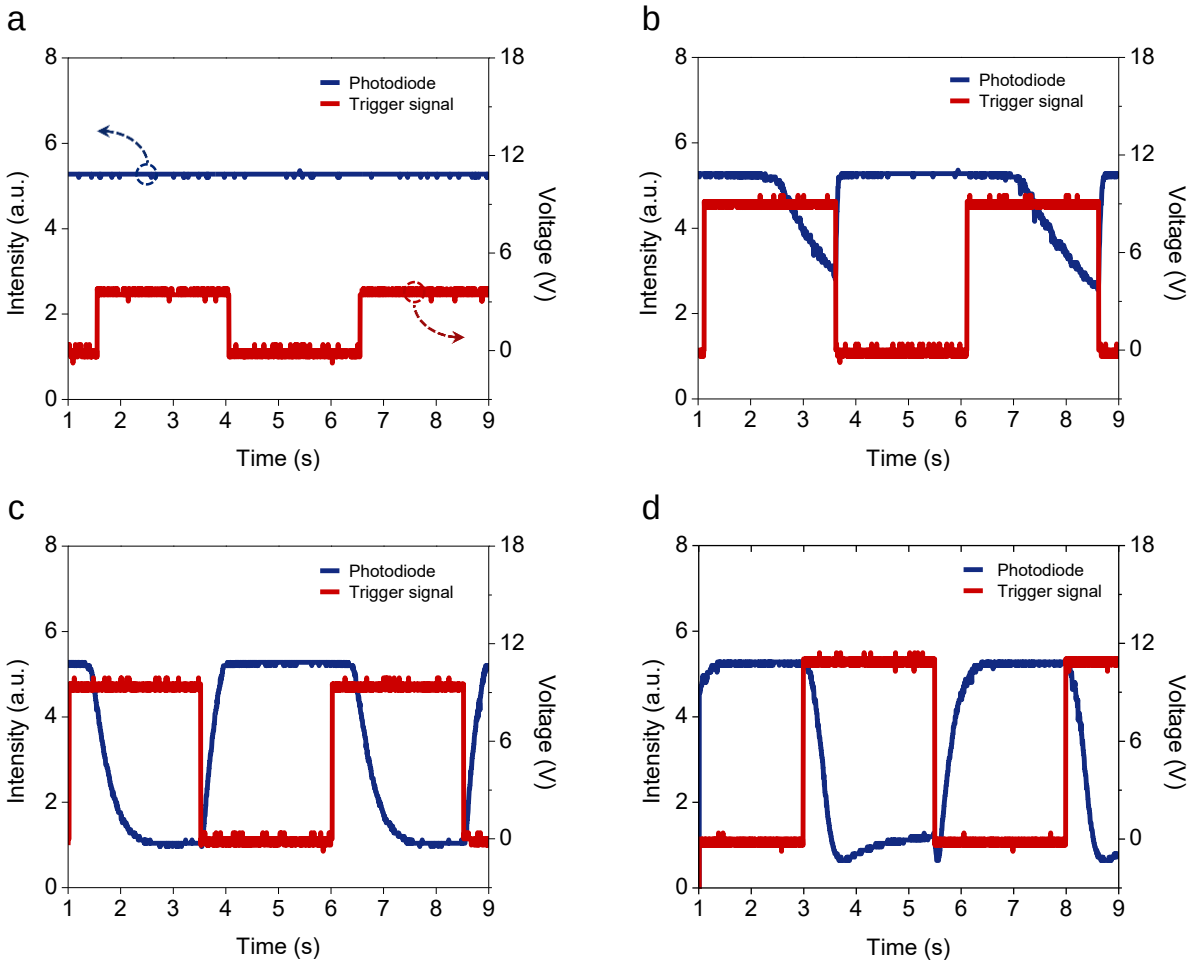

Figure 3.11. Temporal response of the metasurface for different peak-to-peak voltages: (a) 3.4, (b) 8.9, (c) 9.3, and (d) 10.9 V_{pp}. In the figures, the blue and red lines correspond to signals reflected at λ = 1550 nm and trigger signals (voltage pulses), respectively.

Figure 3.11 presents the results obtained under the application of electrical voltage pulses with 2.5 s width and 50% duty cycle for different peak-to-peak voltages. First, when the applied bias was 3.4 V_{pp} (Figure 3.11a), there was no observable change in the reflected

signal, indicating that the applied bias was below the transition threshold (Figure 3.7c). We observed a decrease in the reflected signal as we increased the bias to 8.9 V_{pp} (Figure 3.11b). The reflected signal decreased further and reached its minimum when the bias was decreased to 9.3 V_{pp} (Figure 3.11c). It saturated when the bias was 10.9 V_{pp} (Figure 3.11d), which indicates that VO_2 had completely switched to the rutile phase. We noted that the monitored nonmonotonic behavior corresponded to the steady-state responses, as shown in Figure 3.7c. At a fixed wavelength (λ = 1550 nm), the reflected signal exhibited a nonmonotonic behavior because of the redshift of the resonance dip when the applied bias exceeded 8.9 V_{pp}.

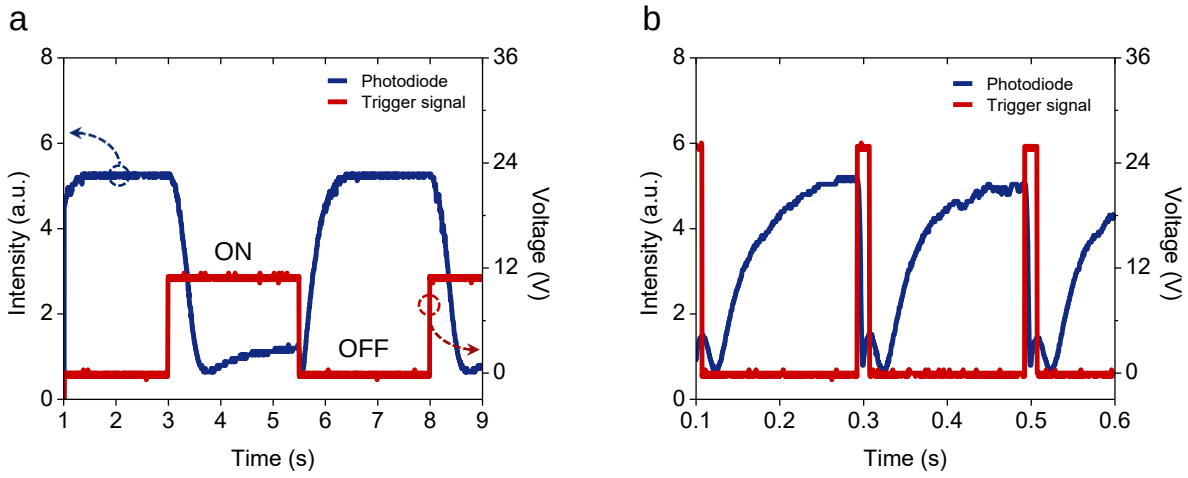

Figure 3.12. Temporal response of the metasurface for different applied voltage pulses. (a) Reflected signal for 10.9 V_{pp}-high and 2.5-s-wide voltage pulses with 50% duty cycle. (b) Reflected signal for 25.7-V_{pp}-high and 15-ms-wide voltage pulses with 7.5% duty cycle.

Note that the switching speed is not an intrinsic limit of the material. Previously, ON and OFF switching speeds of less than 1 µm and a few micrometers, respectively, were observed by reducing the heat capacity of the devices [14]. These speeds can be enhanced by applying high-intensity short pulses, which enables localized Joule heating rather than

global Joule heating, as observed previously [14, 22]. The measured ON and OFF switching times (complete phase transition) for the biases with 10.9-V_{pp}-high, 2.5-s-wide, and 50%-duty-cycle voltage pulses were approximately 2 s and 700 ms, respectively (Figure 3.12a). However, the switching speed was not limited by the intrinsic transition speed of VO_2 but by the thermal design of the device and input parameters. We noted that the previously reported switching speeds, involving thermal processes, were subpicoseconds for optical excitation [23] and a few nanoseconds for electrical switching [24]. Nevertheless, the switching speed of the metasurface could be significantly enhanced using more localized Joule heating by manipulating the applied electrical pulses [25]. For example, we observed ON and OFF switching times of approximately 10 and 100 ms, respectively, by applying high-intensity (25.7 V_{pp}) short (15 ms) voltage pulses with 7.5% duty cycle, as shown in Figure 3.12b (the OFF switching response can be further improved by reducing the heat capacity of the device and adopting a high-thermal-conductivity substrate for achieving efficient heat dissipation).

3.6 References

[1] Chen, Y.; Li, X.; Sonnefraud, Y.; Fernández-Domínguez, A. I.; Luo, X.; Hong, M.; Maier, S. A. Engineering the Phase Front of Light with Phase-Change Material Based Planar Lenses. *Sci. Rep.* 2015, 5, 8660.

[2] Tittl, A.; Michel, A.-K. U.; Schäferling, M.; Yin, X.; Gholipour, B.; Cui, L.; Wuttig, M.; Taubner, T.; Neubrech, F.; Giessen, H. A Switchable Mid-Infrared Plasmonic Perfect Absorber with Multispectral Thermal Imaging Capability. *Adv. Mater.* 2015, 27 (31), 4597–4603.

[3] Yin, X.; Steinle, T.; Huang, L.; Taubner, T.; Wuttig, M.; Zentgraf, T.; Giessen, H. Beam Switching and Bifocal Zoom Lensing Using Active Plasmonic Metasurfaces. *Light Sci. Appl.* 2017, 6 (7), e17016.

[4] Driscoll, T.; Palit, S.; Qazilbash, M. M.; Brehm, M.; Keilmann, F.; Chae, B.-G.; Yun, S.-J.; Kim, H.-T.; Cho, S. Y.; Jokerst, N. M. et al. Dynamic Tuning of an Infrared Hybrid-Metamaterial Resonance Using Vanadium Dioxide. *Appl. Phys. Lett.* 2008, 93 (2), 024101.

[5] Dicken, M. J.; Aydin, K.; Pryce, I. M.; Sweatlock, L. A.; Boyd, E. M.; Walavalkar, S.; Ma, J.; Atwater, H. A. Frequency Tunable Near-Infrared Metamaterials Based on VO_2 Phase Transition. *Opt. Express* 2009, 17 (20), 18330–18339.

[6] Kats, M. A.; Sharma, D.; Lin, J.; Genevet, P.; Blanchard, R.; Yang, Z.; Qazilbash, M. M.; Basov, D. N.; Ramanathan, S.; Capasso, F. Ultra-Thin Perfect Absorber Employing a Tunable Phase Change Material. *Appl. Phys. Lett.* 2012, 101 (22), 221101.

[7] Kocer, H.; Butun, S.; Banar, B.; Wang, K.; Tongay, S.; Wu, J.; Aydin, K. Thermal Tuning of Infrared Resonant Absorbers Based on Hybrid Gold-VO_2 Nanostructures. *Appl. Phys. Lett.* 2015, 106 (16), 161104.

[8] Dong, K.; Hong, S.; Deng, Y.; Ma, H.; Li, J.; Wang, X.; Yeo, J.; Wang, L.; Lou, S.; Tom, K. B. et al. A Lithography-Free and Field-Programmable Photonic Metacanvas. *Adv. Mater.* 2018, 30 (5), 1703878.

[9] Wang, Q.; Rogers, E. T. F.; Gholipour, B.; Wang, C.-M.; Yuan, G.; Teng, J.; Zheludev, N. I. Optically Reconfigurable Metasurfaces and Photonic Devices Based on Phase Change Materials. *Nat. Photonics* 2016, 10 (1), 60–65.

[10] Galarreta, C. R. de; Alexeev, A. M.; Au, Y.-Y.; Lopez-Garcia, M.; Klemm, M.; Cryan, M.; Bertolotti, J.; Wright, C. D. Nonvolatile Reconfigurable Phase-Change

Metadevices for Beam Steering in the Near Infrared. *Adv. Funct. Mater.* 2018, 28 (10), 1704993.

[11] Liu, M.; Hwang, H. Y.; Tao, H.; Strikwerda, A. C.; Fan, K.; Keiser, G. R.; Sternbach, A. J.; West, K. G.; Kittiwatanakul, S.; Lu, J. et al. Terahertz-Field-Induced Insulator-to-Metal Transition in Vanadium Dioxide Metamaterial. *Nature* 2012, 487 (7407), 345–348.

[12] Hosseini, P.; Wright, C. D.; Bhaskaran, H. An Optoelectronic Framework Enabled by Low-Dimensional Phase-Change Films. *Nature* 2014, 511 (7508), 206–211.

[13] Zhu, Z.; Evans, P. G.; Haglund, R. F.; Valentine, J. G. Dynamically Reconfigurable Metadevice Employing Nanostructured Phase-Change Materials. *Nano Lett.* 2017, 17 (8), 4881–4885.

[14] Liu, L.; Kang, L.; Mayer, T. S.; Werner, D. H. Hybrid Metamaterials for Electrically Triggered Multifunctional Control. *Nat. Commun.* 2016, 7, 13236.

[15] Zhu, Z.; Evans, P. G.; Haglund, R. F.; Valentine, J. G. Dynamically Reconfigurable Metadevice Employing Nanostructured Phase-Change Materials. *Nano Lett.* 2017, 17 (8), 4881–4885.

[16] Qazilbash, M. M.; Brehm, M.; Chae, B.-G.; Ho, P.-C.; Andreev, G. O.; Kim, B.-J.; Yun, S. J.; Balatsky, A. V.; Maple, M. B.; Keilmann, F. et al. Mott Transition in VO_2 Revealed by Infrared Spectroscopy and Nano-Imaging. *Science* 2007, 318 (5857), 1750–1753.

[17] Choi, H. S.; Ahn, J. S.; Jung, J. H.; Noh, T. W.; Kim, D. H. Mid-Infrared Properties of a ${\mathrm{VO}}_{2}$ Film near the Metal-Insulator Transition. *Phys. Rev. B* 1996, 54 (7), 4621–4628.

[18] Huang, Y.-W.; Lee, H. W. H.; Sokhoyan, R.; Pala, R. A.; Thyagarajan, K.; Han, S.; Tsai, D. P.; Atwater, H. A. Gate-Tunable Conducting Oxide Metasurfaces. *Nano Lett.* 2016, 16 (9), 5319–5325.

[19] Kafaie Shirmanesh, G.; Sokhoyan, R.; Pala, R. A.; Atwater, H. A. Dual-Gated Active Metasurface at 1550 Nm with Wide (>300°) Phase Tunability. *Nano Lett.* 2018, 18 (5), 2957–2963.

[20] Valente, J.; Ou, J.-Y.; Plum, E.; Youngs, I. J.; Zheludev, N. I. A Magneto-Electro-Optical Effect in a Plasmonic Nanowire Material. *Nat. Commun.* 2015, 6, 7021.

[21] Ee, H.-S.; Agarwal, R. Tunable Metasurface and Flat Optical Zoom Lens on a Stretchable Substrate. *Nano Lett.* 2016, 16 (4), 2818–2823.

[22] Driscoll, T.; Kim, H.-T.; Chae, B.-G.; Kim, B.-J.; Lee, Y.-W.; Jokerst, N. M.; Palit, S.; Smith, D. R.; Ventra, M. D.; Basov, D. N. Memory Metamaterials. *Science* 2009, 325 (5947), 1518–1521.

[23] Liu, M.; Hwang, H. Y.; Tao, H.; Strikwerda, A. C.; Fan, K.; Keiser, G. R.; Sternbach, A. J.; West, K. G.; Kittiwatanakul, S.; Lu, J. et al. Terahertz-Field-Induced Insulator-To-Metal Transition in Vanadium Dioxide Metamaterial. *Nature* 2012, 487 (7407), 345–348.

[24] Markov, P.; Marvel, R. E.; Conley, H. J.; Miller, K. J.; Haglund, R. F.; Weiss, S. M. Optically Monitored Electrical Switching in VO_2. *ACS Photonics* 2015, 2 (8), 1175–1182.

[25] Liu, L.; Kang, L.; Mayer, T. S.; Werner, D. H. Hybrid Metamaterials for Electrically Triggered Multifunctional Control. *Nat. Commun.* 2016, 7, 13236.

Chapter 4

TUNABLE NARROWBAND THERMAL EMISSION WITH VO_2-BASED METASURFACES

4.1 Introduction

In this chapter, we propose and experimentally demonstrate tunable narrowband thermal emission with reflective VO_2 metasurfaces. Generally, the thermal emission from objects is temporally invariant and spectrally broadband; however, we challenge these common notions by introducing dielectric resonant structures coupled with a thin-film-based absorbing layer. The thermal emission process can be actively tailored with a tunable absorbing layer on top of a back reflector. The optical absorption and thermal emissions from the active medium, VO_2, are controlled by an external heating stage, which induces phase transition in the tunable layer. We demonstrated polarization-dependent, narrowband, and thermally controlled absorption changes of approximately 10.8% (~84.6% relative absorption change) in the mid-infrared spectral range. Furthermore, the line shape of the emission curves was as narrow as approximately 2 nm in simulations and approximately 27 nm in experiments. Thus, this study provides a new platform to open numerous applications in the fields of thermal management, sensing, spectroscopy, imaging, and chemistry.

The mid-infrared spectral range of emission overlaps with the vibrational absorption features of many gas molecules, liquids, etc. The relationship between the thermal emission and temperature of an objective has been well-established. According to Kirchhoff's law of thermal radiation, under thermodynamic equilibrium, the emissivity of

an object equals its absorptivity. Based on this law, numerous nanophotonic absorbers have been proposed, which has propelled the realization of thermal emitters [1-7]. Though passive absorbers have been extensively applied, the functions of these devices are invariable, and thus, they cannot be tuned at will. Recently, tunable thermal emissions, which provide active control of the emission properties of devices with post-fabrication tunings, have been actively researched. Examples of metasurface designs with tunable thermal emission properties include MEMS [8], electrical tuning of ENZ mode in AlGaAs/GaAs/AlGaAs quantum wells [9, 10], graphene [11], inter-sub-band absorption modulation in quantum wells [12, 13], and optical pumping of the In(Ga)Sb layer in InAs(Sb) matrices [14].

Here, we demonstrate an active tuning of the thermal emission from VO_2-based metasurfaces. We introduced a thin VO_2 film as an absorbing layer on top of a metal reflector. The absorbing layer was coupled with a dielectric resonator, with a dielectric spacer placed between them. Upon undergoing a phase transition triggered by heating, the induced absorption tuning of the VO_2 layer was accompanied by modulation in the overall absorption of the coupled structure. We experimentally showed that the phase change in VO_2 results in absorption changes of approximately 10.8% at a wavelength of approximately 3.25 μm and approximately 6.1% at a wavelength of approximately 3.7 μm. We highlighted the narrowband absorption peak with a linewidth of approximately 27 nm, which is defined by resonant dielectric structures. The features of the designed structures are expected to be beneficial in realizing dynamically tunable narrowband filters.

4.2 Resonant Waveguide Gratings

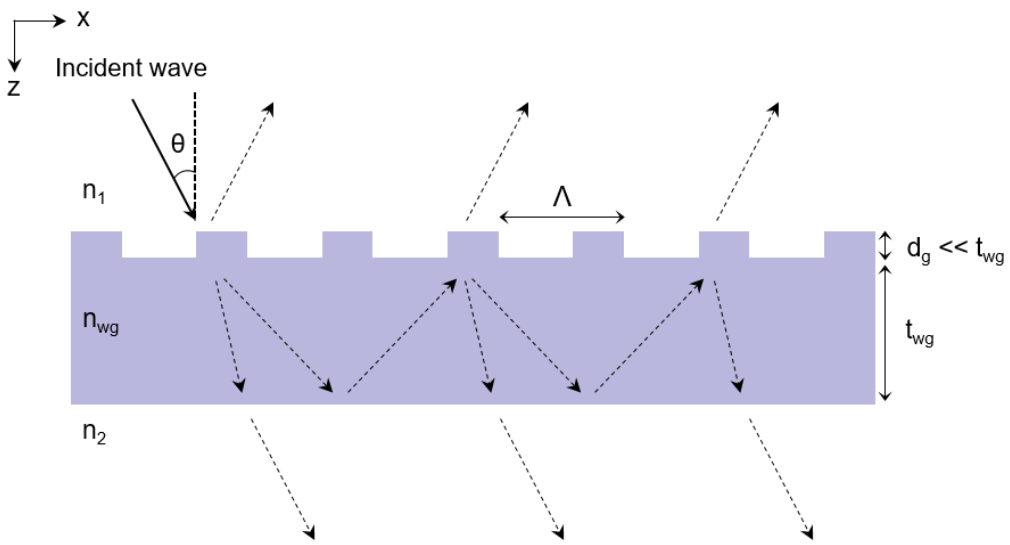

Figure 4.1. Schematic of resonant waveguide gratings.

The dielectric resonant structure of our design is composed of resonant waveguide gratings, which comprise a waveguide and a grating. They are placed in contact or in the vicinity (in optical contact). The waveguide layer usually has a higher refractive index than the surrounding media to allow light to propagate along a confined path through total internal reflection. The waveguide slab supports a discrete number of guided modes, which can be limited to the fundamental mode (zeroth mode) in very thin waveguides or comprise a few modes having different mode indices for TE and TM polarizations. In the latter case, for a given polarization and wavelength, a waveguide grating can support various guided modes having different mode indices. A plane wave is divided into multiple diffracted orders when it is incident on a waveguide grating. When the phase-matching conditions are met, the incident wave can be coupled into the waveguide modes by different grating diffraction

orders [15]. The guided modes are leaky because of index modulation in the waveguide. Therefore, they can be diffracted out (re-radiate) of the waveguide and recombined (interfere) with the propagating waves to establish a guided-mode resonance (GMR). The resonance leads to a very sharp reflection/transmission profile, and the linewidth of the efficient resonances can be as narrow as 0.1 nm [16]. In addition, the resonance is highly sensitive to the angle of incidence, polarization, material properties, and structural deviation due to the high sensitivity of the phase-matching condition.

When the grating depth of the resonant waveguide grating is very shallow compared to the slab thickness, the waveguide mode is weakly perturbed by the grating due to the weak scattering induced by the grating grooves. Under this condition, we can approximate it to an unmodulated slab waveguide, and therefore, obtain the corresponding equation of the resonant mode by setting its propagating wavevector in the slab waveguide to be equal to that of the diffracted light by assuming that the slab waveguide mode can be coupled with the diffraction grating mode [17]. The corresponding eigenvalue equations of the modulated waveguide can be obtained by referring to the eigenvalue equation of the unmodulated slab waveguide [15]:

$$For\ TE\ polarization: \qquad \tan(\kappa_i t_{wg}) = \frac{\kappa_i(\gamma_i+\delta_i)}{{\kappa_i}^2-\gamma_i\delta_i} \tag{4.1}$$

$$For\ TM\ polarization: \qquad \tan(\kappa_i t_{wg}) = \frac{{n_g}^2\kappa_i({n_2}^2\gamma_i+{n_1}^2\delta_i)}{{n_1}^2{n_2}^2{\kappa_i}^2-{n_{wg}}^4\gamma_i\delta_i} \tag{4.2}$$

where $k = \frac{2\pi}{\lambda}$, $\kappa_i = \sqrt{{n_{wg}}^2k^2 - {\beta_i}^2}$, $\gamma_i = \sqrt{{\beta_i}^2-{n_1}^2k^2}$, $\delta_i = \sqrt{{\beta_i}^2-{n_2}^2k^2}$, $\beta_i = k\left(n_1\sin(\theta) - m\frac{\lambda}{\Lambda}\right)$.

In the equations, λ is the wavelength, θ is the angle of incidence, Λ is the grating period, m is the grating diffraction order, t_{wg} is the waveguide thickness, d_g is the grating

depth, and n_1, n_g, and n_2 are the refractive indices of the superstrate, slab waveguide, and substrate, respectively. Based on these equations, we can estimate the location of a resonance peak for specific geometric parameters for TE or TM mode excitations. The resonances occur at different wavelengths due to the difference between the TE and TM eigenvalue equations, which depend on the polarization state of the incident wave for the identical waveguide grating structure. It, therefore, can also function as a polarization-sensitive device even at normal incidence. The TM mode resonance occurs at a shorter wavelength, and the structure can support multiple modes within the resonance regime.

4.3 Device Design, Fabrication, and Tuning Mechanism

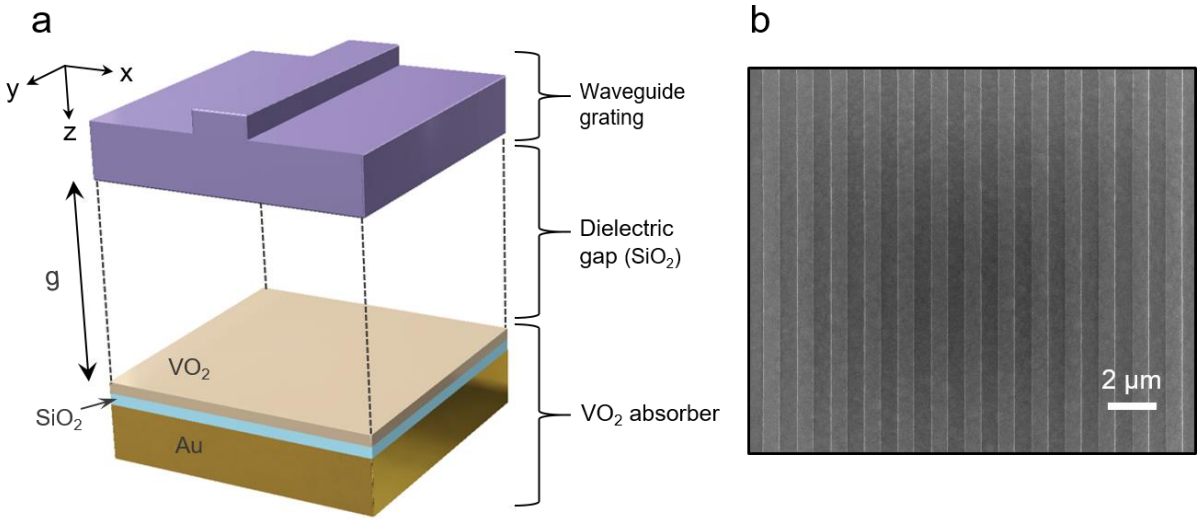

Figure 4.2. Configuration of a tunable VO_2-based metasurface for dynamic thermal emission control. (a) Schematic of a VO_2-based tunable metasurface unit cell comprising a coupled structure. (b) Planar scanning electron microscope image of the metasurface comprising the dielectric (Si) waveguide grating structure, which is coupled with a VO_2 absorber with a dielectric gap in between them. The VO_2 absorber functions as an active layer whose optical properties can be tuned by heating the substrate.

A unit cell of the designed metasurface structure is shown in Figure 4.2a. The absorbing layer comprises a VO_2 layer atop a SiO_2 layer and an optically thick Au backplane. The resonant waveguide grating layer comprises a 1.36-μm-thick Si waveguide slab and a 100-nm-thick Si grating with a duty cycle of 0.5. The period of the unit cell of the grating structure is 1.35 μm. The dielectric gap between the two layers is filled with a SiO_2 layer grown by a plasma-enhanced chemical vapor deposition (PECVD) method. The phase transition in VO_2 is thermally induced using an external heating stage. We varied the thickness of the

dielectric gap to investigate its effect on absorption resonance, which resulted in different line shape profiles.

We deposited a 20-nm-thick Ti adhesion layer on a Si substrate, followed by a 150-nm-thick Au reflector using electron beam deposition. Then, a 30-nm-thick SiO_2 layer was formed on top of the Au reflector using atomic layer deposition, followed by the formation of a 60-nm-thick VO_2 film by pulsed laser deposition. A dielectric gap layer (SiO_2) was deposited on the VO_2 film, followed by the deposition of a 1.36-μm-thick Si layer by PECVD. The grating structure was patterned on a positive electron-beam resist using e-beam lithography, and the pattern was developed using a resist developer. The patterned top resist layer was subsequently used as an etching mask for the dry etching of the Si layer with a fluorine-based ICP-RIE process. This process yielded a 100-nm-thick Si grating structure atop a Si waveguide slab. Figure 4.2b shows the planar SEM image of the fabricated structure and confirms the formation of well-defined grating structures with a grating period of 1.35 μm at a duty cycle of 0.5.

4.4 Simulation Results for Near- and Far-field Analyses

4.4.1 Optical characteristics of waveguide gratings

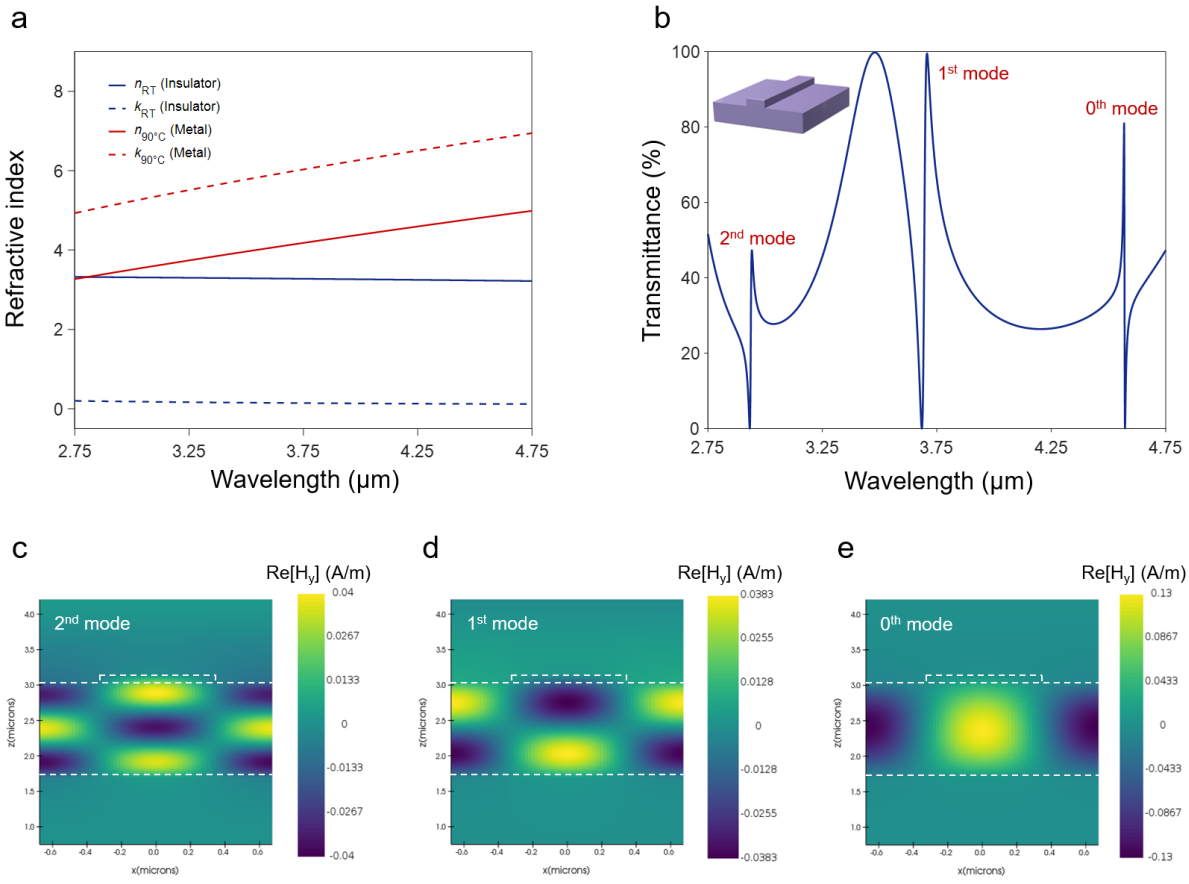

Figure 4.3. Simulation results of the waveguide grating structure. (a) Measured complex refractive index of VO_2 film using spectroscopic ellipsometry for both VO_2 phases. The extinction coefficient (k) of the insulating-phase VO_2 is close to zero, whereas that of the metallic-phase VO_2 is significantly larger, which implies an abrupt optical property change from the insulator to metal. (b) Transmission spectra for the waveguide grating structure under TM-polarized incidence. The structure exhibits three resonance features within the wavelength range. (c–e) Magnetic field profiles, Re[H_y], at three wavelengths, λ = 2.96, 3.71, and 4.6 μm, corresponding to the resonance of the second, first, and fundamental excited modes, respectively.

Figure 4.3 shows the numerical simulation results obtained for the resonant waveguide gratings using FDTD. The thickness of the waveguide slab was 1.36 μm, the period of grating was 1.35 μm, and the duty cycle was 0.5. We used the shallow grating depth (100 nm) to obtain narrowband resonances by minimizing the scattering losses that resulted in a lower quality factor and broad resonances. The designed waveguide structure was sufficiently thick to support higher-order modes under normal incidence illumination with TM-polarized light. As a result, we observed multiple guide-mode resonances excited at different frequencies, which agree well with the solution of Eq. (4.2). Furthermore, the field profiles Re[H_y] at the three resonance wavelengths were confirmed to correspond to the resonances of the fundamental, first-order, and second-order modes, respectively.

4.4.2 Absorption modulation: bare absorber vs. coupled structure

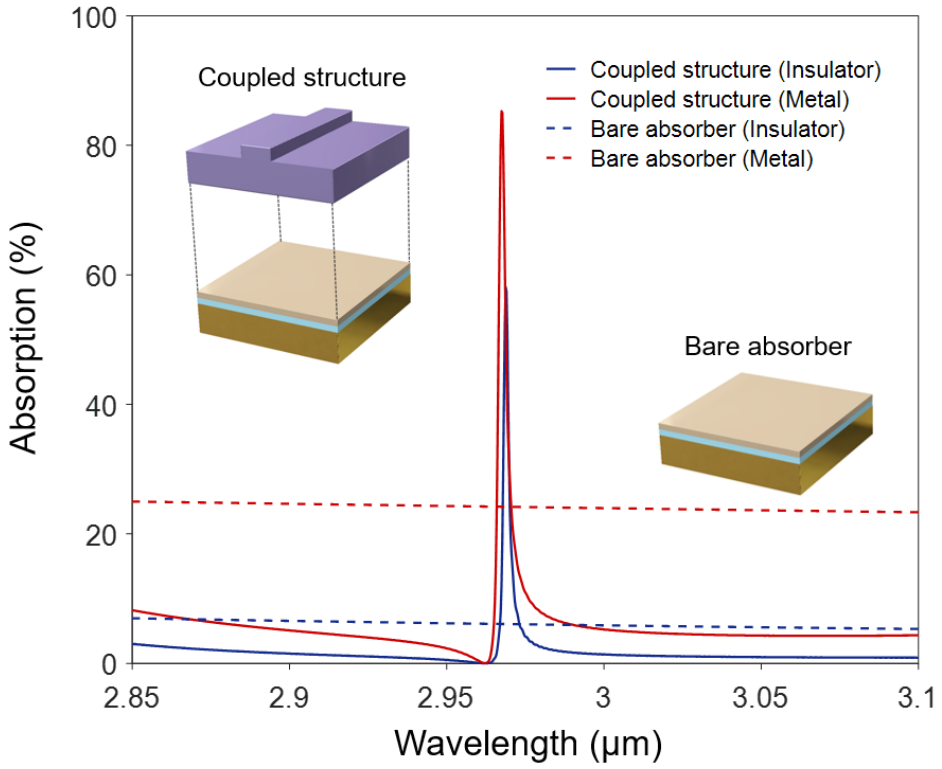

Figure 4.4. Simulation results of the absorption spectra of the coupled structure (g = 1.6 μm) and bare absorber for the insulating and metallic VO_2 phases. The absorption peaks correspond to the second-order GMR modes.

First, we analyzed the optical responses of the bare VO_2 film using the refractive index measured in the mid-infrared region for both VO_2 phases (Figure 4.3a). We performed full-wave simulations under normal incidence for TM-polarized light. The absorption spectra of the VO_2 film exhibited broad absorptions without any resonance feature. The film, however, performed as an efficient absorption modulator upon the VO_2 phase transition without any complicated feature. For example, it showed a modulation depth (ΔA) of approximately 18.1% for the second-order GMR mode ($\lambda \approx 2.97$ μm). The solid curves in Figure 4.4 show

the absorption spectra of the unit cell when the VO_2 absorber was coupled to the waveguide grating structure with a dielectric gap in between them (top left inset). At g = 1.6 μm, the coupled structure exhibited sharp resonance features arising from the GMR of the waveguide grating. The simulation results showed that at the resonance peak wavelength, the absorption from the coupled structure increased by 27.2% upon phase transition, indicating the enhancement of the modulation depth compared to that of the bare absorber. Furthermore, we observed a large change of approximately 46.8% in the relative absorption at the resonance, based on the equation $\Delta A/A_{\text{Insulator}} = (A_{\text{Metal}} - A_{\text{Insulator}})/A_{\text{Insulator}}$, where $A_{\text{Insulator}}$ is the absorption for the insulating-phase VO_2 and ΔA is the absorption difference between the metallic- and insulating-phase VO_2. More importantly, narrow spectral widths could be obtained from the coupled structure. The resonant spectra showed the FWHM of approximately 2 and 3 nm for the insulating and metallic phases, respectively. In the following section, we reveal that the FWHM can be enhanced (by less than 0.5 nm) by introducing a higher-Q resonance condition, whereas the modulation depth is significantly reduced due to the near-perfect absorption for both VO_2 phases.

4.4.3 Effect of dielectric gap height

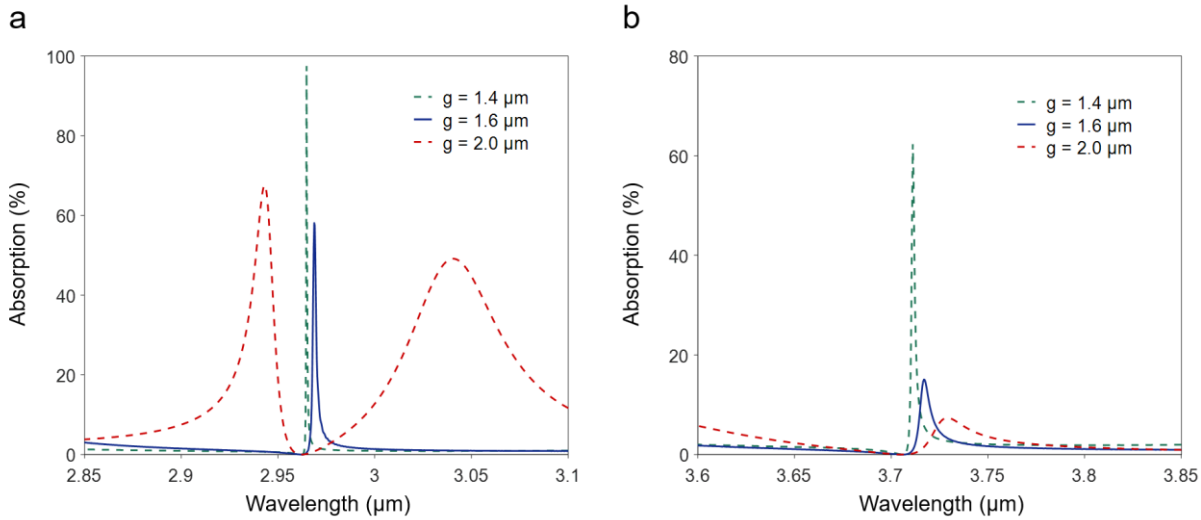

Figure 4.5. Simulation results of absorption profile variations depending on the dielectric gap height for the (a) second mode and (b) first mode. The simulations assume insulating-phase VO_2.

We performed full-wave simulations to investigate the effect of the dielectric gap height on the profile of the absorption curves. The change in the gap height was accompanied by large changes in the line shape of the absorption spectra. The optical response of the unit cell structure was characterized at normal incidence under TM-polarized wave excitation for the insulating-phase VO_2. In Figure 4.5, g denotes the gap height, and we adopted g = 1.6 μm for our optimal design. At a smaller gap height (g = 1.4 μm), the simulated spectra exhibited larger amplitude and sharper line width for both resonances (second mode (Figure 4.5a) and first mode (Figure 4.5b)), which indicate stronger resonances with higher quality factors. However, the absorption amplitudes were too large even for insulating-phase VO_2, which inhibited a clear observation of amplitude modulation upon phase transition. This is especially significant for second-order resonance, where $A(\lambda = 2.96\ \mu m) \approx 100\%$. In contrast, as the gap height was increased (g = 2.0 μm), the absorption spectra

around the resonance became broader for both modes, as they overlapped with the broad absorption peaks. The broad absorption peaks resulted from the Fabry-Perot-like resonance formed in the dielectric gap, where a thin lossy medium (VO_2 film) was located inside the gap. At g = 2.0 μm, the GMR peaks were located more closely to the broad absorption peaks. The broadening became more significant as the gap height was further increased. Therefore, we adopted g = 1.6 μm while fixing the other geometric parameters, such as the period, duty cycle, and waveguide thickness.

4.5 Experimental Measurements

4.5.1 Absorption modulation and hysteresis loop

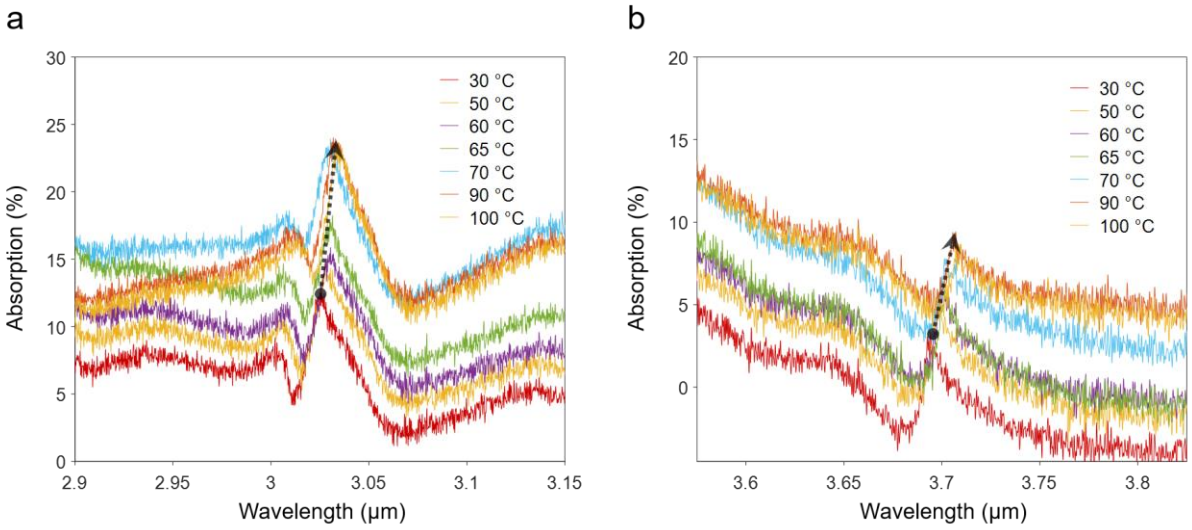

Figure 4.6. Experimental results of dynamic control of thermal emission. Absorption spectra corresponding to (a) the second guided-mode resonance (GMR) and (b) the first GMR mode. A gradual modulation in the resonance peak is observed as the temperature exceeds the phase transition temperature.

As a next step, we presented dynamic thermal emission control by applying a thermal bias to the VO_2-based metasurface. We used an FTIR microscope to obtain the absorption spectra (A) at different substrate temperatures from the fabricated samples (Figure 4.6). The absorption (A) of the metasurface can be obtained from the relation $A = 1 - R - T$. We assumed that the transmittance (T) is negligible in the wavelength regime because of the use of an optically thick metal (Au) reflector. The performance of the metasurface measured by FTIR was found to be in good agreement with the full-wave simulation results (Figure 4.4) in terms of the GMR locations and asymmetric line profiles. When the VO_2 metasurface was in the insulating phase at room temperature, we experimentally observed

a resonance peak at wavelengths of 3.02 and 3.69 μm, which corresponded to the resonances of the second and first excited modes, respectively. A gradual increase in the resonance peak was observed as the temperature was increased to 100 °C, indicating that a gradual structural deformation of VO_2 from the monoclinic insulating phase to the tetragonal rutile metallic phase occurred upon continuous heating. In the second mode ($\lambda \approx 3.02$ μm), the position of the resonance dip redshifted to approximately 10 nm as VO_2 was fully switched to the metallic phase with a peak absorption of approximately 23.6%. These spectral redshifts were attributable to the thermos-optic effect of Si, which induces a slight variation in the refractive index as the temperature increases. Compared to our simulation results, the fabricated sample exhibited a smaller absorption modulation (~10.8% for the second mode and ~6.1% for the first mode). Furthermore, we confirmed a large change of approximately 84.6% in relative absorption when comparing the maximal absorption at each resonance location for the second mode. Furthermore, we obtained narrow spectral widths from the coupled structure. The FWHM of the second-mode insulating phase was approximately 27 nm. This line width is very sharp compared to the typical thermal emission curves; the discrepancy between the simulation results will be discussed in the following section.

Next, we plotted the absorption measured at the second-mode resonance ($\lambda \approx 3.02$ μm) for cyclically changed substrate temperature (temperature was first gradually increased from 30 °C to 100 °C and then gradually decreased from 100 °C to 30 °C). The optical modulation was found to be more pronounced when the temperature exceeded 60 °C, which corresponds to the phase transition threshold. As shown in Figure 4.7, the absorption at the resonance reached its maximum value at 75 °C and saturated when the temperature exceeded this value, which implies that the VO_2 layer was completely changed to the metallic phase. Furthermore, hysteretic behavior was observed in the heating–

cooling cycle. The slope of the temperature-dependent absorption variation was most rapid in the hysteretic region, where the insulating and metallic VO_2 phases coexisted.

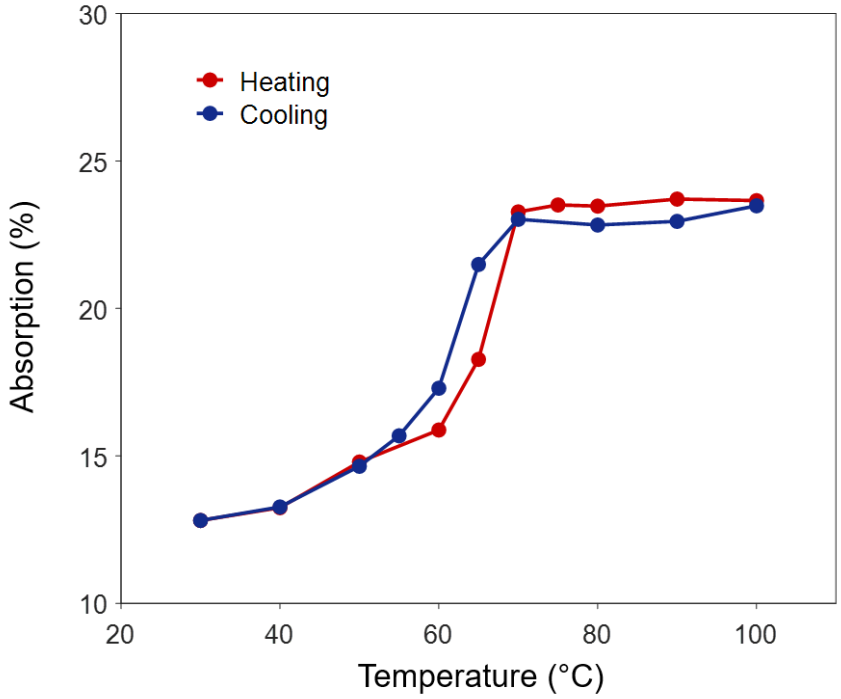

Figure 4.7. Hysteresis loop in absorption modulation as a function of temperature. The absorption is extracted at the second guided-mode resonance mode with a peak location of $\lambda \approx 3.02$ μm. The slope of the temperature-dependent absorption variation is most rapid in the hysteretic region, where the insulating and metallic VO_2 phases coexist.

To confirm the simulation results, we fabricated samples with different gap heights: g = 1.6 and 2.0 μm (Figure 4.8). The fabricated structures were characterized using an FTIR microscope to collect the absorption spectra. Figure 4.8 shows the measured spectra for the insulating-phase VO_2. The resonance locations and trends depending on the gap height of the measured spectra agreed well with the full-wave simulation results (Figure 4.5). When the gap height was increased from 1.6 to 2.0 μm, we experimentally observed broader absorption peaks for the second mode (Figure 4.8a) and first mode (Figure 4.8b).

In the following section, we will discuss the discrepancy between the simulations and experiments, especially the broader line width observed in the experimental results.

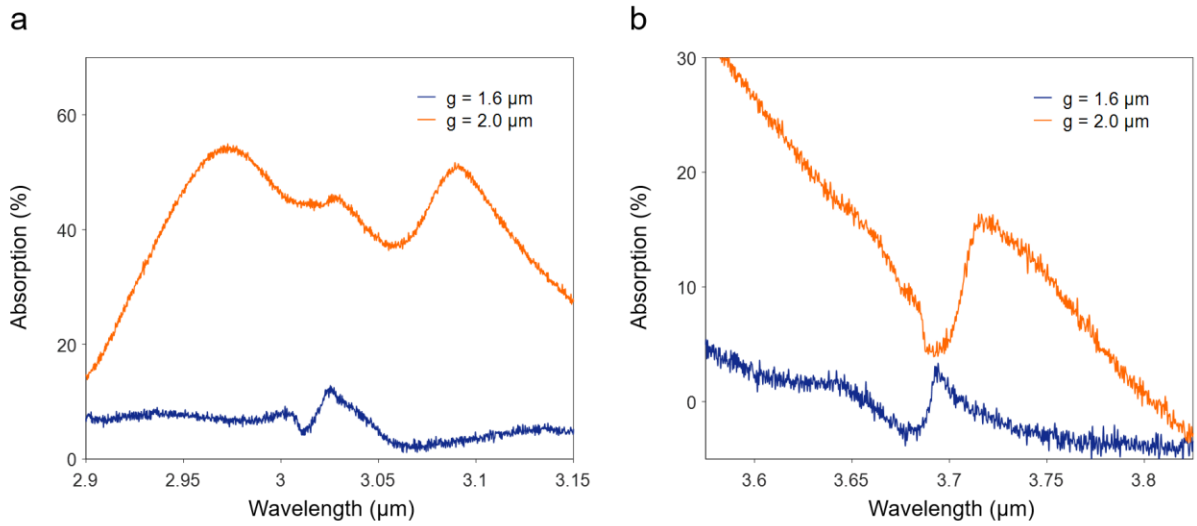

Figure 4.8. Experimental results of absorption spectral profile variation depending on the dielectric gap height for the (a) second mode and (b) first mode. In the experiments, we measured the spectra at room temperature, which implies that VO_2 is in the insulating phase.

4.5.2 Effect of broad angular distribution

The locations and modulation trends of the GMR resonances measured by FTIR agreed well with the full-wave simulation results and analytical calculations. However, the experimental results shown in Figure 4.7 differed from the simulation results in several important ways. The measured absorption spectra were lower in amplitude and broader in spectral width than the simulation results. These features can be attributed to several factors that distinguish measurements from simulations. The incoming light was illuminated by a high numerical aperture (NA) (0.58) objective lens, which produced a broad incident angle ranging from −35° to 35°. The broad angular distribution of the incident light resulted in

reduced absorption and a broader spectral width, as GMR is highly sensitive to the incident angle and grating period.

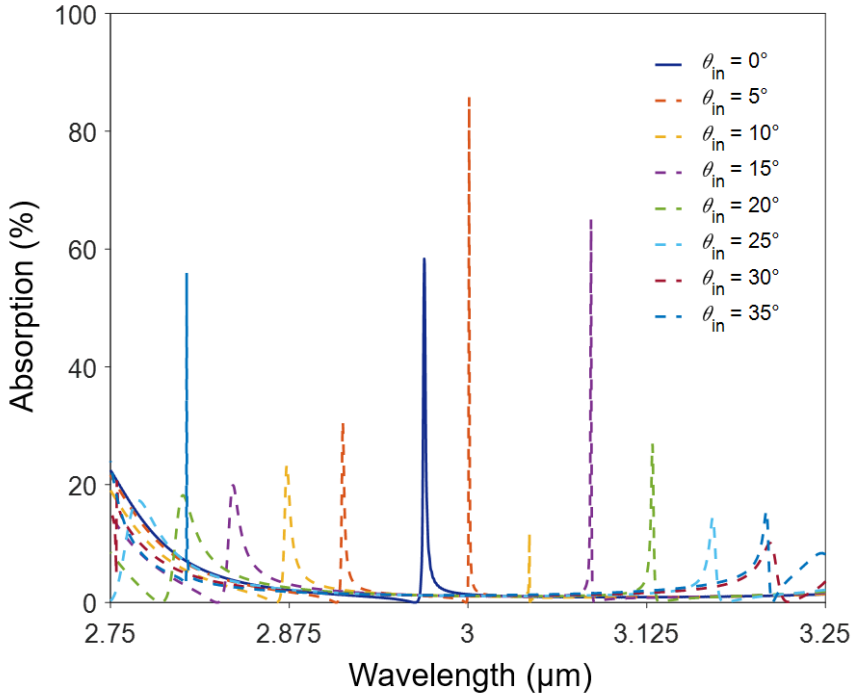

Figure 4.9. Simulation results of incident angle dependence. At a nonzero angle of incidence, $i = \pm 1$ diffracted orders are distinguishable. The guided-mode resonance is highly sensitive to the incident angle, and the resonance locations move farther away from the normal incidence resonance location as the incident angle increases.

To understand the effect of the broad angular distribution, we performed full-wave simulations for the incident angle ranging from −35° to 35°. First, we observed the split of the GMR peak ($\lambda \approx 3$ μm) into two peaks, which were located away from the original resonance. As the incident angle increased, the peaks moved farther away from the original peak location. The resonance induced by $i = \pm 1$ diffracted orders was distinguishable at a nonzero angle of incidence, which indicates degenerate resonance [18].

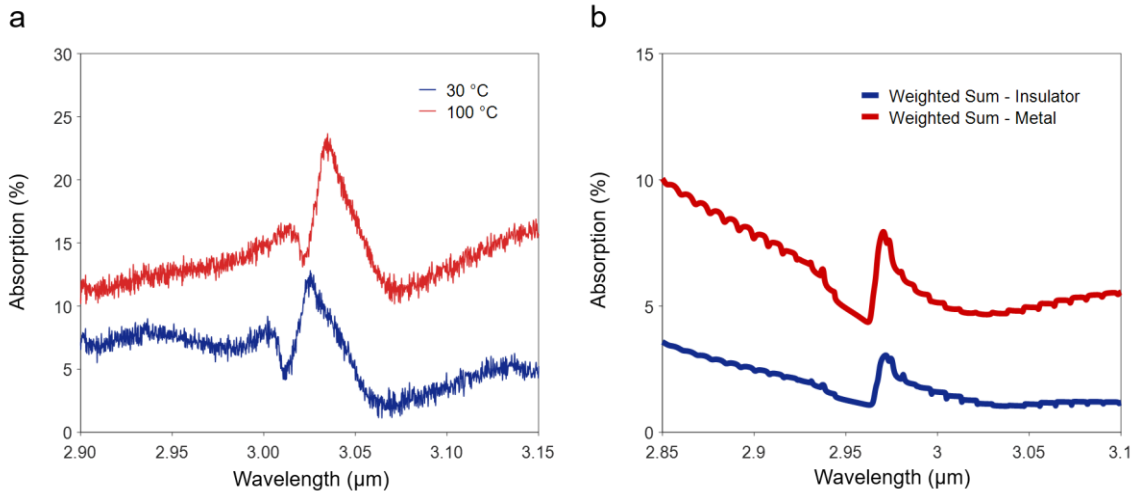

Figure 4.10. Effect of the broad angular distribution. (a) Experimental results of absorption peak for the second-order mode and (b) simulation results demonstrating the effect of broad angular distribution of incident light. We adopted the weighted sum of absorption spectra at different incident angles (Figure 4.9) to account for the high-numerical-aperture objective lens of the measurement system.

To investigate the effect of the broad angular distribution, we superposed the spectra using a weighted sum equation [19] by assuming a Gaussian profile of the incident beam within the incident angle. Figure 4.10 shows the superposed spectra of the insulating (solid blue line) and metallic (solid red line) VO_2 phases. The superposed spectra differ from those of the normally incident light. They show broader linewidth and reduced absorption at the GMR locations, which indicates a similar trend to that observed experimentally (Figure 4.7). Compared to the modes, the line profile of the fundamental mode is unclear, as it is much broader. The main reason for this is that the resonance overlaps with a broad Fabry-Perot-like peak in its proximity, in addition to the effect of the angular distribution of the broad light incidence. Furthermore, the materials grown by PECVD (SiO_2 and Si) induce undesirable absorptions from the phonon bands to degrade the Q-factor of the resonance [20].

Additionally, some inhomogeneity of the fabricated structure could have induced discrepancies between the simulation and experimental results. For example, variations in the grating period and slab thickness resulted in large variations in resonance locations as they changed the phase-matching condition. Finally, undesirable absorptions from dielectric layers grown by PECVD, such as the Si slab and SiO_2 gap, degraded the quality factor of the resonant structure. The overall absorption obtained experimentally exceeded that obtained through the simulation. This is mainly attributed to the normalization errors obtained for the experimental results, as the Au reflector used for the background measurements was not a perfect reflector.

4.6 References

[1] Landy, N. I.; Sajuyigbe, S.; Mock, J. J.; Smith, D. R.; Padilla, W. J. Perfect Metamaterial Absorber. *Phys. Rev. Lett.* 2008, 100, 207402.

[2] Liu, N.; Mesch, M.; Weiss, T.; Hentschel, M.; Giessen, H. Infrared Perfect Absorber and its Application as Plasmonic Sensor. *Nano Lett.* 2010, 10, 2342–2348.

[3] Kats, M. A.; Capasso, F. Optical Absorbers based on Strong Interference in Ultra-Thin Films. *Laser Photon. Rev.* 2016, 10, 735–749.

[4] Chan, D. L. C.; Soljačić, M.; Joannopoulos, J. D. Thermal Emission and Design in 2D-Periodic Metallic Photonic Crystal Slabs. *Opt. Express* 2006, 14, 8785–8796.

[5] Ghebrebrhan, M.; Bermel, P.; Yeng, Y. X.; Celanovic, I.; Soljačić, M.; Joannopoulos, J. D. Tailoring Thermal Emission via Q Matching of Photonic Crystal Resonances. *Phys. Rev. A* 2011, 83, 033810.

[6] Liu, X.; Tyler, T.; Starr, T.; Starr, A. F.; Jokerst, N. M.; Padilla, W. J. Taming the Blackbody with Infrared Metamaterials as Selective Thermal Emitters. *Phys. Rev. Lett.* 2011, 107, 045901.

[7] Constantini, D.; Lefebvre, A.; Coutrot, A.-L.; Moldovan-Doyen, I.; Hugonin, J.-P.; Boutami, S.; Marquier, F.; Benisty, H.; Greffet, J.-J. Plasmonic Metasurface for Directional and Frequency-Selective Thermal Emission. *Phys. Rev. Appl.* 2015, 4, 014023.

[8] Liu, X.; Padilla, W. J. Dynamic Manipulation of Infrared Radiation with MEMS Metamaterials. *Adv. Opt. Mater.* 2013, 1, 559–562.

[9] Vassant, S.; Doyen, I. M.; Marquier, F.; Pardo, F.; Gennser, U.; Cavanna, A.; Pelouard, J. L.; Greffet, J. J. Electrical Modulation of Emissivity. *Appl. Phys. Lett.* 2013, 102, 081125.

[10] Vassant, S.; Archambault, A.; Marquier, F.; Pardo, F.; Gennser, U.; Cavanna, A.; Pelouard, J. L.; Greffet, J. J. Epsilon-Near-Zero Mode for Active Optoelectronic Devices. *Phys. Rev. Lett.* 2012, 109, 237401.

[11] Brar, V. W.; Sherrott, M. C.; Jang, M. S.; Kim, S.; Kim, L.; Choi, M.; Sweatlock, L. A.; Atwater, H. A. Electronic Modulation of Infrared Radiation in Graphene Plasmonic Resonators. *Nat. Commun.* 2015, 6, 7032.

[12] Inoue, T.; Zoysa, M. De; Asano, T.; Noda, S. Realization of Dynamic Thermal Emission Control. *Nat. Mater.* 2014, 13, 928–931.

[13] Inoue, T.; Zoysa, M. De; Asano, T.; Noda, S. Electrical Tuning of Emissivity and Linewidth of Thermal Emission Spectra. *Phys. Rev. B* 2015, 91, 235316.

[14] Liu, R.; Zhong, Y.; Yu, L.; Kim, H.; Law, S.; Zuo, J.-M.; Wasserman, D. Mid-Infrared Emission from In(Ga)Sb Layers on InAs(Sb). *Opt. Express* 2014, 22, 24466–24477.

[15] Wang, S. S.; Magnusson, R. Theory and Applications of Guided-Mode Resonance Filters. *Appl. Opt.* 1993, 32, 2606–2613.

[16] Rosenblatt, D.; Sharon, A.; Friesem, A. A. Resonant Grating Waveguide Structures. *IEEE J. Quantum Electron.* 1997, 33, 2038–2059.

[17] Wang, S. S.; Magnusson, R. Resonant Grating Waveguide Structures. *Appl. Opt.* 1993, 32, 2606–2613.

[18] Shin, D. H.; Tibuleac, S.; Maldonado, T. A.; Magnusson, R. Thin-Film Optical Filters with Diffractive Elements and Waveguides. *Opt. Eng.* 1998, 37, 2634–2646.

[19] Kim, S.; Jang, M. S.; Brar, V. W.; Tolstova, Y.; Mauser, K. W.; Atwater, H. A. Electronically Tunable Extraordinary Optical Transmission in Graphene Plasmonic Ribbons Coupled to Subwavelength Metallic Slit Arrays. *Nat. Commun.* 2016, 7, 12323.

[20] Han, S. M.; Aydil, E. S. Detection of Combinative Infrared Absorption Bands in Thin Silicon Dioxide Films. *Appl. Phys. Lett.* 1997, 70, 3269–3271.

Chapter 5

NANOSCALE POSITION AND ORIENTATION MEASUREMENT OF QUANTUM EMITTERS USING VANADIUM DIOXIDE

5.1 Introduction

Over the past few decades, point defects [1] that introduce electronic states with optical transitions, also known as color centers, have garnered great interest owing to their quantum photonics applications, such as quantum computation and quantum information [2, 3], quantum cryptography [4], and quantum sensing [5]. Wide-bandgap materials, such as diamond [6], silicon carbide [7], gallium nitride [8], and zinc oxide [9], offer promising platforms for hosting quantum emitters with emission in the visible to near-infrared spectrum. However, these materials suffer from one or more intrinsic challenges, such as the requirement of cryogenic temperatures, decoherence of emitted photons, optical coupling losses, and challenges associated with chip-based photonic integration. These problems have driven researchers to seek new candidate materials with fewer disadvantages [10, 11].

Recent discoveries of quantum light emission from 2D van der Waals (vdW) layered materials [12-17] have introduced promising candidates for single photon emitters (SPEs). In contrast to bulk materials, vdW materials offer easier integration with photonic structures and minimal loss due to the refractive index mismatch [18, 19]. Among the several candidate vdW host materials, *h*BN has received particular attention due to its ability to offer a bright source of quantum light at room temperature. The quantum emitters

in *h*BN have shown high (>80%) Debye–Waller factor [17], a brightness comparable to that of the brightest SPEs [10, 19], polarized emission [17, 20], giant stark shift [21-23], magnetic-field-dependent quantum emission [24, 25], correlated cathodoluminescence and photoluminescence (PL) emission [26], and near transform-limited optical linewidth [27], all of which have been reported at room temperature. To date, the atomic structure of *h*BN quantum emitters remains unclear; the most common approach to deduce the atomic structure of these emitters has been to compare the energy of the zero-phonon line (ZPL) and phonon-assisted emission to the first-principles calculations [28]. However, this approach cannot narrow down the pool of possible candidates. Accurate information regarding the 3D orientation of the emitting dipole can provide invaluable insight into the underlying symmetry properties of the defect center, which can complement the aforementioned approach and help in identifying the atomic origin of emitters.

Quantum emitters in multilayered flakes, in contrast to mono- and few-layered flakes, exhibit superior emission characteristics, such as higher saturation counts and spectral stability, due to the reduced environmental screening effects [29]. However, an efficient coupling of these quantum emitters with nanophotonic structures requires precise information about their axial position and 3D dipole orientation. Determining both, the 3D dipole orientation and axial position of a quantum emitter in any multilayered *h*BN, poses a coupled problem because the polarization characteristics of the detected photons are strongly influenced by either dipole orientation or axial position.

Here, we demonstrate the nanometer-scale axial location of *h*BN quantum emitters in a multilayered flake by leveraging the highly sensitive, distance-dependent modulation of the spontaneous emission lifetime of these quantum emitters when they are located near a tunable PCM (i.e., VO_2). Specifically, we modified the local density of optical states (LDOS) by inducing an IMT in VO_2, which in turn modulated the emission rate of quantum emitters near the *h*BN/VO_2 interface. This method, along with the use of emission

polarimetry to determine the 3D orientation of the quantum emitter, yielded comprehensive information about emitters' axial position and orientation, which can be used to distinguish possible candidates based on the atomic structure of the emitter.

5.2 Vanadium Dioxide Film Growth and Characterization

A 40-nm-thick VO_2 film was formed on a clean c-plane single-side-polished sapphire substrate by pulsed laser deposition. A high-power pulsed laser beam vaporized a vanadium target and deposited a thin film on the sapphire substrate in the presence of 5-mTorr oxygen gas at an elevated temperature (650 °C). First, the surface of the VO_2 film grown on the sapphire substrate was conformed to be uniform and continuous with root-mean-square roughness of approximately 1.5 nm, as measured by AFM (Figure 5.1). The measurement results showed the morphology of the VO_2 film, comprising smooth and continuous small grains.

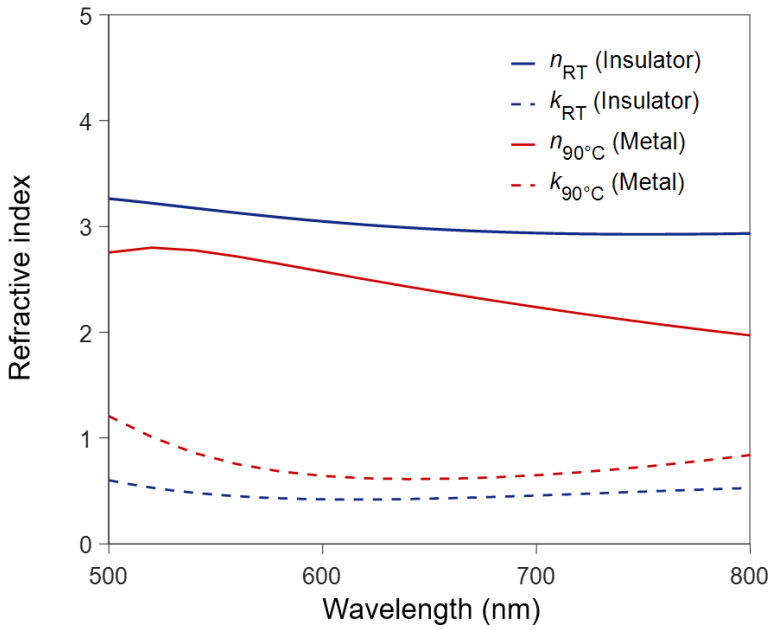

Figure 5.1. Complex refractive index of VO_2 in insulating and metallic phases. Extracted value of real (n) and imaginary (k) parts of the complex refractive index of 40-nm-thick layer of VO_2 deposited on a sapphire crystal at 30 °C (blue) and 100 °C (red) from our ellipsometry data.

We used the Bruggeman effective medium approximation to estimate the intermediate optical constants as a function of the volume fraction of the metallic-phase VO_2 layer. The legend R(0.00) denotes a purely insulating-phase VO_2, whereas R(1.00) represents a purely metallic-phase VO_2. The estimated optical constants were used in full-wave simulations to monitor the reflectance values at normal incidence. The full-wave simulation results were consistent with the measured spectra, which validate the characterized refractive index and thickness of the VO_2 film.

To characterize the optical properties of the VO_2 film grown on the sapphire substrate, we measured the reflectance spectra in the visible range. The temperature-dependent reflectance curves were measured using a microscope spectrometer with an external heating stage. Figure 5.2 shows the temperature-dependent reflectance modulation of the 40-nm-thick VO_2 film for the heating cycle in the 30–100°C range. When the substrate temperature was gradually varied, we observed a gradual change in reflectance as a result of the IMT. The temperature-dependent curves indicated a gradual decrease in reflectance as the VO_2 film exhibited a lower index and a lossier metallic state.

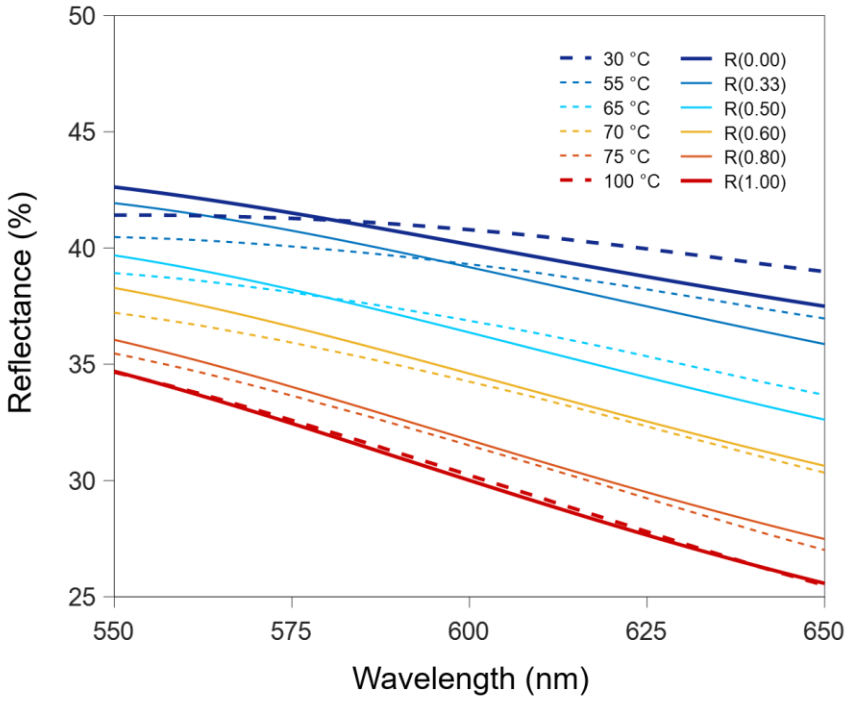

Figure 5.2. Temperature-dependent reflectance spectra of a VO_2 film during the heating cycle (dotted lines) and simulated reflectance curves of the film using the Bruggeman effective medium theory (solid lines). We observe gradual reflectance variations upon phase transition in VO_2, where the volume fraction of metallic-phase VO_2 gradually evolves within the insulating-phase VO_2 host.

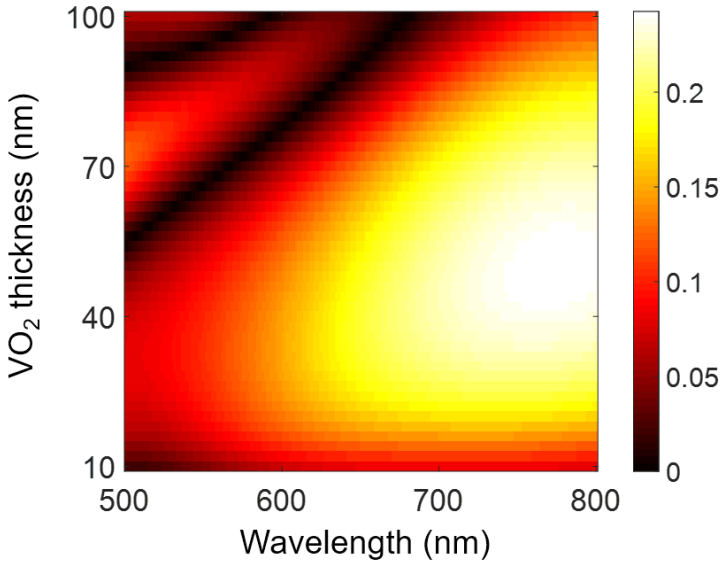

Figure 5.3. Optimization of VO_2 thickness. The figure of merit (FOM) map of the VO_2 film on the sapphire substrate is obtained using full-wave simulations. The FOM map indicates the reflectance contrasts between the insulating and metallic phases of VO_2. The results indicate the largest optical contrasts at the zero-phonon lines when the VO_2 thickness is approximately 40 nm.

We performed full-wave electromagnetic simulations using an FDTD method to estimate the optimal thickness of the VO_2 film in order to obtain the largest optical contrast in the PL wavelength range. We used a commercial Lumerical FDTD software package to obtain the reflectance spectra of the VO_2 film on the sapphire substrate. The reflectance maps of the thin-film structure were monitored by varying the thickness of the VO_2 film for both insulating and metallic phases. Finally, the thickness of the VO_2 film was optimized based on the FOM equation shown below. Figure 5.3 represents the simulated FOM map, where an approximately 40-nm-thick VO_2 film shows the largest reflectance contrast at the ZPLs of our exfoliated *h*BN flake. Based on this analysis, we grew 40-nm-thick VO_2 films on sapphire substrates.

$$FOM = \frac{|R_{Metallic} - R_{Insulating}|}{R_{Metallic} + R_{Insulating}}$$

Here, $R_{Metallic}$: metallic-phase reflectance and $R_{Insulating}$: insulating-phase reflectance.

5.3 Analytical Calculation and Numerical Analysis

5.3.1 Photoluminescence quantum yield calculation of single *h*BN quantum emitter

We modeled a single *h*BN quantum emitter as a three-level system that comprises a ground state $|b\rangle$, an excited state $|a\rangle$, and a metastable state $|c\rangle$, as shown in Figure 5.4. The emission characteristics of this quantum emitter can be described by the rate equations for the population of the three levels [38].

$$\dot{\varrho}_{aa} = R\varrho_{bb} - (\gamma_b + \gamma_a)\varrho_{aa} \tag{5.1}$$

$$\dot{\varrho}_{cc} = \gamma_a\varrho_{aa} - \gamma_c\varrho_{cc} \tag{5.2}$$

Here, R is the rate of excitation and γ_i (with I = a, b, c) is the decay rate of the population (radiative and nonradiative combined).

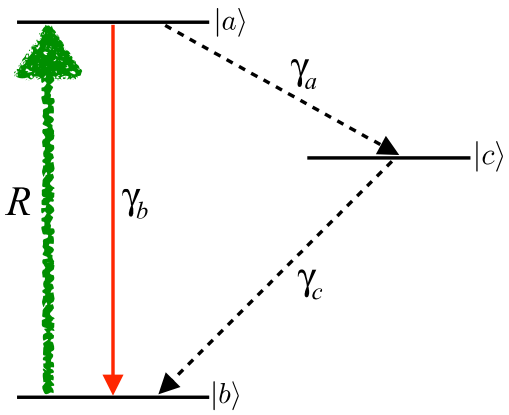

Figure 5.4. Three-level system with corresponding decay and excitation rates.

These equations are supplemented with the population conservation equation $\varrho_{aa} + \varrho_{bb} + \varrho_{cc} = 1$. Using the rate equations, the analytical expression for the normalized "ideal" second-order autocorrelation function $g^2(\tau)$ can be derived as

$$g^2(\tau) = 1 - \left[(1+\zeta)e^{-\lambda_1|t|} - \zeta e^{-\lambda_2|t|}\right] \tag{5.3}$$

where the coefficients are given in the limit ($\gamma_b \gg \gamma_a, \gamma_c$)

$$\gamma_1 = R + \gamma_b \tag{5.4}$$

$$\gamma_2 = \gamma_c + \frac{R\gamma_a}{(R+\gamma_b)} \tag{5.5}$$

$$\zeta = \frac{R\gamma_a}{[\gamma_c(R+\gamma_b)]} \tag{5.6}$$

However, in the presence of background noise, such as a laser scatter or diffused PL, Eq. (5.3) takes the following modified form [20]:

$$g^2(\tau) = 1 - \rho^2\left[(1+\zeta)e^{-\gamma_1|\tau|} - \zeta e^{-\gamma_2|\tau|}\right] \tag{5.7}$$

where ρ quantifies the background noise and $g^2(0) = 1 - \rho^2$. The decay rate of the excited state $|a\rangle$ is $\gamma_t = \gamma_a + \gamma_b \approx \gamma_b$ as the transition rate to the metastable state $|c\rangle$ is orders of magnitude smaller than the decay rate γ_b. From Equation (5.4), we can obtain the decay rate of the quantum emitter by using the pump-power-dependent decay rate γ_1 as $\gamma = \gamma_1 - R$. In our experiment, the focal spot was near the diffraction limit ($\sim 0.5\ \mu m$), and the average pump power was maintained constant at $P_{avg} = 50\ \mu W$ for all measurements.

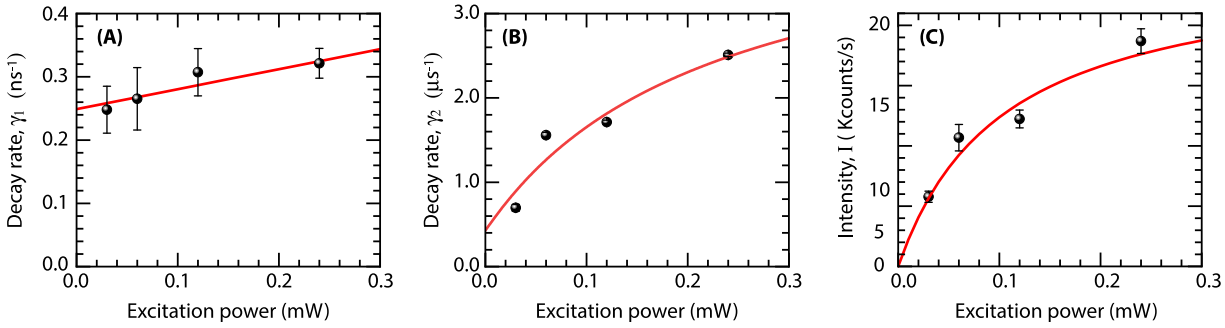

Figure 5.5. Plot of the decay rates $\boldsymbol{\gamma_{1,2}}$ as a function of excitation power at the emitter location. We fit the experimental data shown in (A) and (B) with Eqs. (5.4) and (5.5), respectively. (C) Plot of intensity as a function of excitation power to determine the saturation count rate (I_{sat}) and saturation power (P_{sat}).

The spontaneous decay γ and absorption cross-section σ can be estimated by measuring the pump-power-dependent decay rate γ_1. Figure 5.5a shows the evolution of γ_1 as a function of excitation power at the location of the emitter after accounting for Fresnel reflections from all interfaces. According to the results of our full wave-simulation, for emitter A ($\lambda = 600\ nm$), the excitation power drops to $\tilde{P}_{avg} \cong 0.6\ P_{avg}$. From the linear fit, we obtained the spontaneous decay $\gamma = 249$ MHz by extrapolating the linear fit to zero excitation power. At excitation power $\tilde{P}_{avg} = 30\ \mu W$, the absorption rate $R = 9.5$ MHz. Thus, in our experiment, the contribution of the excitation rate R was negligible compared to that of the spontaneous decay rate (i.e., $\gamma \cong \gamma_1$). The absorption rate is given by $R = \sigma\ I/h\nu$ [39], where σ indicates the absorption cross-section, I indicates the excitation intensity, and ν indicates the excitation frequency. Using the absorption rate $R = 9.5$ MHz at excitation power $\tilde{P}_{avg} = 30\ \mu W$ and a near-diffraction-limited focal spot, we estimated the absorption cross-section $\sigma \cong 9.28 \text{ x } 10^{-16}\ cm^2$. Similar absorption cross-sections for *h*BN emitters have been reported previously [46]. Next, we estimated the intersystem crossing rates by fitting γ_2 with Equation (5.5). Here, we treated γ_a as constant [39] and γ_c

as the excitation power-dependent rate of the form $\gamma_c = \gamma_c^0 + \frac{uP}{P+v}$. From our fitting, we obtained $\gamma_a = 5.84$ MHz, $\gamma_c^0 = 0.40$ MHz, u = 0.89 MHz, and v = 0.05 mW.

Internal quantum yield is an important parameter for a quantum emitter and can be estimated from the value of the rate coefficients and the maximum single photon rates (i.e., the saturation count rate I_∞) as [39]:

$$I_\infty = \eta_c \eta_q \frac{\gamma_b}{1+\gamma_a(\gamma_c^0+u)^{-1}} \tag{5.8}$$

Here, η_c is the collection efficiency of the experimental setup; η_q is the quantum efficiency; and $\gamma_b, \gamma_a, \gamma_c^0, u$ are the rate coefficients that can be obtained using the power-dependent deshelving model. We fitted the power-dependent PL intensity with the function $I = I_{sat}\left(\frac{P}{P+P_{sat}}\right)$ and obtained $I_{sat} = 0.025$ MHz and $P_{sat} = 104\,\mu W$. From the rate coefficients, we obtained $\eta_c\eta_q = 5.63 \times 10^{-4}$. Taking into account the collection, transmission, and coupling efficiencies of the optical element of the experimental setup, the collection efficiency $\eta_c = 8.87 \times 10^{-4}$, which yielded $\eta_q = 0.634$. The quantum efficiency η_q is contributed from the internal quantum yield, radiative Purcell enhancement, and the nonradiative loss resulting from the ohmic loss in VO_2. Using simple algebra, we obtain

$$\frac{1}{\eta_q} = \frac{1}{\eta_l} + \frac{1}{\eta_e}\left(\frac{1}{\eta_i} - 1\right). \tag{5.9}$$

Here, η_l indicates the rate of energy loss in VO_2, η_i is the internal quantum yield of the *h*BN emitter, and η_e is the radiative Purcell enhancement with respect to the homogenous medium. Our full-wave simulation yielded $\eta_l = 0.76$ and $\eta_e = 0.324$, which yielded $\eta_i = 0.793$.

5.3.2 LDOS manipulation using VO_2

Figure 5.6 shows the individual contributions of the radiative and nonradiative channels to the decay rates $\gamma_{Insulating}$ (Figure 5.6a,b) and $\gamma_{Metallic}$ (Figure 5.6c,d) for both parallel and perpendicular orientations as a function of distance (*d*) from the *h*BN/VO_2 interface. The nonradiative decay rate of the emitter corresponds to the emission of a photon that is absorbed in the lossy material VO_2. For numerical simulation, we considered an *h*BN quantum emitter with a ZPL wavelength of approximately 600 nm and a photoluminescence quantum yield (PLQY) of 0.79. Figure 5.6 illustrates that, at distances ranging from approximately 0 to 15 nm, the decay rate γ is dominated by the nonradiative channel. Thus, the emitters located within this distance range are "hidden" owing to a lack of light emission available for the collection objective lens. However, the radiation contribution to the total decay rate is stronger for the vertical dipole compared to the horizontal dipole within the first approximately 50 nm with both states of VO_2. Thus, emitters found near the *h*BN/VO_2 interface exhibit a higher probability of dipole moment oriented along the vertical direction.

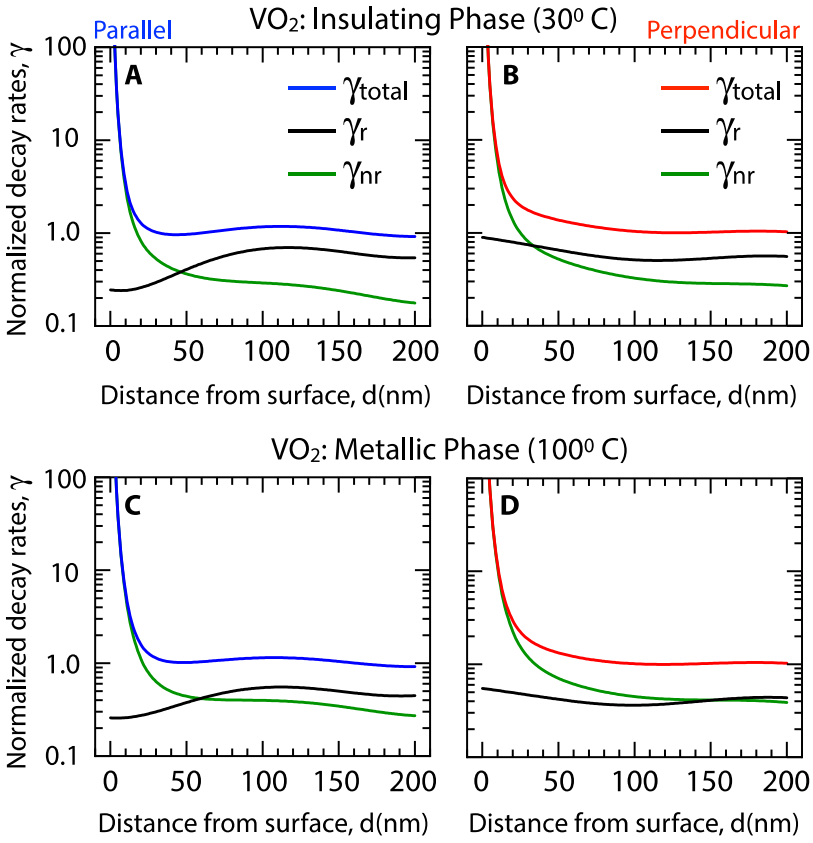

Figure 5.6. Radiative and nonradiative decay rates. Total (γ_{total}/γ_0), radiative (γ_r/γ_0), and nonradiative (γ_{nr}/γ_0) rates of spontaneous emission of a quantum emitter as a function of distance from the VO_2 surface for two dipole orientations (i.e., parallel ($\theta = 90°$) and perpendicular ($\theta = 0°$) to the surface). For the numerical simulation, we consider the emission wavelength λ_0 = 600 nm and quantum yield (QY) = 0.79 corresponding to the emitter "A." (A, B) Insulating-phase VO_2 and (C, D) metallic-phase VO_2. Free-space decay rate $\gamma_0 = n\omega_0^3|\varrho|^2/3\pi\varepsilon_0\hbar c^3$, where c is the speed of light, n is the refractive index of *h*BN, ω_0 is the atomic transition frequency, $\hbar$ is the reduced Planck's constant, and ϱ is the amplitude of the dipole moment vector. The refractive indices of the upper medium, *h*BN, and sapphire are set to 1, 1.82, and 1.77, respectively. The refractive index of VO_2 at 600 nm is set to 3.05 + 0.42i (insulating phase) and 2.57 + 0.64i (metallic phase) from our ellipsometry data.

5.4 Experimental Measurement

5.4.1 Experimental configuration

The experimental configuration is shown in Figure 5.7a, where a quantum emitter is located at a distance *d*, within the thickness of an *h*BN flake, from the surface of a substrate that comprises a thin layer of VO_2 formed on a sapphire substrate. PL excitation and detection were performed with optical pumping of quantum emitters by laser excitation from the top. The decay rate of the excited quantum emitter depends on its interaction with the optical environment [30]. By optical environment, we mean the substrate beneath and the air above the *h*BN flake. We modeled this interaction by treating the quantum emitter as an oscillating-point dipole source oriented along the (θ, φ) direction. For an emitter in an unbounded, homogeneous, and lossless medium with refractive index *n*, the spontaneous decay rate is enhanced by a factor *n* compared to the free space. This result also holds for bounded geometry, as long as the emitter is placed at a distance $d \gg \lambda$ from any interface. When $d \ll \lambda$, the decay rate strongly depends on *d*, dipole orientation (θ, φ), and refractive index contrast across the interface [31-33]. In this study, we manipulated the optical environment of a quantum emitter located near the *h*BN/VO_2 interface by using VO_2, whose complex refractive index exhibits a sharp change when VO_2 is thermally switched from the insulating to metallic state at a near-room temperature $T_c \approx 340$ K [34].

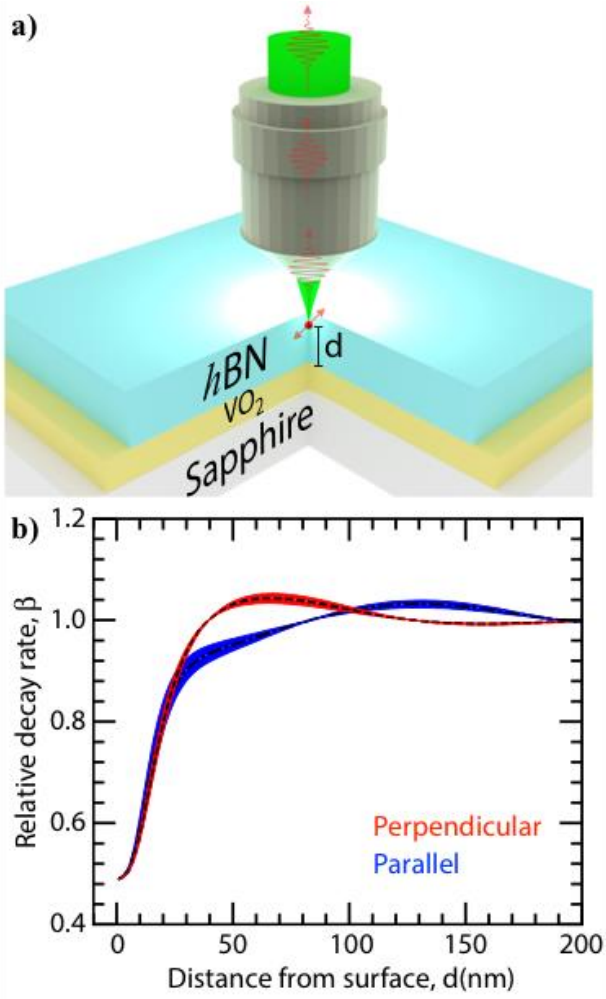

Figure 5.7. Experimental schematic and distance-dependent modulation of relative decay rates. (a) Schematic of a quantum emitter in an atomically thin crystal of hexagonal boron nitride (*h*BN) located within the thickness of a flake on a substrate that comprises a thin layer of VO_2 deposited on a sapphire crystal. (b) Relative decay rate $\beta = \gamma_{Insulating}/\gamma_{Metallic}$ as a function of distance d of a quantum emitter from the surface of the VO_2 layer when switched from insulating to metallic state. The blue and red curves indicate quantum emitters oriented parallel and perpendicular to the surface, respectively, and the shaded regions correspond to the typical quantum yield (QY) range of 0.6–1.0 of *h*BN quantum emitters with the zero-phonon line around 600 nm (46). For numerical simulation, we consider the emission wavelength of 600 nm for the quantum emitter corresponding to the emitter "A" (Figure 5.8e). The dashed line within the shaded region corresponds to QY = 0.79, as estimated from our experimental data. The refractive indices of the upper medium, *h*BN, and sapphire are set to 1, 1.82, and 1.77, respectively. The refractive indices of VO_2 at 600 nm are set to 3.05 + 0.42i (insulating state) and 2.57 + 0.64i (metallic state) from our ellipsometry data.

Figure 5.7b shows the calculated relative decay rate $\beta = \gamma_{Insulating}/\gamma_{Metallic}$ of an emitter as a function of distance *d* when the emitter is oriented perpendicular ($\theta = 0°$) and parallel ($\theta = 90°$) to the *h*BN/VO_2 interface. Here, $\gamma_{Insulating}$ and $\gamma_{Metallic}$ indicate the total (radiative and nonradiative) decay rate of the emitter when VO_2 is in insulating (30 ℃) and metallic (100 ℃) states. In these simulations, we considered a flake thickness of 310 nm and emission wavelength of 600 nm, corresponding to those of the quantum emitters in our experiment, as shown in Figure 5.10a,b. The refractive indices of the upper medium, *h*BN, and sapphire were set to 1, 1.82 [35], and 1.77, respectively. The complex refractive index of VO_2 at 600 nm was extracted from our ellipsometry data and set as 3.05 + 0.42i and 2.57 + 0.64i for VO_2 in the insulating and metallic states, respectively. The thickness of the VO_2 layer was 40 nm. In general, the PLQY of *h*BN quantum emitters varies in the range 0.6–1.0 [10, 19], and a recent experiment has shown average PLQY in the range 0.6–0.8 for quantum emitters with ZPL around 600 nm [36]. The shaded area in Figure 5.7b corresponds to this PLQY range. The dashed line within the shaded region corresponds to PLQY = 0.79 estimated from our experimental data. The relative modulation of the decay rates for both orientations is clearly evident within the first approximately 50 nm, which quickly fades away at distances of approximately 100 nm and above. We use this highly sensitive distance-dependent decay rate of quantum emitters near the *h*BN/VO_2 interface to localize their position along the axial direction.

5.4.2 Experimental setup for optical characterization

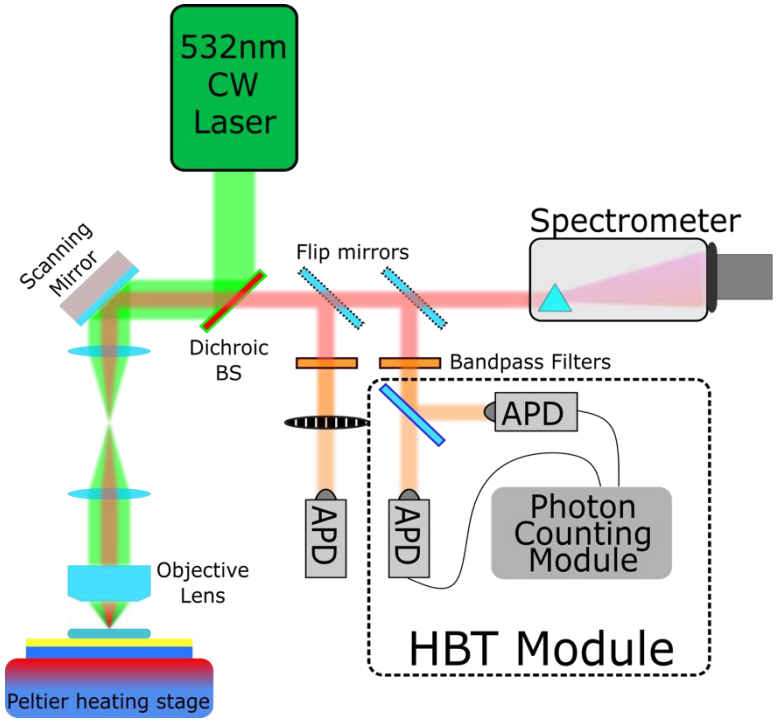

Figure 5.8. Experimental setup. Schematic of the homebuilt confocal microscope used to characterize hexagonal boron nitride quantum emitters and perform correlation measurements.

The optical characterization of the samples was performed using a home-built confocal microscope capable of optical spectroscopy in the visible range and intensity auto-correlation measurement ($g_2(\tau)$) in a Hanbury–Brown–Twiss configuration using a 50–50 beam splitter and two avalanche photodiodes. We used a fast-scanning mirror and a 4*f* telecentric configuration to perform PL mapping. The microscope used a 532-nm continuous-wave laser to pump emitters in *h*BN, a 100× objective to focus the beam on the sample, and 50-μW laser power (before objective) for all emitters. A quarter-wave plate was placed in the beam path at 45° orientation with respect to the linear polarization of the

laser in order to produce circularly polarized light. We pumped with circularly polarized light to excite all emitters irrespective of their in-plane dipole orientation. A tunable bandpass filter was used to only pass ZPL on the emitter into the HBT setup to reduce the background noise. A schematic of our optical characterization setup is shown in Figure 5.8. Annealing in an inert environment is routinely used to create or activate quantum emitters in diamond and *h*BN. For the *h*BN samples used in this study, we annealed a bulk crystal of *h*BN at 950 ℃ in 1-bar-pressure argon gas for 30 min before exfoliation. We mounted our sample comprising the *h*BN/VO_2/sapphire interface on a Peltier heating stage.

5.4.3 Optical characterization of *h*BN quantum emitters

Figure 5.9a shows the optical microscope image of a thin *h*BN flake on a VO_2/sapphire substrate. This sample was prepared by mechanical exfoliation of high-purity *h*BN single crystals and transferred onto a 40-nm-thick VO_2 film deposited on a 500-μm-thick sapphire substrate by pulsed laser deposition. To determine the thickness of this flake at each position, we used AFM. Figure 5.9b shows an AFM image of the *h*BN flake shown in Figure 5.9a. The red dots in Figures 5.9a,b indicate the locations of the quantum emitters "A" and "B" with emission wavelengths of 600 and 620 nm, respectively. Figure 5.9c shows the AFM height profile across the lines (S-E) indicated in Figure 5.9b, where the flake thickness varies from 230 to 420 nm. At the locations of emitters "A" and "B," the flake heights were 310 and 340 nm, respectively.

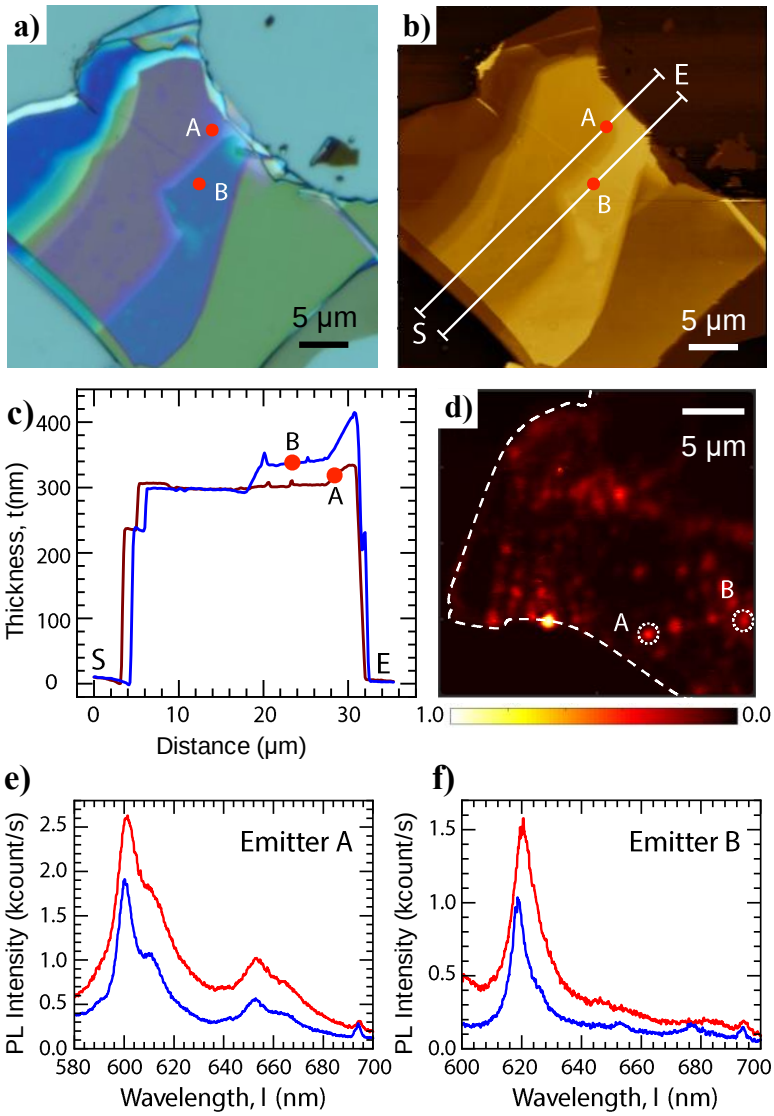

Figure 5.9. Characterization of the exfoliated flake and spectra of hexagonal boron nitride (*h*BN) quantum emitters. (a) Optical image of the mechanically exfoliated *h*BN flake on VO_2/sapphire substrate. (b) Atomic force microscopy image of the flake shown in (a). The red dots on the traces (S-E) in (b) and (a) indicate the positions of emitters "A" and "B" with emission wavelengths of 600 and 620 nm, respectively. (c) Line profiles along the region indicated by the trace in (b). At the locations of emitters "A" and "B," the flake heights are 310 and 340 nm, respectively. (d) Confocal photoluminescence (PL) map of the *h*BN flake. The positions of two single photon emitters are marked by white circles. The flake edge is marked by a white dashed line. The PL spectra of emitters "A" and "B" shown in (e) and (f), respectively, are obtained with VO_2 in the insulating state (blue) and metallic state (red).

To locate the quantum emitters precisely, we performed confocal PL mapping in a mode in which the sample was scanned point-by-point. Figure 5.9d shows a PL map over an area of 20 × 20 μm^2 on the *h*BN flake. The locations of the quantum emitters "A" and "B" are highlighted by dashed circles. The single-photon emission characteristic of these quantum emitters is evident from their second-order autocorrelation measurements, indicating $g^2(0) < 0.5$ (Figure 5.10a,b). Figure 5.9e,f shows the PL spectra of these quantum emitters obtained for insulating and metallic VO_2. The emission spectra of each quantum emitter comprise a pronounced ZPL accompanied by a weaker phonon-assisted emission. An increase in the PL intensity obtained for metallic VO_2 compared to insulating VO_2 is noticeable for all quantum emitters, which indicates a higher photon emission rate (i.e., decrease in emission lifetime). This enhancement of the emission rate is due to modification in LDOS owing to a change in the complex refractive index of VO_2 when switched from insulating to metallic state. A recent experiment reported that the decay rate of *h*BN quantum emitters remains constant even when they are heated up to 800 K [37], which further corroborates that the enhancement of decay rate is attributed to LDOS modification rather than a thermal effect. The defect-based quantum emitter's dimensions are atomic scale, and thus, the lateral emitter size and location measurement are constrained by the optical diffraction limit.

5.4.4 Single-photon source characterization and axial location

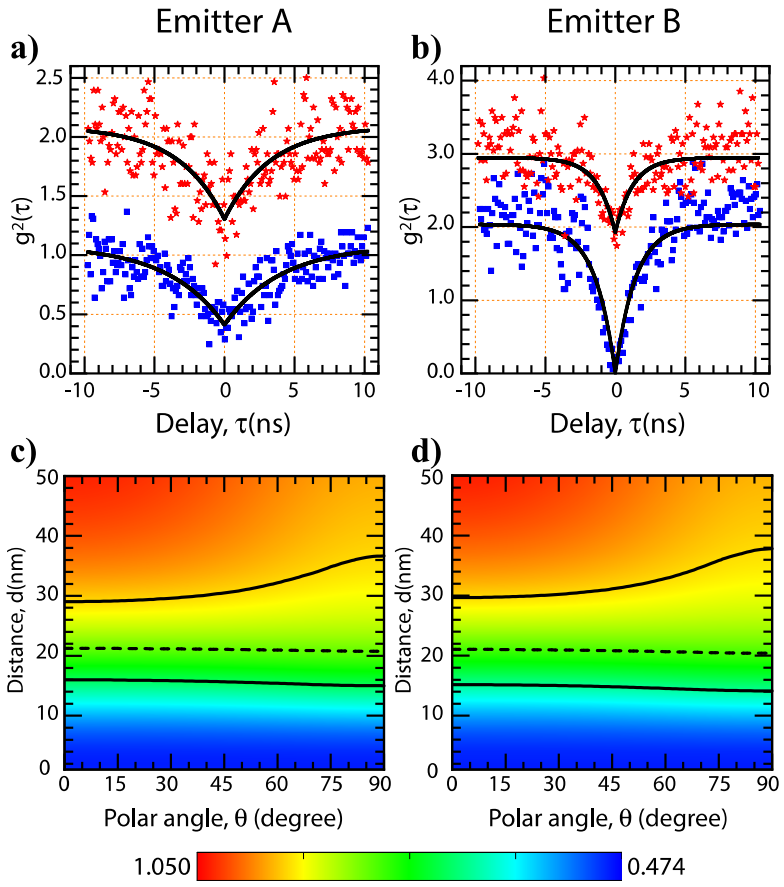

Figure 5.10. Single-photon source characterization and axial location in *h*BN flake. Plot of the second-order photon correlation measurement, $g^2(\tau)$, for emitters "A" and "B" in (a) and (b), respectively. The experimental data, blue squares for insulating VO_2 phase and red stars for metallic VO_2, are fitted using Eq. (5.10) to obtain the decay rates of the emitters. From the fit, we calculate the relative decay rates $\beta = \gamma_{\text{Insulating}}/\gamma_{\text{Metallic}}$ for the two emitters "A" and "B" as 0.818 ± 0.108 and 0.800 ± 0.124, respectively. For clarity, $g^2(\tau)$ data obtained for metallic VO_2 in (a) and (b) are shifted by 1 and 1.5, respectively. Plots of the relative decay rate β as a function of distance (d) from the VO_2 surface and the polar angle (θ) for "A" and "B" are shown in (c) and (d), respectively. The dashed contour lines in (c) and (d) correspond to the experimental values of β obtained from (a) and (b), respectively, whereas the solid lines correspond to the error ($\pm\Delta\beta$) in the ratio.

To investigate the single-photon emission characteristics and decay lifetime of the quantum emitters, we measured their second-order intensity correlation function $g^2(\tau)$ in both insulating and metallic phases of VO_2. To reduce the influence of the background signal and noise, we corrected the raw $g^2_{raw}(\tau)$ using the function $g^2(\tau) = [g^2_{raw}(\tau) - (1-\rho^2)]/\rho^2$, where $\rho = S/(S+B)$ (S and B indicate the signal and background counts, respectively). This background-corrected $g^2(\tau)$ was fitted with the double exponential of the form [20]

$$g^2(\tau) = 1 - \rho^2\left[(1+\zeta)e^{-\gamma_1|\tau|} - \zeta e^{-\gamma_2|\tau|}\right], \tag{5.10}$$

where $\zeta, \rho, \gamma_{1,2}$ are laser power-dependent parameters [20, 35]. Here, γ_1 and γ_2 are the faster and slower decay time constants, respectively, for a three-level system. The second-order intensity correlation functions $g^2(\tau)$ under continuous-wave excitation pumping for "A" and "B" for insulating-phase VO_2 (blue dots) and metallic-phase VO_2 (red dots) are shown in Figure 5.10a and b, respectively. The data for the metallic-phase VO_2 configuration were vertically offset for visual clarity. The equal-time coincidence count $g^2(0)$ for each quantum emitter was less than 0.5, which indicates the presence of a single emitter. All measurements were performed at a constant 50-μW pump laser power, which is several orders of magnitude smaller than the saturation power of ~mW for *h*BN quantum emitters [10, 18, 19]. Given the Fresnel reflections from all interfaces, which were analyzed using full-wave simulations, the excitation power within the flake along the axial direction was position-dependent. From fitting our experimental data of correlation functions $g^2(\tau)$, we extracted the decay constant ($\gamma_{1,2}$), which has contributions from the spontaneous decay rates and the pump rate [43, 44]. The spontaneous decay rates (γ) of "A" and "B" are listed

in Table 5.1. The correlation functions over long-term scales are shown in Figure 5.11. With an excitation power of 50 μW, the pump rates were approximately 25- and 73-fold slower than the spontaneous decay rates for "A" and "B," respectively, and thus, made negligible contributions to the decay constants. Table 5.1 shows that, for all emitters, the decay rates were higher in the presence of a metallic-phase VO_2 as compared to an insulating-phase VO_2 configuration. Thus, "A" and "B" were placed at such distances from the VO_2 surface that their optical environment was modified when VO_2 underwent an IMT.

Emitter	**Decay rate, $\gamma_{\mathbf{Insulating}}$ (MHz)**	**Decay rate, $\gamma_{\mathbf{Metallic}}$ (MHz)**
A	249 ± 15	304 ± 33
B	693 ± 45	865 ± 122
C	268 ± 16	334 ± 18

Table 5.1 Spontaneous emission rates of emitters. Spontaneous decay rates of emitters "A," "B," and "C" near the insulating-phase and metallic-phase VO_2. The decay rates are estimated on the basis of the fitting of $g_2(\tau)$ and subtracting the contribution of pump-dependent excitation rate.

To model the distance dependence of the quantum emitter lifetime on the VO_2 phase, we define the ratio of their decay rates in the insulating and metallic phases as β. Figure 5.10c,d shows a 2D plot of the relative decay rate β as a function of distance d from the *h*BN/VO_2 interface and the polar orientation angle θ of the dipole for each of the quantum emitters "A" and "B," respectively. Each plot has three contour lines: a dashed line for the relative decay rate β and upper and lower solid contour lines for the error in the decay rate ($\pm\ \Delta\beta$). Using the experimental values of γ from Table 5.1, we obtained the values of β for "A" and "B" as 0.818 ± 0.108 and 0.800 ± 0.124, respectively. These simulation and the experimental values of β indicate that the quantum emitters are located within a narrow region at a distance $d \approx 21$ nm from the *h*BN/VO_2 interface. However, the uncertainty in the axial position depends on the emitters' polar angle θ. For emitter "A," the uncertainty (full

width) varies from approximately 13 nm at $\theta = 0°$ to approximately 22 nm at $\theta = 90°$. Similarly, for quantum emitter "B," the uncertainty in their axial location varies from approximately 15 nm at $\theta = 0°$ to approximately 23 nm at $\theta = 90°$.

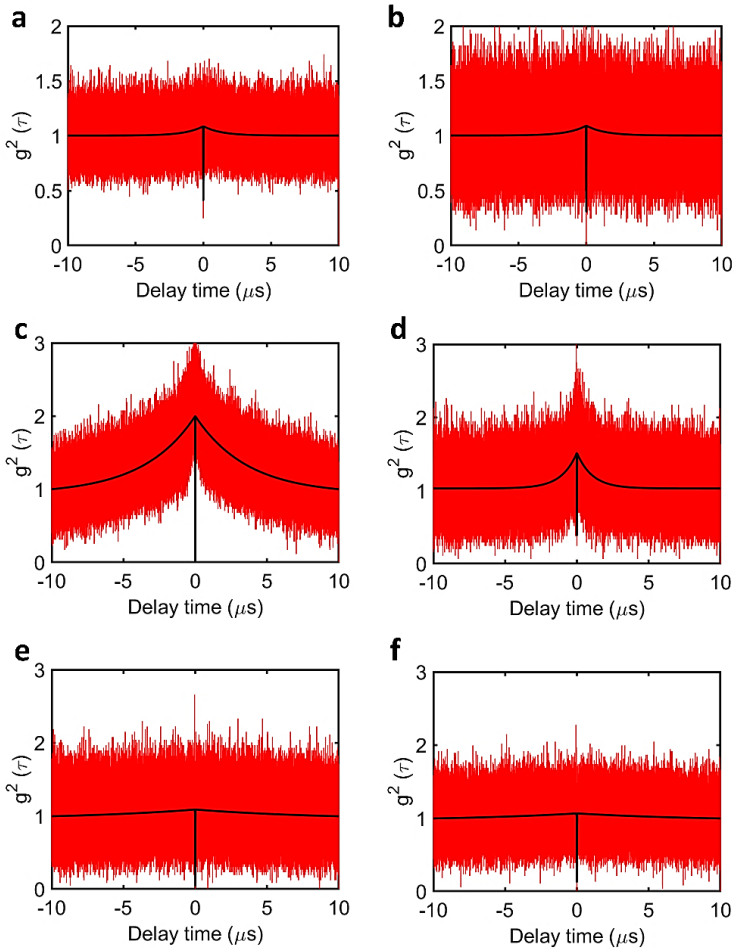

Figure 5.11. Full-scale correlation data for emitters A, B, and C. Plot of correlation measurement for emitter "A" (a, b), emitter "B" (c, d), and emitter "C" (e, f) as a function of delay over the range of microseconds. The data in (a, c, e) and (b, d, f) are at room temperature and 100 °C, respectively.

5.4.5 Nanometric axial location and orientation

Next, we focus on the emission polarimetry of the quantum emitters. Previous studies [45] have shown that the 3D orientation (θ, φ) of a dipole can be directly extracted by analyzing the polarization characteristics of its emitted light. Figure 5.12a and b shows the emission polarization measurements from "A" and "B," respectively. The data are fitted by the function

$$I(\alpha) = I_{min} + (I_{max} - I_{min}) \cos^2(\alpha - \varphi) \tag{4.11}$$

where $I_{min,max}$ and φ are the fitting parameters. From the fit, we obtain the following for emitter "A": $I_{min} = 0.356 \pm 0.013$, $I_{max} = 0.966 \pm 0.024$, and $\varphi = 175.7° \pm 1.0°$. Similarly, for emitter "B", $I_{min} = 0.318 \pm 0.034$, $I_{max} = 0.888 \pm 0.066$, and $\varphi = 109.0° \pm 2.9°$. In emission polarimetry, the polar angle θ can be extracted from the degree of polarization of the emission, as

$$\delta(\theta) = \frac{I_{max} - I_{min}}{I_{max} + I_{min}} \tag{4.12}$$

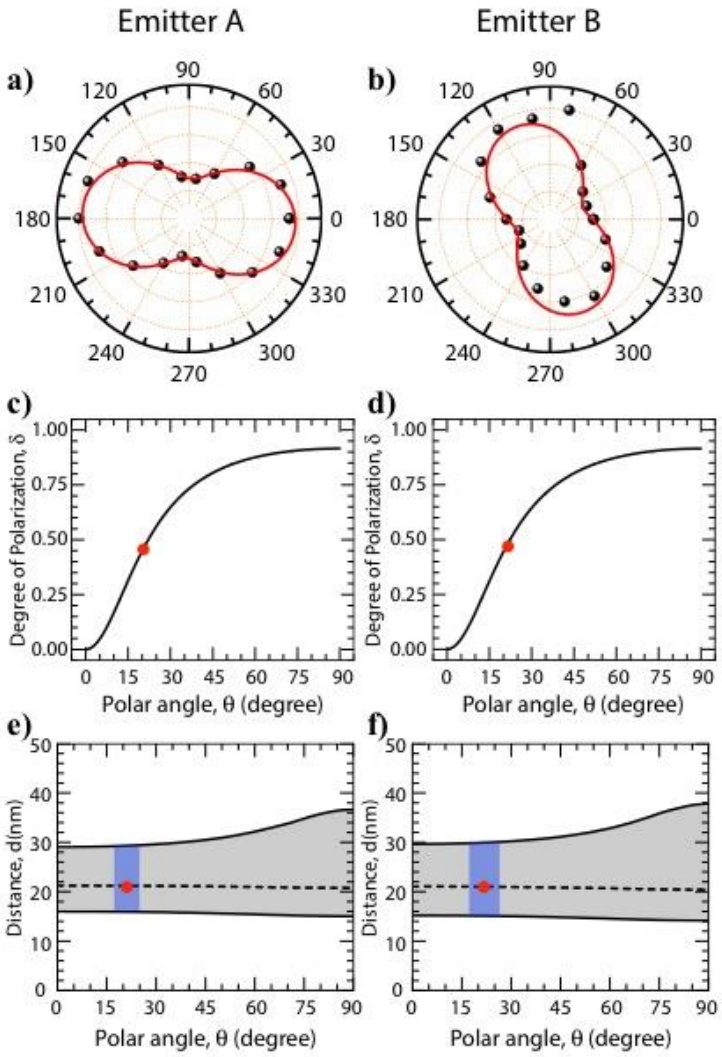

Figure 5.12. Three-dimensional orientation of *h*BN quantum emitters and nanometric axial location. (a, b) Polar plots of the photoluminescence (PL) intensity of the emitters "A" and "B" as a function of the emission polarization analysis angle (α). The PL data (solid spheres) are fitted using Eq. (5.11) to extract the azimuthal angle (φ) of the emitters and the degree of polarization (δ). From the fit, we deduce that, for emitter A, $\varphi = 175.7° \pm 1.0°$ and $\delta = 0.461 \pm 0.023$ and for emitter B, $\varphi = 109.9° \pm 2.9°$ and $\delta = 0.473 \pm 0.070$. (c, d) Calculated value of the degree of polarization (δ) as a function of the polar angle (θ) of the emitters located approximately 21 nm from the VO_2 surface. The red dots in (c) and (d) correspond to the experimental value δ obtained from (a) and (b), respectively. The extracted values of θ for emitters "A" and "B" are $20.5° \pm 3.6°$ and $21.2° \pm 4.5°$, respectively. (e, f) Purple shaded region shows the range of distance (*d*) and polar angle (θ) of "A" and "B" based on our experimental and simulation data.

From the fitting parameters (I_{max}, I_{min}), we obtained $\delta = 0.461 \pm 0.023$ and $\delta = 0.473 \pm 0.070$ for "A" and "B," respectively. Figure 5.12c,d shows the calculated degree of polarization, δ, as a function of the polar orientation angle θ using the experimental values of numerical aperture (0.9) and refractive indices of *h*BN, VO_2 (insulating phase), and sapphire. The distance *d* of the quantum emitters "A" and "B" from the VO_2/sapphire substrate was set to approximately 20 nm. Figure 5.12e,f shows that the variation in the distance *d* is negligible (dashed line). The red dots in Figure 5.12e,f represent the measured value of δ, from which we extracted the polar orientation angle $\theta = 20.5° \pm 3.6°$ and $\theta = 21.2° \pm 4.5°$ for "A" and "B," respectively. In estimating the value of error in θ, we accounted for the error in location *d*, which is shown in Figure 5.12e,f as solid lines. Figure 5.12e represents the nanoscale axial location of emitter A with an uncertainty (full width) of approximately 15 nm, oriented along $(\theta, \varphi) = (20.5° \pm 3.6°, 175.7° \pm 1.0°)$. Similarly, Figure 5.10f represents the nanoscale axial location of emitter B with a full-width uncertainty of approximately 17 nm, oriented along $(\theta, \varphi) = (21.2° \pm 4.5°, 109.9° \pm 2.9°)$. The strong vertical component of the dipole orientation for both emitters found near the *h*BN/VO_2 interface agrees with our simulation results shown in Figure 5.6. The predominant out-of-plane dipole orientation of these emitters is attributable to the out-of-plane atomic structure of the emitter, as discussed in the literature. We believe that the information provided by these measurements is significant for determining the underlying atomic structure of emitters.

5.5 References

[1] Franklin, A. D. In Point Defects in Solids, J. H. Crawford, L. M. Slifkin (Eds.) (Plenum Press, New York, 1972), vol. 1, chap. 1.

[2] Nielsen, M. A.; Chuang, I. L. Quantum Computation and Quantum Information (Cambridge University Press, 2010).

[3] Weber, J. R.; Koehl, J. B. V.; Janotti, A.; Buckley; B. B.; Van de Walle, C. G.; Awschalom, D. D. Quantum Computing with Defects. *Proc. Natl. Acad. Sci. U. S. A* 2010, 107, 8513–8518.

[4] Beveratos, A.; Brouri, R.; Gacoin, T.; Villing, A.; Poizat, J.-P.; Grangier, P. Single Photon Quantum Cryptography. *Phys. Rev. Lett.* 2002, 89, 187901.

[5] Degen, C. L.; Reinhard, F.; Cappellaro, P. Quantum Sensing. *Rev. Mod. Phys.* 2017, 89, 035002.

[6] Doherty, M. W.; Manson, N. B.; Delaney, P.; Jelezko, F.; Wrachtrup, J.; Hollenberg, L. C. L. The Nitrogen-Vacancy Colour Centre in Diamond. *Phys. Rep.* 2013, 528, 1–45.

[7] Awschalom, D. D.; Hanson, R.; Wrachtrup, J.; Zhou, B. B. Quantum Technologies with Optically Interfaced Solid-State Spins. *Nat. Photonics* 2018, 12, 516–527.

[8] Kako, S.; Santori, C.; Hoshino, K.; Götzinger, S.; Yamamoto, Y.; Arakawa, Y. A Gallium Nitride Single-Photon Source Operating at 200 K. *Nat. Mater.* 2016, 5, 887–892.

[9] Morfa, A. J.; Gibson, B. C.; Karg, M.; Karle, T. J.; Greentree, A. D.; Mulvaney, P.; Tomljenovic-Hanic, S. Single-Photon Emission and Quantum Characterization of Zinc Oxide Defects. *Nano Lett.* 2012, 12, 949–954.

[10] Aharonovich, I.; Englund, D.; Toth, M. Solid-State Single-Photon Emitters. *Nat. Photonics* 2016, 10, 631–641.

[11] Atatüre, M.; Englund, D.; Vamivakas, N.; Lee, S.-Y.; Wrachtrup, J. Material Platforms for Spin-Based Photonic Quantum Technologies. *Nat. Rev. Mater.* 2018, 3, 38–51.

[12] Srivastava, A.; Sidler, M.; Allain, A. V.; Lembke, D. S.; Kis, A.; Imamoğlu, A. Optically Active Quantum Dots in Monolayer WSe2. *Nat. Nanotechnol.* 2015, 10, 491–496.

[13] He, Y.-M.; Clark, G.; Schaibley, J. R.; He, Y.; Chen, M.-C.; Wei, Y.-J.; Ding, X.; Zhang, Q.; Yao, W.; Xu, X.; Lu, C.-Y.; Pan, J.-W. Single Quantum Emitters in Monolayer Semiconductors. *Nat. Nanotechnol.* 2015, 10, 497–502.

[14] Koperski, M.; Nogajewski, K.; Arora, A.; Cherkez, V.; Mallet, P.; Veuillen, J.-Y.; Marcus, J.; Kossacki, P.; Potemski, M. Single Photon Emitters in Exfoliated WSe2 Structures. *Nat. Nanotechnol.* 2015, 10, 503–506.

[15] Chakraborty, C.; Kinnischtzke, L.; Goodfellow, K. M.; Beams, R.; Vamivakas, A. N. Voltage-Controlled Quantum Light from an Atomically Thin Semiconductor. *Nat. Nanotechnol.* 2015, 10, 507–511.

[16] Tonndorf, P.; Schmidt, R.; Schneider, R.; Kern, J.; Buscema, M.; Steele, G. A.; Castellanos-Gomez, A.; van der Zant, H. S. J.; De Vasconcellos, S. M.; Bratschitsch, R. Single-Photon Emission from Localized Excitons in an Atomically Thin Semiconductor. *Optica* 2015, 2, 347–352.

[17] Tran, T. T.; Bray, K.; Ford, M. J.; Toth, M.; Aharonovich, I. Quantum Emission from Hexagonal Boron Nitride Monolayers. *Nat. Nanotechnol.* 2016, 11, 37–41.

[18] Aharonovich, I.; Toth, M. Quantum Emitters in Two Dimensions. *Science* 2017, 358, 170–171.

[19] Caldwell, J. D.; Aharonovich, I.; Cassabois, G.; Edgar, J. H.; Gil, B.; Basov, D. N. Photonics with Hexagonal Boron Nitride. *Nat. Rev. Mater.* 2019, 4, 552–567.

[20] Exarhos, A. L.; Hopper, D. A.; Grote, R. R.; Alkauskas, A.; Bassett, L. C. Optical Signatures of Quantum Emitters in Suspended Hexagonal Boron Nitride. *ACS Nano* 2017, 11, 3328–3336.

[21] Noh, G.; Choi, D.; Kim, J.-H.; Im, D.-G.; Kim, Y.-H.; Seo, H.; Lee, J. Stark Tuning of Single-Photon Emitters in Hexagonal Boron Nitride. *Nano Lett.* 2017, 18, 4710–4715.

[22] Xia, Y.; Li, Q.; Kim, J.; Bao, W.; Gong, C.; Yang, S.; Wang, Y.; Zhang, X. Room-Temperature Giant Stark Effect of Single Photon Emitter in van der Waals Material. *Nano Lett.* 2019, 19, 7100–7105.

[23] Nikolay, N.; Mendelson, N.; Sadzak, N.; Böhm, F.; Tran, T. T.; Sontheimer, B.; Aharonovich, I.; Benson, O. Very Large and Reversible Stark-Shift Tuning of Single Emitters in Layered Hexagonal Boron Nitride. *Phys. Rev. Applied* 2019, 11, 041001.

[24] Exarhos, A. L.; Hopper, D. A.; Patel, R. N.; Doherty, M. W.; Bassett, L. C. Magnetic-Field-Dependent Quantum Emission in Hexagonal Boron Nitride at Room Temperature. *Nat Commun.* 2019, 10, 222.

[25] Gottscholl, A.; Kianinia, M.; Soltamov, V.; Orlinskii, S.; Mamin, G.; Bradac, C.; Kasper, C.; Krambrock, K.; Sperlich, A.; Toth, M.; Aharonovich, I.; Dyakonov, V. Initialization and Read-Out of Intrinsic Spin Defects in a Van Der Waals Crystal at Room Temperature. *Nat. Mater.* 2020, 19, 540–545.

[26] Hayee, F.; Yu, L.; Zhang, J. L.; Ciccarino, C. J.; Nguyen, M.; Marshall, A. F.; Aharonovich, I.; Vučković, J.; Narang, P.; Heinz, T. F.; Dionne, J. A. Revealing Multiple Classes of Stable Quantum Emitters in Hexagonal Boron Nitride with Correlated Optical and Electron Microscopy. *Nat. Mater.* 2020, 19, 534–539.

[27] A. Dietrich, M. W. Doherty, I. Aharonovich, A. Kubanek, Solid-State Single Photon Source with Fourier Transform Limited Lines at Room Temperature. *Phys. Rev. B* 2020, 101, 1–6.

[28] S. A. Tawfik, A. Ali, M. Fronzi, M. Kianinia, T. T. Tran, C. Stampfl, I. Aharonovich, M. Toth, M J. Ford, First-Principles Investigation of Quantum Emission from hBN Defects. *Nanoscale* 2017, 36.

[29] H. Akbari, W.-H. Lin, B. Vest, P. K. Jha, and H. A. Atwater, Temperature-Dependent Spectral Emission of Hexagonal Boron Nitride Quantum Emitters on Conductive and Dielectric Substrates. *Phys. Rev. Applied* 2021, 15, 014036.

[30] Barnes, W. L.; Horsley, S. A. R.; Vos, W. L. Classical Antennae, Quantum Emitters, and Densities of Optical States. *J. Opt.* 2020, 22, 073501.

[31] Drexhage, K. H. In Progress in Optics, E. Wolf (Ed.) (Elsevier, New York, 1974), vol XII, pages 163-232.

[32] Jha, P. K.; Mrejen, M.; Kim, J.; Wu, C.; Wang, Y.; Rostovtsev, Y. V.; Zhang, X. Coherence-Driven Topological Transition in Quantum Metamaterials. *Phys. Phys. Lett.* 2016, 116, 165502.

[33] Ghosh, A.; Sharma, A.; Chizhik, A. I.; Isbaner, S.; Ruhlandt, D.; Tsukanov, R.; Gregor, I.; Karedla, N.; Enderlein, J. Graphene-Based Metal-Induced Energy Transfer for Sub-Nanometer Optical Localization. *Nat. Photonics* 2019, 13, 860–865.

[34] Qazilbash, M. M.; Brehm, M.; Chae, B. G.; Ho, P. C.; Andreev, G. O.; Kim, B. J.; Yun, S. J.; Balatsky, A. V.; Maple, M. B.; Keilmann, F.; Kim, H. T.; Basov, D. N. Mott Transition in VO_2 Revealed by Infrared Spectroscopy and Nano-imaging. *Science* 2017, 318, 1750–1753.

[35] Golla, D.; Chattrakun, K.; Watanabe, K.; Taniguchi, T.; LeRoy, B. J.; Sandhu, A. Optical Thickness Determination of Hexagonal Boron Nitride Flakes. *Appl. Phys. Lett.* 2013, 102, 161906.

[36] Nikolay, N.; Mendelson, N.; Özelci, E.; Sontheimer, B.; Böhm, F.; Kewes, G.; Toth, M.; Aharonovich, I.; Benson, O. Direct Measurement of Quantum Efficiency of single-Photon Emitters in Hexagonal Boron Nitride. *Optica* 2019, 6, 1084–1088.

[37] Kianinia, M.; Regan, B.; Tawfik, S. A.; Tran, T. T.; Ford, M. J.; Aharonovich, I.; Toth, M. Robust Solid-State Quantum System Operating at 800 K. *ACS Photonics* 2017, 4, 768–773.

[38] Wu, E.; Jacques, V.; Zeng, H.; Grangier, P.; Treussart, F.; Roch, J.-F. Narrow-Band Single-Photon Emission in the Near Infrared for Quantum Key Distribution. *Opt. Express* 2006, 14, 1296–1303.

[39] Davis, C. C. Laser and Electro-optics: Fundamental and Engineering (Cambridge University Press, 2014).

[40] Lethiec, C.; Laverdant, J.; Vallon, H.; Javaux, C.; Dubertret, B.; Frigerio, J.-M.; Schwob, C.; Coolen, L.; Maître, A. Measurement of Three-Dimensional Dipole Orientation of a Single Fluorescent Nanoemitter by Emission Polarization Analysis. *Phys. Rev. X* 2014, 4, 021037.

[41] Vogl, T.; Campbell, G.; Buchler, B. C.; Lu, Y.; Lam, P. K. Fabrication and Deterministic Transfer of High-Quality Quantum Emitters in Hexagonal Boron Nitride. *ACS Photonics* 2018, 5, 2305–2312.

[42] Pizzocchero, F.; Gammelgaard, L.; Jessen, B.; Caridad, J. M.; Wang, L.; Hone, J.; Bøggild, P.; Booth, T. J. The Hot Pick-Up Technique for Batch Assembly of van der Waals Heterostructures. *Nat. Commun.* 2016, 7, 11894.

[43] Purdie, D. G.; Pugno, N. M.; Taniguchi, T.; Watanabe, K.; Ferrari, A. C.; Lombardo, A. Cleaning Interfaces in Layered Materials Heterostructures. *Nat. Commun.* 2018, 9, 5387.

[44] Cueff, S.; Li, D.; Zhou, Y.; Wong, F. J.; Kurvits, J. A.; Ramanathan, S.; Zia, R. Dynamic Control of Light Emission Faster than the Lifetime Limit Using VO_2 Phase-Change. *Nat. Commun.* 2015, 6, 8636.

[45] Szilard, D.; Kort-Kamp, W. J. M.; Rosa, F. S. S.; Pinheiro, F. A.; Farina, C. Hysteresis in the Spontaneous Emission Induced by VO_2 Phase Change. *J. Opt. Soc. Am. B* 2019, 36, C46–C51.

[46] Stenzel, O.; Hahn, J.; Roder, M.; Ehrlich, A.; Prause, S.; Richter, F. The Optical Constants of Cubic and Hexagonal Boron Nitride Thin Films and their Relation to the Bulk Optical Constants. *Phys. Status Solidi A* 1996, 158, 281–287.

[47] Palik, E. D. Handbook of Optical Constants of Solids: Index (Academic Press, Waltham, MA, 1991).

[48] Boll, M. K.; Radko, I. P.; Huck, A.; Andersen, U. L. Photophysics of Quantum Emitters in Hexagonal Boron-Nitride Nano-flakes. *Opt. Exp.* 2020, 28, 7475.

Chapter 6

CONCLUSION AND OUTLOOK

6.1 Introduction

This thesis is composed of experimental demonstrations of active metasurfaces that control the fundamental properties of light, such as amplitude, phase, resonance frequency, thermal emission, and quantum emission. First, we demonstrated phase modulation using a plasmonic metasurface, which incorporates nanostructured VO_2 inside the MIM resonance cavity. The phase change in VO_2 induced large changes in near- and far-field characteristics of the metasurfaces. A continuous and a large phase shift was achieved through Joule heating with the near-infrared reflective metasurfaces. Second, we experimentally showed active thermal emission control based on a VO_2 metasurface. The metasurface comprised a thin-film absorber (VO_2) coupled with a waveguide grating structure, with a dielectric spacer located between them. The coupled structure exhibited tunable and narrowband thermal emission achieved by coupling the PCM-based absorber and a high-*Q* dielectric resonant structure. Finally, we investigated the nanoscale axial location of *h*BN quantum emitters in a multilayered flake. A PCM (VO_2) was introduced near the quantum emitters to modulate the spontaneous emission lifetime. The phase transition in VO_2 accompanied the LDOS, which modulated the emission rate of quantum emitters near the *h*BN/VO_2 interface. This chapter presents VO_2-based metasurfaces with reconfigurable beam-steering capability, which possess various potential applications, such as light detection and LiDAR systems.

6.2 Thermal Crosstalk Management

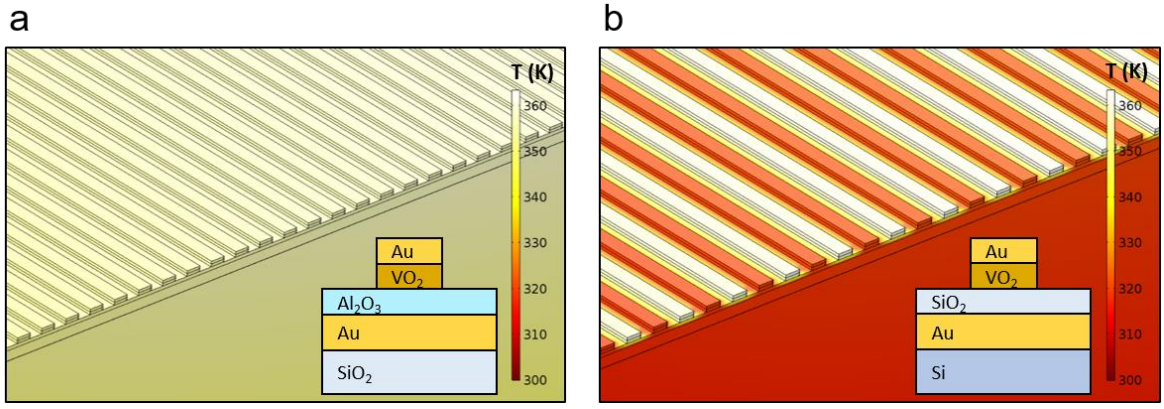

Figure 6.1. Heat-transfer simulation results of the beam-steering VO_2 metasurfaces. Electrical biases are periodically applied to each unit cell of the metasurfaces (a) without and (b) with thermal crosstalk management.

To individually manipulate each element of the metasurface through Joule heating, it is essential to mitigate the thermal crosstalk between the adjacent antennas. Figure 6.1 shows the temperature profile of the VO_2-based beam-steering metasurface. Electrical biases are periodically applied to each unit cell of the metasurface. The input power of the bias is chosen to achieve the maximal temperature of the ON-state unit cell to be slightly above 360 K, which indicates that VO_2 is completely transformed to the metallic state. Figure 6.1a shows significant thermal crosstalk across the entire metasurface structure when it is designed without thermal management. The thermal crosstalk can be significantly reduced through heat conduction engineering by introducing a thermally insulating dielectric layer underneath the VO_2 layer and a thermally conductive substrate. The corresponding heat distribution (Figure 6.1b) shows that the SiO_2 layer between each unit cell performs as a thermal insulator, whereas the Si substrate acts as a heat sink. This results in a temperature contrast ($\Delta T \approx 35$ K) between the ON- and OFF-state unit cells, which is sufficiently larger

than the typical hysteresis width (<20 K) of high-quality VO_2. Therefore, thermal management enables us to distinguish the different phases of VO_2 to achieve desirable optical responses from individual unit cells.

6.3 Dynamically Tunable Beam-Steering VO_2 Metasurfaces

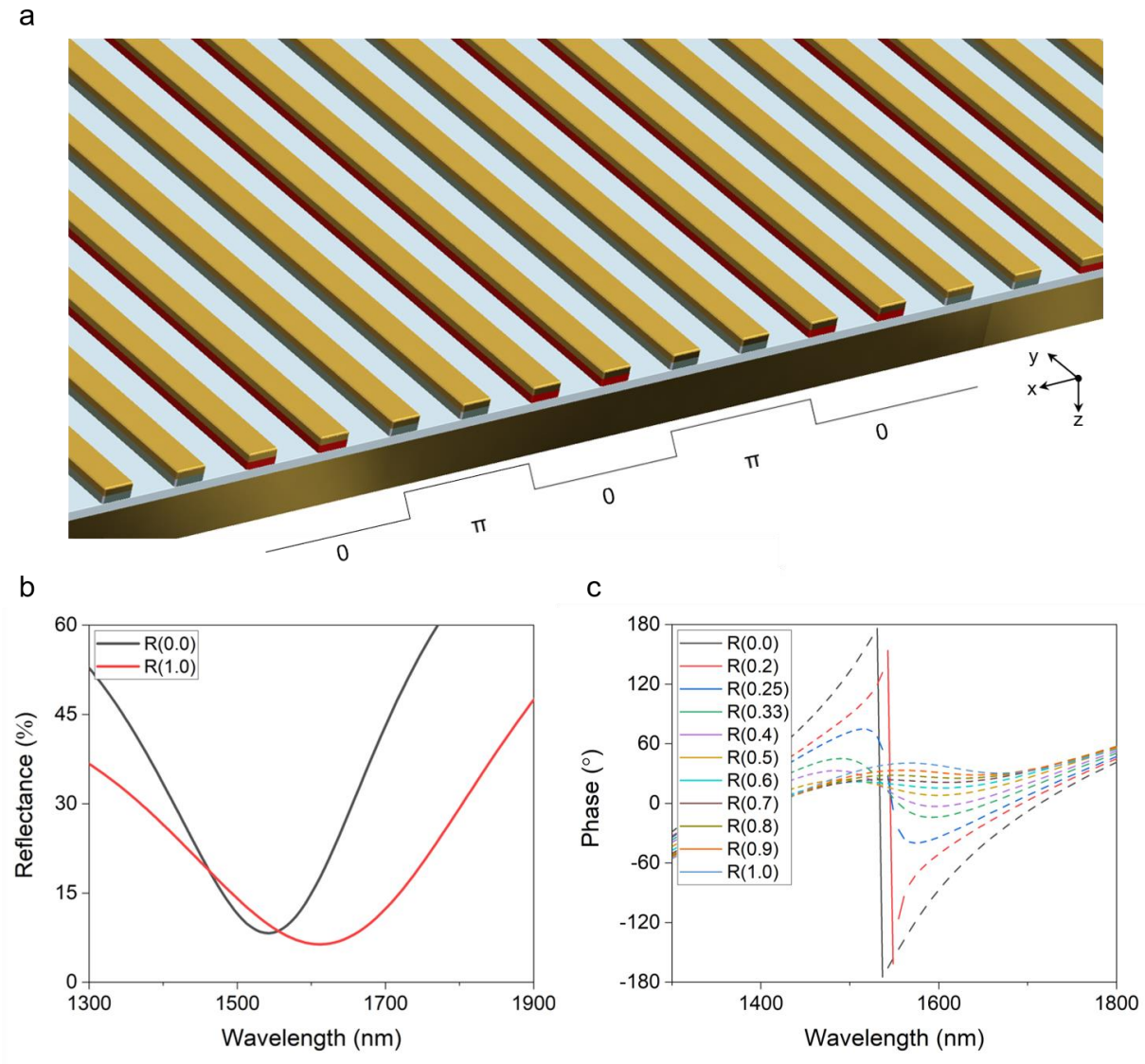

Figure 6.2. Beam-steering VO_2 metasurfaces working in the near-infrared region. (a) Schematic illustration of beam-steering VO_2 metasurfaces with two-level phase gratings. Simulation results of (b) reflectance spectra for different VO_2 phases and (c) phase modulation as a function of the rutile-phase volume fraction in the VO_2 layer.

Next, we designed a beam-steering VO_2 metasurface based on the thermal management results, operating in the near-infrared region (Figure 6.2a). According to the full-wave simulation results (Figure 6.2b), the metasurface exhibits a large reflection amplitude ($R \approx$ 9%) for both VO_2 phases. A continuous phase shift can be obtained by gradually changing the VO_2 phase, and the maximal phase shift near the insulating-phase resonance exceeds π (Figure 6.2c). The legend R(0.0) corresponds to the case in which VO_2 lies in a purely insulating phase, whereas R(1.0) corresponds to the case in which VO_2 lies in a purely metallic phase.

We investigated the far-field radiation patterns by changing the supercell period of the metasurfaces. We chose a working wavelength of $\lambda \approx 1.56$ μm to increase the beam-steering efficiency, where the reflectances of the insulating and metallic phases are equivalent. At this wavelength, the metasurface exhibits a reflectance R of approximately 9% and a phase shift $\Delta\varphi$ of approximately 180°. Figure 6.3a,b shows the beam-switching characteristics of the metasurface when assuming two-level phase gratings. The simulated diffraction angle is consistent with the theoretical value (solid red line) obtained from the grating equation. The results show significantly suppressed zeroth-order diffraction beam and a symmetric beam-steering profile because it is a two-level system. We observe the tunable angle of the first-order diffraction beam by changing the supercell period (or repeat number) [1]. The diffraction order at the negative angles is reduced when the multilevel blazed gratings are introduced (Figure 6.3c,d). The asymmetric phase profile results in the suppression of the negative-angle diffraction order beams. By adopting the phase gradient profile, the metasurface performs as a beam-steering metasurface rather than a beam-switching metasurface [2]. The performance of the metasurfaces with nonideal amplitude

and phase responses can be further improved by introducing an array-level inverse design based on an optimization algorithm [3].

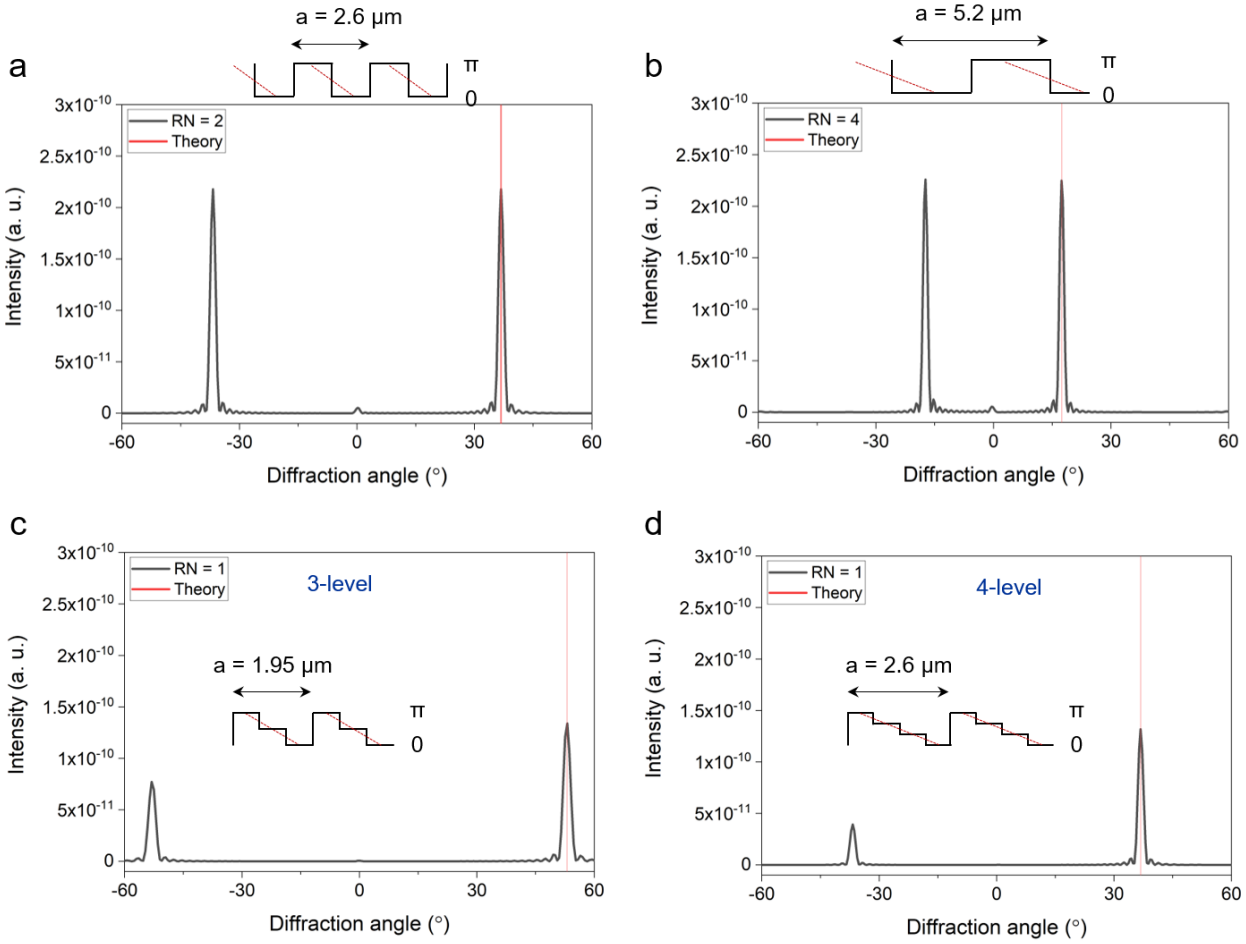

Figure 6.3. Simulation results and analytical calculations (solid red line) of VO_2-based beam-steering metasurfaces. (a, b) Beam-switching simulation results obtained by changing the repeat number of the two-level beam-switching metasurface. (c, d) Beam-steering simulation results of the beam-steering metasurface with three- and four-level blazed gratings.

6.4 References

[1] Wu, P. C.; Pala, R. A.; Kafaie Shirmanesh, G.; Cheng, W.; Sokhoyan, R.; Grajower, M.; Alam, M. Z.; Lee, D.; Atwater, H. A. Dynamic Beam Steering with All-Dielectric Electro-Optic III-V Multiple-Quantum-Well Metasurfaces. *Nat. Commun.* 2019, 10, 1–9.

[2] Shirmanesh, G. K.; Sokhoyan, R.; Wu, P. C.; Atwater, H. A. Electro-Optically Tunable Multifunctional Metasurfaces. *ACS Nano* 2020, 14, 6912–6920.

[3] Thureja, P.; Shirmanesh, G. K.; Fountaine, K. T.; Sokhoyan, R.; Grajower, M.; Atwater, H. A. Array-Level Inverse Design of Beam Steering Active Metasurfaces. *ACS Nano* 2020, 14, 15042–15055.